Durham University

Durham E-Theses

The radio halos of spiral galaxies

Brindle, Christopher

How to cite:

Brindle, Christopher (1978) *The radio halos of spiral galaxies*, Durham theses, Durham University. Available at Durham E-Theses Online: http://etheses.dur.ac.uk/8882/

Use policy

The full-text may be used and/or reproduced, and given to third parties in any format or medium, without prior permission or charge, for personal research or study, educational, or not-for-profit purposes provided that:

- a full bibliographic reference is made to the original source
- a link is made to the metadata record in Durham E-Theses
- the full-text is not changed in any way

The full-text must not be sold in any format or medium without the formal permission of the copyright holders.

Please consult the full Durham E-Theses policy for further details.

Academic Support Office, The Palatine Centre, Durham University, Stockton Road, Durham, DH1 3LE
e-mail: e-theses.admin@durham.ac.uk Tel: +44 0191 334 6107
http://etheses.dur.ac.uk

The Radio Halos of Spiral Galaxies.

A Thesis submitted to the University of Durham for the Degree of Master of Science.

by

Christopher Brindle, BSc.

May 1978.

The copyright of this thesis rests with the author. No quotation from it should be published without his prior written consent and information derived from it should be acknowledged.

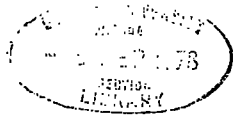

To my Mother

Abstract.

Models of the Galactic synchrotron radio-continuum emission are applied to the 'edge-on' galaxies NGC 891 and NGC 4631, to see if they can account for the distribution of emission observed in them. It is concluded that the model which has an emissivity which decreases linearly from the plane to a height of ~6 kpc, can reasonably well account for the distribution in NGC 891, whereas for NGC 4631, the model which has a 'thick disc' of emission which varies with Galactocentric distance, can fairly well account for the high Z-emission observed there.

Also in this thesis, the effect of spiral-arm irregularities on the synchrotron profile along the Galactic plane is investigated and the effect of spiral shocks on the irregular component of the magnetic field. It is shown that such irregularities can shift the peaks of maximum emission, in directions tangential to spiral-arms, through several degrees and also give rise to multiple peaks. The effect of the shock on the magnetic field is shown to decrease these peaks of emission.

Preface.

The work presented in this thesis was carried out during the period 1976 - 1978, whilst the author was a research student under the supervision of Dr. J. L. Osborne at the University of Durham.

The work in chapter 2 on the effect of arm irregularities on the synchrotron profile, and the effect of spiral shocks on the irregular component of the magnetic field, was carried out in collaboration with Dr. J. L. Osborne. All the calculations presented in chapter 5 are due solely to the author. The main conclusions from this work have been published in:-

Brindle, C., French, D. K. and Osborne, J. L., 1978, Mon. Not. R. astr. Soc. (in the press).

Contents

Chapter 1

Introduction - The Halo Problem.

1.1 Historical Background.

The galactic radio-continuum radiation was discovered by Karl G. Jansky in 1932, whilst carrying out a study in long-distance communications for the Bell laboratories in America. Working at a wavelength of 15 meters, he detected a steady background signal, which was greatest when his aerial pointed to the constellation Sagittarius. Grote Reber followed up Jansky's discovery, using a steerable, 30 ft. parabolic reflector. He produced the first radio maps of the sky, which showed peaks of emission in the Milky Way away from any optical sources, and in 1944 he attempted to detect M31, but failed because of inadequate sensitivity. With the rapid development of Radio Astronomy after the Second World War, radio surveys of the sky were made at low frequencies, in particular in Australia under J. L. Pawsey, and in England under M. Ryle.

Westerhout and Oort (1951) compared the radio distribution with that of various classes of galactic objects, and it seemed analogous to that of the most common stars, the G and K type dwarfs, which are distributed similarly to the mass in the Galaxy. They computed the brightness distribution to be expected if the sources of the radio emission were distributed in the same way as the mass. They found a good general agreement between the computed maps and a 100 Mhz survey by Bolton et al (1950), which was then the most complete survey. There was however one outstanding discrepancy; - the computed relative brightness towards the Galactic Poles and the anti-centre, were much less than the measured values.

Henyey and Keenan (1940), proposed that the radiation is

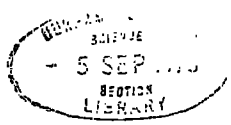

Bremsstrahlung emission in the ionized component of the interstellar gas. Alfvén and Herlofson (1950), proposed that the radiation from radio sources might originate from relativistic electrons, moving in the magnetic field of a star. About the same time Kiepenheur (1950), suggested that the electrons are the electron component of cosmic rays, and the radiation originates in their traversal through interstellar magnetic fields. Ginzburg in 1951, showed that the synchrotron process could explain the Galactic radio emission, if the flux of cosmic ray electrons is about one per cent that of the protons. This prediction was confirmed when the first balloon flights carrying cosmic ray electron detectors, were flown in the 1950's.

In 1950 Ryle, Smith and Elsmore suggested that some of the radio sources that they had detected in their survey, might be identified with nearby galaxies. The identification of a radio source with M31 was confirmed when Hanbury Brown and Hazard (1951), showed that the size of the radio source agreed with the optical size of the galaxy. They also showed that the total radio emission from Andromeda, is of the same order of magnitude as that from the Galaxy.

1.2 Evidence for a Galactic Radio Halo.

Shklovsky (1952) was the first person to suggest that the Galaxy is surrounded by a large, spherical radio halo or corona, as it is sometimes called. With a model of the radio-continuum emission, incorporating a spherical halo, the minimum brightness would occur at $l^{II} = 180^{o}$, $b^{II} = \pm 45^{o}$, and since the path length through the halo in this direction would be roughly three times less than that towards $l^{II} = 0^{o}$, $b^{II} = \pm 45^{o}$, the brightness would be about three times that in the latter. These two predictions were both confirmed by Baldwin in 1955.

During this period cosmic ray anisotropy measurements were made, which supported the halo hypothesis. It was found that the anisotropy of cosmic rays above 10^{12} ev is less than 10^{-4} ($\lesssim 10^{-3}$ from more recent measurements). Biermann and Davis (1958), pointed out that a large spherical volume containing cosmic rays, would lead to such a small anisotropy. This result was followed by the declaration of Pawsey (1961), that the "recognition of the corona in our Galaxy from observations of the nonthermal component of cosmic radio waves is one of the outstanding astronomical discoveries of the century." Since then much work has been done on the galactic distribution of continuum radio emission, and the propagation and confinement of cosmic rays, making such a "discovery" doubtful. Baldwin (1967) and Burke (1967), suggested that the enhanced emission from the local spiral arms and spurs, due to the compression of the magnetic field, might be able to explain the entire background radiation without the presence of a bright halo.

Webster (1975), from an analysis of T - T plots, in which the temperature of a region of the sky at a particular frequency, is plotted against the temperature of the same region at a different frequency, concluded that the 'signature' of the plots is adequately accounted for by a spherical halo with a radius of between 10 and 15 kpc. Assuming that the spectrum of the halo emission is steeper than that of the disc component, as would be expected from the energy loss processes, he produced synthetic T - T curves, which resemble the observed ones when a large halo is present. The T - T plots show a closed loop, and the separation of the two branches of the loop is the 'signature' of a radio halo with a spectrum steeper than that of the disc. According to him the radius of the halo is 12.5 kpc, and the emissivity at 81.5 Mhz 40^{o} k/kpc, about 30 times weaker than the disc emission. Although his work appears to be compelling evidence for a large halo, some workers are not in agreement

with his interpretation of the plots. His results also contradict the results of Bulanov et al (1975) and Dogel et al (1975), who showed, from cosmic ray diffusion calculations, that the average emissivity of the halo at frequencies around 15 Mhz must be about the same as that of the disc. Bulanov et al (1976), have shown that if the spectral index of the radiation changes slowly from disc to halo, as expected from diffusion models, Webster in assuming constant spectral indices, would have underestimated the ratio of halo to disc luminosity.

Strong (1977) did a 3-dimensional diffusion calculation to reproduce the T - T plots. He found that the average magnetic field intensity in the halo, may be about a fifth of that in the disc. The full width to half-maximum of radio-emission, is estimated to be about 6 kpc at 17.5 Mhz.

Recently French (1977), has modelled the radio-continuum radiation using a realistic model of the spiral-structure, and magnetic field and cosmic ray electron distributions in the Galaxy. From a detailed comparison with observations, it was concluded that the background emission can be best explained if the Galaxy possesses a 'pseudo-halo'. This halo is quite different from a spherical halo, in that the thickness of the halo decreases towards the Galactic centre, the thickness following that of the observed HI distribution.

1.3 Evidence Against a Radio Halo.

The observed relative amounts of spallation nuclei, Lithium, Beryllium and Boron, in the cosmic ray flux, has been used as evidence against a halo. From these measurements, it is found that the average amount of matter traversed by the primary cosmic rays is $\simeq 5\ g/cm^2$. Since the diffusion time for particles out of a chaotic halo is about 3×10^8 yr , the total mass in the halo would be about $3 \times 10^9\ M_\odot$, which is the same order of magnitude as that in which a halo would become

gravitationally unstable. Because it is not known how much matter the cosmic rays traverse before leaving their sources, it is not a very strong argument. Daniel and Stephens (1970), concluded that the cosmic ray confinement mechanisms require either no halo, or a 'leaky' halo.

Price (1974) could account for the high-latitude emission by placing the Sun on the inner edge of the adjacent outer arm on the Lin and Shu spiral pattern, which corresponds to the Perseus arm. French and Osborne (1976), however, pointed out that this is unacceptable since the Perseus arm is more than 1 kpc away.

Studies of nearby stars and 21-cm hydrogen observations indicate that the Sun lies close to or somewhere within a spur or branch of the overall spiral pattern, the Orion arm. Hornby (1966) argued that much of the high-latitude brightness is due to emission from the local arm, although this conclusion is not supported by the work of French.

The point is that both Hornby and Price regard the value of the local synchrotron emissivity as being arbitrarily adjustable, while French takes it to be fixed by the observed values of field strength and electron intensity at the Earth. The spiral arms will have a Z-distribution of emissivity that is more strongly peaked towards the galactic plane, than has the interarm region. French then argues that the placing of the Sun in an arm region lowers, rather than increases, the pole temperature.

1.4 Difficulties in Detecting a Galactic Radio Halo.

The detection of a possible radio halo is made uncertain by the difficulty in subtracting the background signal, due to extra-galactic sources, and that due to local sources, such as extended supernova remnants. It is also complicated by possible spurious instrumental effects, due to sidelobe responses far from the main beam.

Baldwin's early work of 1955 could have been influenced by such

sidelobe responses. Burke (1967) repeated Baldwins' measurements and found the ratio of the brightness temperatures in the two directions to be one, a value in agreement with the absence of a halo.

The extra-galactic component can be subtracted if a reasonable value for the mean spectral index can be established. From the assumption that the flux density of all extra-galactic radio sources at meter wavelengths has the same spectral shape, $S \propto \nu^{-0.75}$, Bridle (1967) found that the integrated extra-galactic emission at 150 Mhz is 48 ± 11° K.

Subtracting the emission due to all the spurs and fine structure is a very difficult task. Early rough attempts to do so (Baldwin, 1963, Yates, 1968), confirmed that an extensive halo is no longer demanded by the observations.

1.5 Radio Halos of External Galaxies.

Because of the difficulties, mentioned above, in detecting unmistakably a radio halo surrounding the Galaxy, external galaxies have been studied to see if halos exist. 'Edge-on' galaxies are the ideal ones for this purpose. A radio-telescope of sufficient sensitivity and resolution would be able to detect the emission from a halo of such a galaxy, if it existed, unambiguously.

M31 is the nearest galaxy that is believed to be similar to ours, and has been studied in detail at optical and radio-wavelengths, (see Berkhuijsen, 1977 for comparison of radio and optical data). Interferometer measurements at 81 Mhz, made by Baldwin (1954) at Cambridge, showed that the emission distribution could consist of a component "distributed like the stars" plus a spherical component. This was the first evidence of a halo in an external galaxy, and it confirmed that in general terms the distribution of radio continuum emission in M31 is roughly the same as that of the Galaxy (Westerhout and Oort 1951). Baldwin estimated that the

spherical component contributes about two-thirds of the total intensity.

In a follow-up investigation to their first detection of radio emission from M31, Hanbury-Brown and Hazard (1959), proposed an interpretation of the observed radio emission in terms of a disc and a halo model. This interpretation was supported by observations of Large et al. (1959) at 408 Mhz.

Many surveys of M31 have been done since then, none of them conclusively proving the existence of a halo, but the usual conclusion being that one exists. Pooley (1969a) found that the total flux density in the spiral arms, nucleus, and background sources is significantly less at 408 Mhz than the total flux density measured by Large et al. (1959), at 408 Mhz, thus supporting the halo hypothesis. Durdin and Terzian (1972) reached a similar conclusion at 73.8 Mhz. Assuming the 5C3 sources all have a spectral index of -0.7, their halo dimensions are 25 x 40 kpc.

A more recent 408 Mhz survey, made by Haslam et al. (1974) with the 100-meter Bonn radio-telescope, was used by Wielebinski (1976) for a thorough investigation into the origin of the radio emission. After having subtracted the emission due to sources in the area, and that from the spiral arms of our own galaxy, he concluded that if a halo exists around M31, it must be at least a factor of three fainter than the halo proposed for our Galaxy by Webster (1975).

van der Kruit and Allen (1976), after having evaluated all of the results of the various surveys, concluded that a faint radio halo probably does exist around M31, though its brightness is not yet resolved.

Pooley (1969b) using the aperture synthesis radio-telescope at Cambridge, made the first high-resolution radio-continuum observations of NGC 4631. He established an upper limit to the brightness temperature of a halo of 10°K at 408 Mhz. More recent measurements with the Westerbork telescope, which has a higher sensitivity than the Cambridge one, by Ekers

and Sancisi (1977), have revealed radio emission extending to about 12 kpc from the plane. At 610 Mhz the halo constitutes only a few percent of the total flux density.

Observations by Allen, Baldwin and Sancisi (1977), of NGC 891 at Westerbork, have also revealed emission at large distances from the plane for this galaxy.

Other 'edge-on' galaxies have been studied, as well as the above two, although not in as much detail. NGC 3432 (Sc), NGC 3675 (Sb), and NGC 3556 (Sc) were observed in the Westerbork study of bright spiral galaxies, at 1415 Mhz (van der Kruit, 1973). In the case of the former two galaxies, there is some evidence for a possible extended emission.

In a similar southern sky survey the nearby 'edge-on' galaxies NGC 253 (SAB (s) c) and NGC 4945 (SB (s)), have been studied by Cameron (1971), with the Molonglo Cross radio-telescope at 408 Mhz. No evidence was found, for both galaxies, for a halo component of total emission (0.5 to 1.0) x 10^{21} W Hz^{-1} $ster^{-1}$ at 408 Mhz, this being the value then postulated for the Galactic halo.

1.6 Cosmic ray nucleon and material halos.

Since the electron component of cosmic rays, which produce the synchrotron radio emission, is only a small percentage of the total cosmic ray flux, it is possible that a nucleon halo as well as a radio halo exists. Cosmic ray nucleons do not suffer significant energy losses in a large halo, so that evidence against an extensive cosmic ray halo argues against an extensive radio halo. The distribution of galactic 100 Mev γ-rays, as measured by the Sas-2 and Cos-B satellites, provides constraints on the possibility of a nucleon halo and a test for the existence of a radio halo. The Sas-2 observations of $\sim$ 100 Mev γ-radiation in the Galaxy imply a non-uniform cosmic ray distribution.

Stecker (1977) used this data to show that the observations are best explained by the absence of a nucleon halo, or a very thin one. Worral (1977) showed that a large percentage of the high latitude γ-ray flux probably emanates from the Galaxy and discrete extragalactic sources. She considers it likely that the deficit in the γ-ray flux (the observed flux is greater than the flux expected from the disc) is due to the inverse- compton flux from a flat halo. The γ-ray data therefore allows for the possibility of a nucleon and a radio halo.

The only form of halo known definitely to exist around the Galaxy is a halo of population II stars, consisting of subdwarfs, globular clusters and RR Lyr-variables with $P > 0^d.4$ (Unsöld 1969). Firm evidence that external spiral galaxies are surrounded by massive faint halos of stars has been obtained by Hegyi and Gorber (1977), from observations of the 'edge-on' galaxy NGC 4565. They found that significant emission of light occurs as far as 30 kpc above the plane of the galaxy, which is best explained by the presence of stars.

1.7 Summary of Thesis.

The object of this thesis is to draw some conclusions from the observations of the radio-continuum emission of 'edge-on galaxies', regarding a possible halo emission around the Galaxy, from models of the z - distribution in emissivity of the Galaxy.

Chapter 2 describes the models of the radio-continuum emission from the Galaxy that will be used. In chapter 3 the 'edge-on' galaxies NGC 4631 and NGC 891 will be compared with the Galaxy, since they have both been studied in detail. Chapter 4 describes the models of the radio-continuum emission, that have been constructed for these two galaxies, from the chapter 3 models. The final chapter, chapter 5, presents the results of the calculations of chapter 4, and compares them with the observations. Also in this chapter, the conclusions will be presented and a discussion of possible serious omissions to the chapter 4 models.

Chapter 1 - References

Alfvén, H. and Herlofson, N. 1950, Phys. Rev. 78, 616.

Allen, R. J., Baldwin, J. E., and Sancisi, R. 1977, Astron. and Astrophys. (in the press)

Baldwin, J. E. 1954, Nature 174, 320.

Baldwin, J. E. 1955, Mon. Not. R. Astr. Soc. 115, 690.

Baldwin, J. E. 1963, Observatory 83, 153.

Baldwin, J. E. 1967, I. A. U. Symp. 31, Radio Astronomy and the Galactic System, ed. H. van Woerden, P. 337.

Berkhuijsen, E. M. 1977, Astron. and Astrophys. 57, 9.

Biermann, L. and Davis, L. 1958, z. Astrophys. 51, 19.

Bolton, J. G., Stanley, G. J., Slee, O. B. and Westfold, K. C. 1950, Aust. J. Sci. Res. A. 3, 19.

Bridle, A. H. 1967, Mon. Not. R. Astr. Soc. 136, 219.

Bulanov, S. V., Syrovatskii, S. I. and Dogiel, V. A. 1976, Astrophys. and Space Sci. 44, 255.

Bulanov, S. V., Syrovatskii, S. I. and Dogiel, V. A. 1975.

Burke, B. F. 1967. I. A. U. Symposium No. 31, p. 361.

Cameron, M. J. 1971, Mon. Not. R. Astr. Soc. 152, 439.

Daniel, R. R., and Stephens, S. A. 1970, Space Sci. Rev. 10, 559.

Dogiel, V. A., Bulanov, S. V. and Syrovatskii, S. I. 1975, Proc. 14th Int. Cosmic Ray Conf. Munich v. 2 p. 700.

Durdin, J. M., Terzian, Y. 1972, Astron. J. 77, 637.

Ekers, R. D. and Sancisi, R. 1977, Astron. and Astrophys. 54, 973.

French, D. K. 1977, Phd thesis University of Durham.

French D. K., and Osborne, J. L. 1976, Mon. Not. R. Astr. Soc. 177, 509.

Haslam, C. G. T., Wilson, W. E., Graham, D. A., and Hunt, G. C. 1974, Astron. and Astrophys. Suppl. 13, 359.

Hanbury Brown, R. and Hazard, C. 1951, Mon. Not. R. Astr. Soc. 111, 357.

Hanbury Brown, R. and Hazard, C. 1959, Mon. Not. R. Astr. Soc. 119, 298.

Hegyi, D. and Gorber, G. 1977, Astrophys. J. 218, p. L7

Henyey, L. G. and Keenan, P. C. 1940, Astrophys. J. 91, 625.

Hornby, J. M. 1966, Mon. Not. R. Astr. Soc. 133, 213.

Jansky, K. G. 1932, Proc. Inst. Rad. Eng. 20, 1920.

Jansky, K. G. 1933, Nature 132, 66.

Jones, F. C. and Stecker, F. W. 1977. preprint x - 602 - 77 - 73, Goddard Space Flight Centre, Greenbelt, Maryland.

Kiepenheur, K. O. 1950, Phys. Rev. 79, 738.

Kruit, P. C. van der. 1973, Astron. and Astrophys. 29, 249.

Kruit, P. C. van der., and Allen, R. J. 1976, in Annual Review of Astronomy and Astrophysics. vol. 14, 417-445.

Large, M. I., Mathewson, D. S. and Haslam, C. G. T. 1959, Nature 183, 1250.

Lodge, O. J. 1900, "Signalling across Space without Wires," "The Electrician" Printing and Publishing Company, Limited, London.

Oort, J. H. and Westerhout, G. 1951, Bull. Astr. Inst. Netherlands. 11, 323.

Pawsey, J. L. 1961, in Galactic Structure, A. Blaauw and M. Schmidt, eds. Chicage, University of Chicago Press, p. 219.

Pooley, G. G. 1969a, Mon. Not. R. Astr. Soc. 144, 101.

Pooley, G. G. 1969b, Mon. Not. R. Astr. Soc. 144, 143.

Price, R. M., 1974, Astron. and Astrophys., 33, 33.

Ryle, M., Smith, F. G., Elsmore, B. 1950, Mon. Not. R. Astr. Soc., 110, 508.

Reber, G. 1940, Astrophys. J., 91, 621.

Reber, G. 1944, Astrophys. J., 100, 279.

Shklovsky, I. S. 1952, Astron. Zh. 29, 418.

Strong, A. W., 1977, Submitted Astronomy and Astrophysics.

Unsöld, A. 1969 The New Cosmos. (translated by W. H. McCrea) Heidelberg Science Library, vol. 5/6 p. 342.

Webster, A. S. 1975, Mon. Not. R. Astr. Soc. 171, 243.

Wielebinski, R. 1976, Astron. and Astrophys., 48, 155.

Worral, D. H. 1977, Ph.d thesis University of Durham.

Yates, K. W. 1968, Australian J. Phys., 21, 167.

Chapter 2

A Model of the Synchrotron Radiation of the Galaxy.

2.1 Introduction.

In the paper of Brindle et al. (1978), which is based on the calculations presented by French (PhD. Thesis, Durham 1977), the Galactic continuum radiation has been modelled to try to explain the distribution of emissivity over the whole celestial sphere. This chapter will summarize the model, since the ingredients will be used in a later chapter to produce a model of an 'edge-on' spiral galaxy. Also in this chapter the effect of spiral shocks on the magnetic field will be discussed, together with the effect of irregularities in spiral arms on the synchrotron profiles.

2.2 Summary of Model.

2.2.1 Magnetic field.

The field consists of a regular component that runs parallel to the arms, and a superimposed isotropically orientated random component. In regions where there is no field compression the ratio of magnitude of regular to irregular is adjusted to give the best fit to the observations, and is taken to be 0.75. The overall magnitude of the field intensity has the form

$$H(R) \propto \left[1 - \exp\left(-\frac{R^2}{4}\right)\right]\left[\exp - \frac{R^2}{R_o^2}\right] \qquad (2.1)$$

The first bracket ensures the magnetic field falls to zero at the centre, as expected from dynamo theory of field generation (White 1977). The second bracket determines the radial fall off, R_o being taken to be 13.1, again in order to reproduce the observations.

2.2.2 Arm - interarm Modulation.

Density wave theory was used in D. K. French's model to determine the compression of Magnetic field, with distance from the inner edge of spiral arms and height above the plane. According to the theory the gas density rises abruptly at an arm, and then falls off approximately exponentially out to the next arm, where it rises abruptly again. The radial variation was approximated by the expression,

$$\frac{\rho_2}{\rho_1} = 4.1 \exp\left(-13.7\, a/A\right) + 0.7 \qquad (2.2)$$

Where A is the radial separation of the two arms adjacent to the point being considered, a the distance to the inner arm, and ρ_1, ρ_2 the uncompressed and compressed gas densities respectively. At approximately 0.5 kpc above the plane the compression is expected to have fallen to zero, since at this height the magnetic pressure overcomes the gas compression. The polynomial which approximates the fall off in compression with height above the plane is

$$D(z) = 1 + 0.7715z - 17z^2 + 22.914z^3 \qquad (2.3)$$

The overall compression at a particular distance between the arms and height above the plane, is obtained when the exponential term in 2.2 is multiplied by 2.3.

2.2.3 Spiral Structure.

The galactic spiral structure used in the model is based upon the model of Georgelin (1976), which used HII regions as spiral tracers and the map of neutral hydrogen outside the Solar Circle of Verschuur (1973). The overall structure is that of a four-armed spiral galaxy, with the Sun situated between the Sagittarius and Perseus arms. Fig. 2.1 shows the spiral structure.

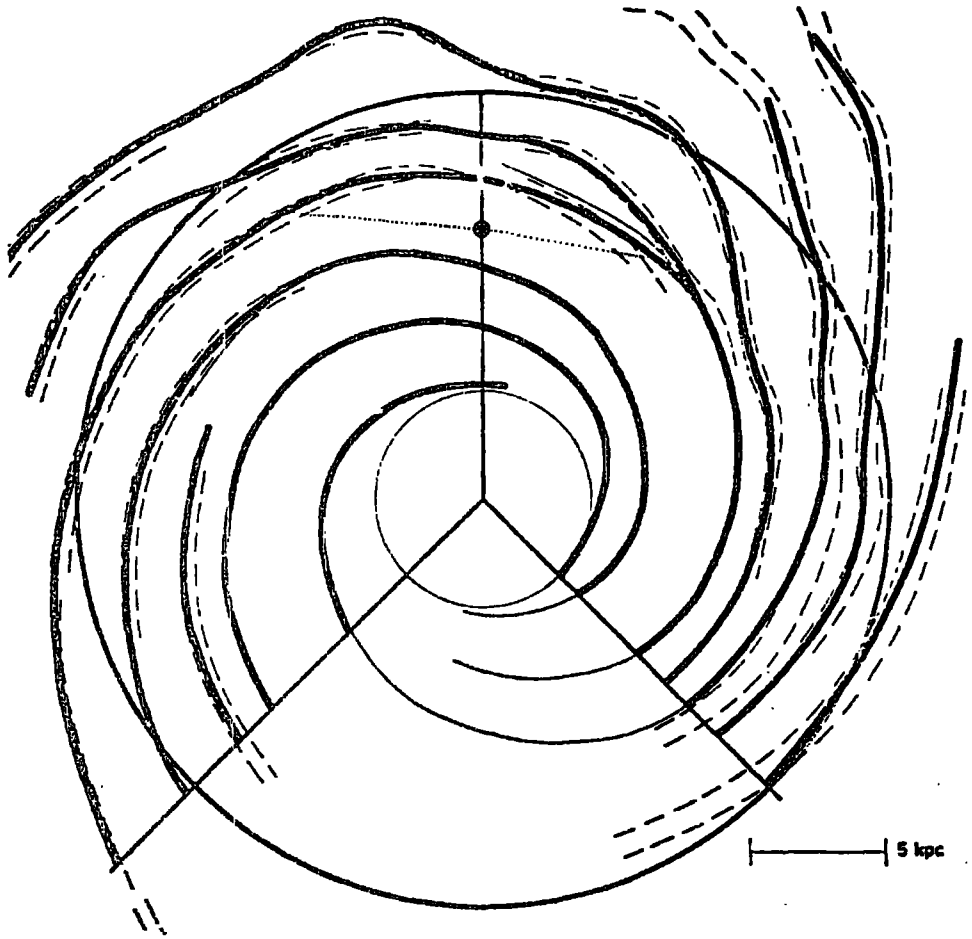

Fig. 2.1 Galactic Spiral Structure.

spiral structure of Georgelin (1976), using HII regions.

spiral structure of Verschuur (1973), using HI regions.

Dotted line represents the Orion feature, and ⊕ the location of the Sun at R = 10 kpc. Circle with radius 15 kpc represents boundary beyond which emission is taken to be zero.

2.2.4 Brightness Temperature Determination.

The brightness temperature in a given direction is calculated from the formula,

$$T_b = 0.0498 I_o \int_0^S \left\{ \left[H(A) \sin\theta \frac{S_2}{S_1} \right]^{1.8} + H_{eff}^{1.8} \left(\frac{S_2}{S_1}, \theta, F \right) \right\} dS \qquad (2.4)$$

I_o is the observed value of electron intensity at the Earth at 1 GeV, 80^{+70}_{-30} m^{-2} s^{-1} sr^{-1} GeV^{-1},

and this is assumed uniform throughout the Galaxy. H_{eff} is the effective value of the irregular component of the magnetic field. The integrations were performed out to a boundary of 15 kpc, using a step length of 0.015 kpc. θ is the angle between the line of sight and the regular component of the magnetic field.

2.3 Magnetic Field Compression.

Due to the high conductivity of the gas near the plane of the Galaxy, the magnetic field is effectively tied to it. The spiral shock fronts of Density Wave Theory result in compression perpendicular to the spiral arms and the regular field. Therefore the regular component of the magnetic field inside the shock simply increases as the shock strength. Things are not so simple for the irregular component, which is considered to be isotropic. To obtain the effective magnetic field to put into the brightness temperature formula, the quantity $(H \sin\theta)^{\frac{\delta+1}{2}}$ has to be averaged over all values of θ. The field lines that are orientated perpendicular to the shock are unaffected, but the ones that are inclined to the shock undergo a certain amount of 'bending'. Fig. 2.2 clarifies this situation.

After the shock the component H_y is enhanced by the factor $\frac{S_2}{S_1}$. The net effect is an increase in H, and a decreasing of the angle χ,

as shown in Fig. 2.2 (b).

In the three-dimensional case the component of the magnetic field perpendicular to the galactic plane is also enhanced by the factor $\frac{S_2}{S_1}$. The co-ordinate system that will be used to derive H_{45} is shown in Fig. 2.3.

The X - Y plane corresponds to the galactic plane, and the components of a randomly orientated magnetic field vector $\underline{H}$, with no compression, are

$$\underline{H} = \underline{H}_x + \underline{H}_y + \underline{H}_z \qquad (2.5)$$

In the compressed field case the components become,

$$\underline{H}' = \underline{H}_x + \frac{S_2}{S_1}\underline{H}_y + \frac{S_2}{S_1}\underline{H}_z$$

$$= \underline{H}_x + \underline{H}_y' + \underline{H}_z' \qquad (2.6)$$

Fig. 2.4 shows the decomposition of the randomly orientated magnetic field vector $\underline{H}$, and Fig. 2.5 the component of $\underline{H}$ in the Y - Z plane,

$$\underline{H}_{yz} = |\underline{H}_{yz}| = \left(|\underline{H}_z|^2 + |\underline{H}_y|^2\right)^{\frac{1}{2}} = H\sin(\alpha) \qquad (2.7)$$

Regarding $|\underline{H}|$ as H_x etc., from the diagrams

$$\cos\alpha = \frac{H_x}{H}, \quad \tan\phi = \frac{H_z}{H_y} \qquad (2.8)$$

where α is the angle between $\underline{H}$ and the x - axis, as shown in Fig. 2.4. ϕ is the angle between the y - axis and the projection of $\underline{H}$ onto the Y - Z plane, as shown in Fig. 2.5.

From these two relations and the diagrams,

$$H_x = H\cos\alpha, \quad H_y = H\sin\alpha\cos\phi, \quad H_z = H\sin\alpha\sin\phi \qquad (2.9)$$

$$H_y' = \frac{S_2}{S_1} H\sin\alpha\cos\phi, \qquad (2.10)$$

$$H_z' = \frac{S_2}{S_1} H\sin\alpha\sin\phi \qquad (2.11)$$

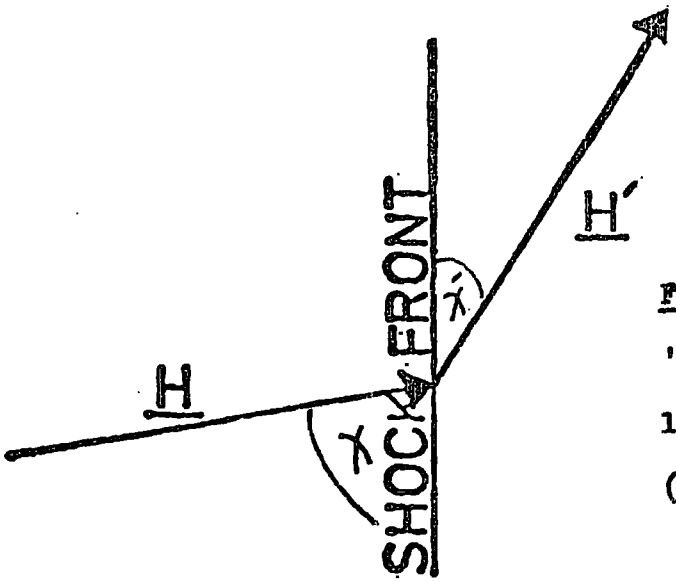

Fig. 2.2a

'Bending' of a magnetic field line due to a shock front. (2 - D case)

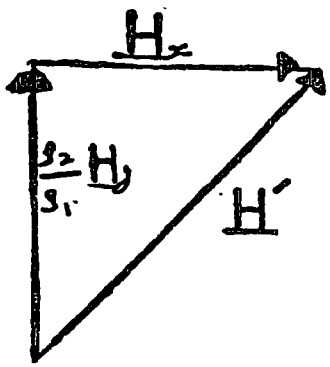

Fig. 2.2b

Decomposition of the modified field line into x and y components.

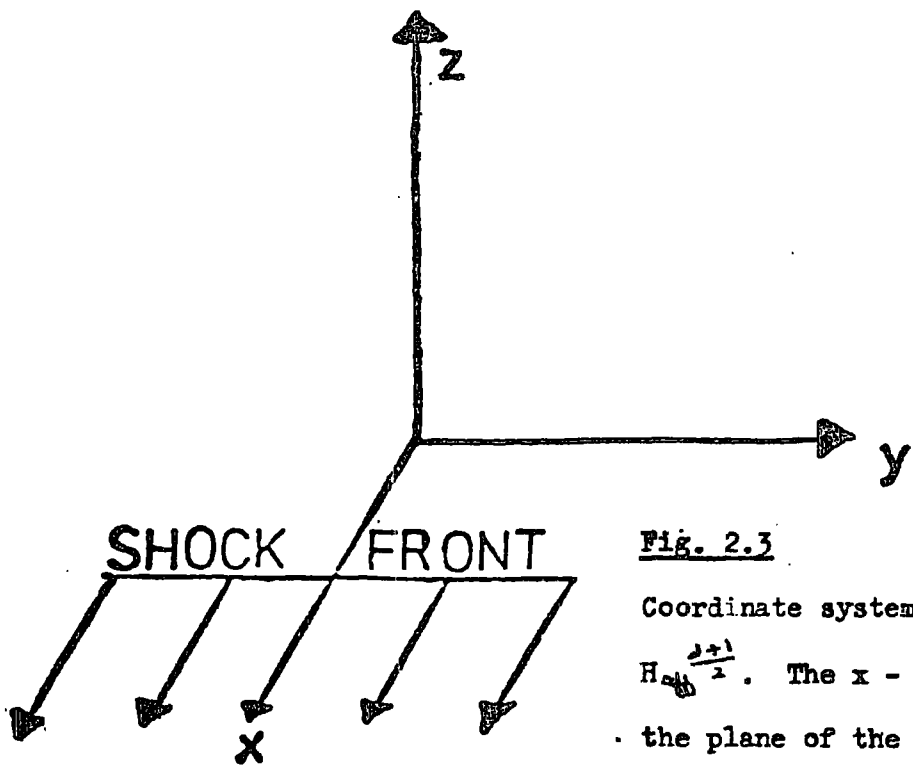

Fig. 2.3

Coordinate system used to derive $H_{\perp}^{\frac{s+1}{2}}$. The x - y plane represents the plane of the Galaxy.

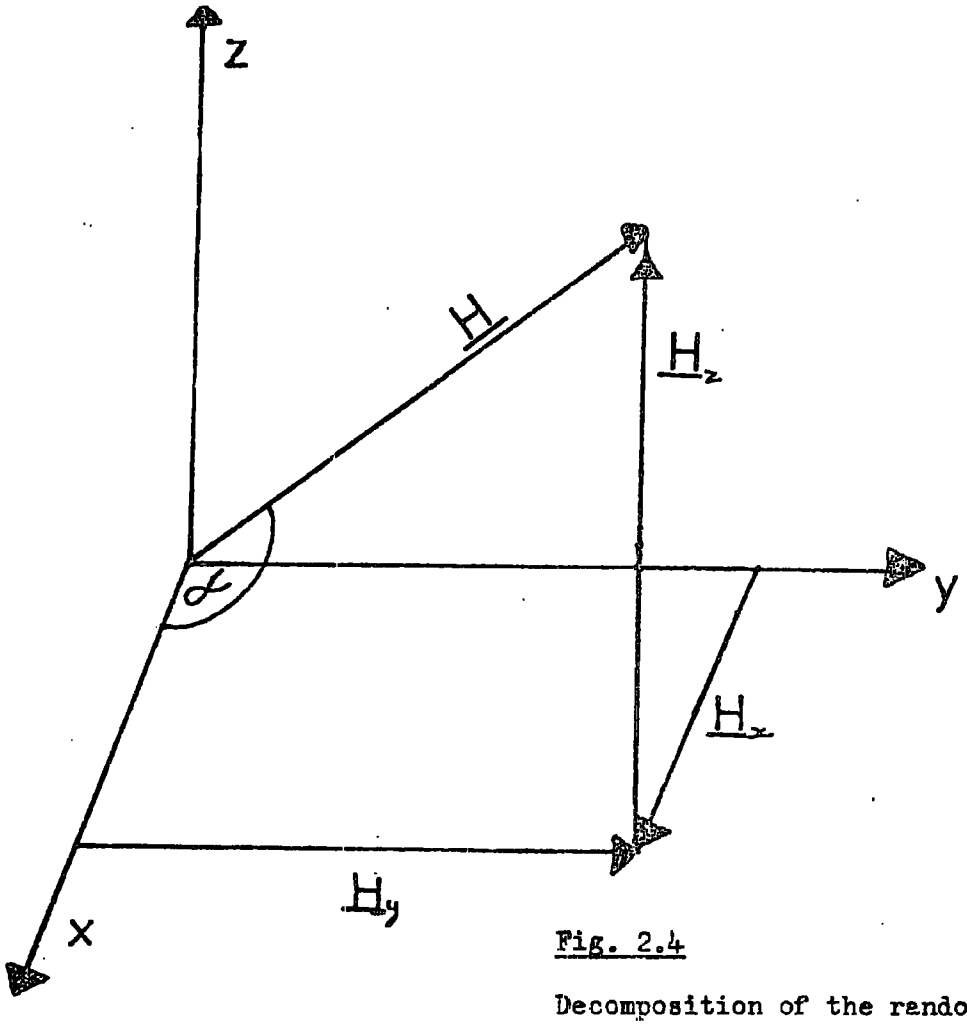

Fig. 2.4

Decomposition of the randomly orientated magnetic field vector H, into its x, y and Z components.

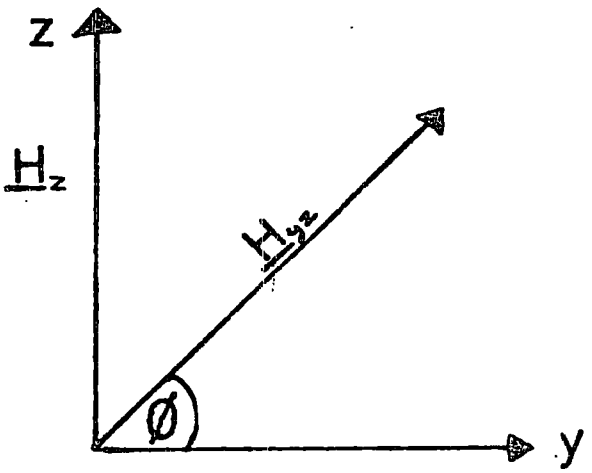

Fig. 2.5

Component of H projected onto Y - Z plane.

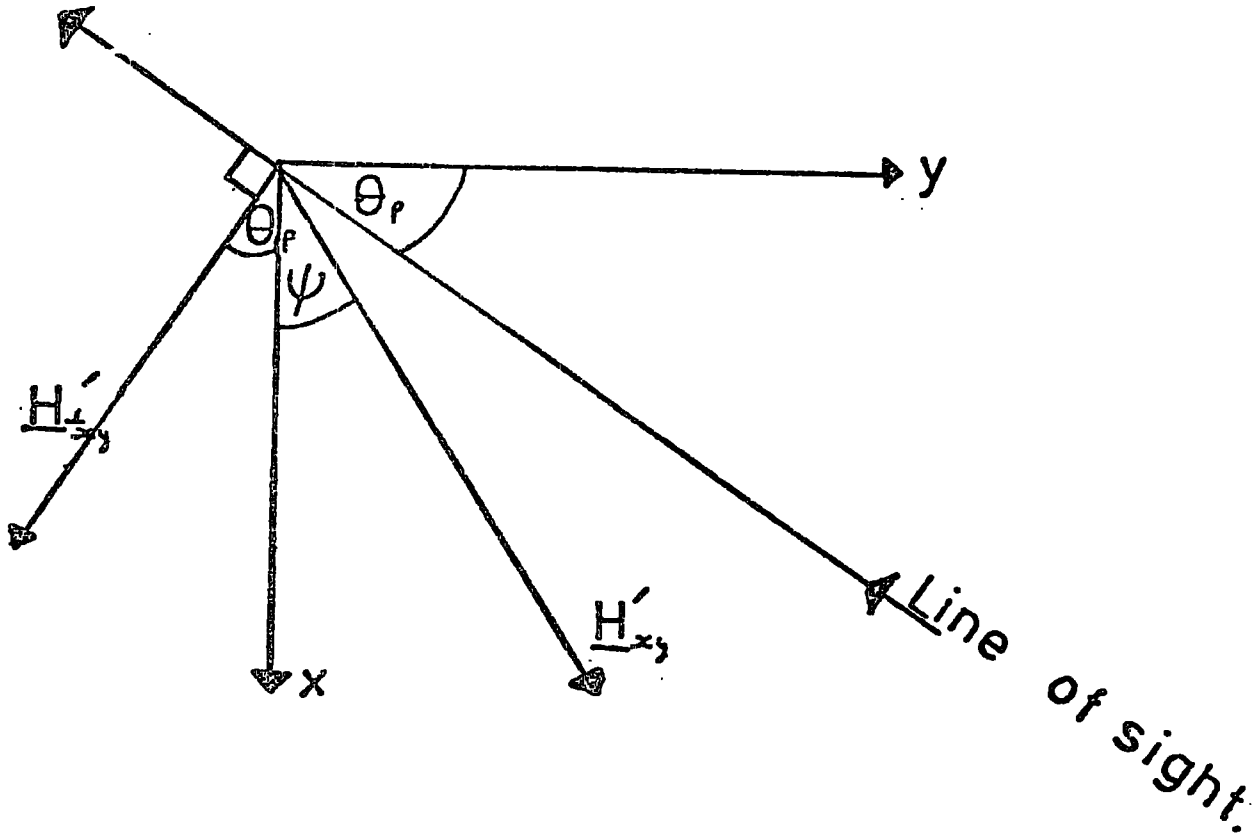

Fig. 2.6

The geometry in the plane of the Galaxy.

Since the nearest spiral arm, the Perseus arm, is over 2 kpc away, and the compression region of the disc is 0.5 kpc, the angle between the line of sight and the galactic plane will always be very small, and here it will be assumed to be zero.

Fig. 2.6 shows the geometry in the plane of the Galaxy. $\underline{H}'_{\perp xy}$ is the perpendicular component of $\underline{H}'_{\perp xy}$ to the line of sight in the plane of the Galaxy, Θ_p the angle between the line of sight and the Y - axis, and ψ the angle between $\underline{H}'_{xy}$ and the X - axis.

From Fig. 2.6 the magnitude of $\underline{H}'_{xy}$ is given by

$$H'_{xy} = \left(H_x^2 + H_y'^2\right)^{\frac{1}{2}} \qquad (2.12)$$

But since $\psi = \tan^{-1}\left(\frac{H_y'}{H_x'}\right)$, the perpendicular component of the compressed magnetic field vector to the line of sight, in the x - y plane, is given by,

$$H'_{\perp xy} = \left(H_x^2 + H_y'^2\right)^{\frac{1}{2}} \cos\left(\Theta_p + \tan^{-1}\left(\frac{H_y'}{H_x'}\right)\right)$$

Considering also the H_z' component of $\underline{H}'$ then,

$$H'_{\perp} = \left[H_z' + \left(H_x^2 + H_y'^2\right)\cos^2\left(\Theta_p + \tan^{-1}\left(\frac{H_y'}{H_x'}\right)\right)\right]^{\frac{1}{4}} \qquad (2.13)$$

Expressing this equation in terms of H, α and ϕ, by using equations 2.10 and 2.11, it becomes

$$H'_{\perp} = H\left[\left(\frac{s_2}{s_1}\sin\alpha\sin\phi\right)^2 + \left(\cos^2\alpha + \left(\frac{s_2}{s_1}\sin\alpha\cos\phi\right)^2\right)\cos^2\left(\tan^{-1}\left(\frac{s_2}{s_1}\tan\alpha\cos\phi\right) + \Theta_p\right)\right]^{\frac{1}{2}} \qquad (2.14)$$

In order to calculate the synchrotron emission from this random component, the quantity $H_{eff}^{\frac{\delta+1}{2}}$ has to be evaluated. This quantity is obtained by integrating equation 2.14 over all possible values of α and ϕ, such that

$$H_{eff}^{\frac{\delta+1}{2}} = \frac{H^{\frac{\delta+1}{2}}}{4\pi}\int_{\alpha=0}^{\pi}\int_{\phi=0}^{2\pi}\left[\left(\frac{S_2}{S_1}\sin\alpha\sin\phi\right)^2+\left(\cos^2\alpha+\left(\frac{S_2}{S_1}\sin\alpha\cos\phi\right)^2\right)\cos^2\left(\tan^{-1}\left(\frac{S_2}{S_1}\tan\alpha\cos\phi\right)+\theta_p\right)\right]^{\frac{\delta+1}{4}}\sin\alpha\,d\alpha\,d\phi, \tag{2.15}$$

which comes from the general expression

$$H_{eff}^{\frac{\delta+1}{2}} = \frac{\int_0^{\pi}(H\sin\theta)^{\frac{\delta+1}{2}}2\pi\sin\theta\,d\theta}{\int_0^{\pi}2\pi\sin\theta\,d\theta}$$

$$= \frac{H^{1.8}}{4\pi}\times 8.623, \text{ for } \delta = 2.6.$$

In this expression θ_p can be regarded as the angle between the line of sight and the magnetic field direction. Since this expression needs to be known for nearly all locations in the Galaxy, it was evaluated numerically for values of θ_p between 0 and 90° for compression ratio's $\frac{S_2}{S_1}$ between 1 and 5. The following expression was then fitted to the results,

$$\left(\frac{H_{eff}}{\frac{H(R)}{F}}\right)^{\frac{\delta+1}{2}} = 0.6861\left(\frac{S_2}{S_1}\right)^{1.8}\left[1-0.477\left(1-\left(\frac{S_2}{S_1}\right)^{-2}\right)\cos^2(\theta_p)\right] \tag{2.16}$$

where 2.15 has been normalized by dividing by $\frac{1}{8.623}\left(\frac{S_2}{S_1}\right)^{1.8}$

This equation agrees with numerical solutions to 2.15 to within 1 or 2% for $\theta_p = 45^\circ$ with $\frac{S_2}{S_1} = 4$, and to within comparable accuracy for other values of θ_p and $\frac{S_2}{S_1}$. Fig. 2.7a and 2.7b show the variation of $H_{eff}^{\frac{\delta+1}{2}}$ with $\frac{S_2}{S_1}$ and θ_p.

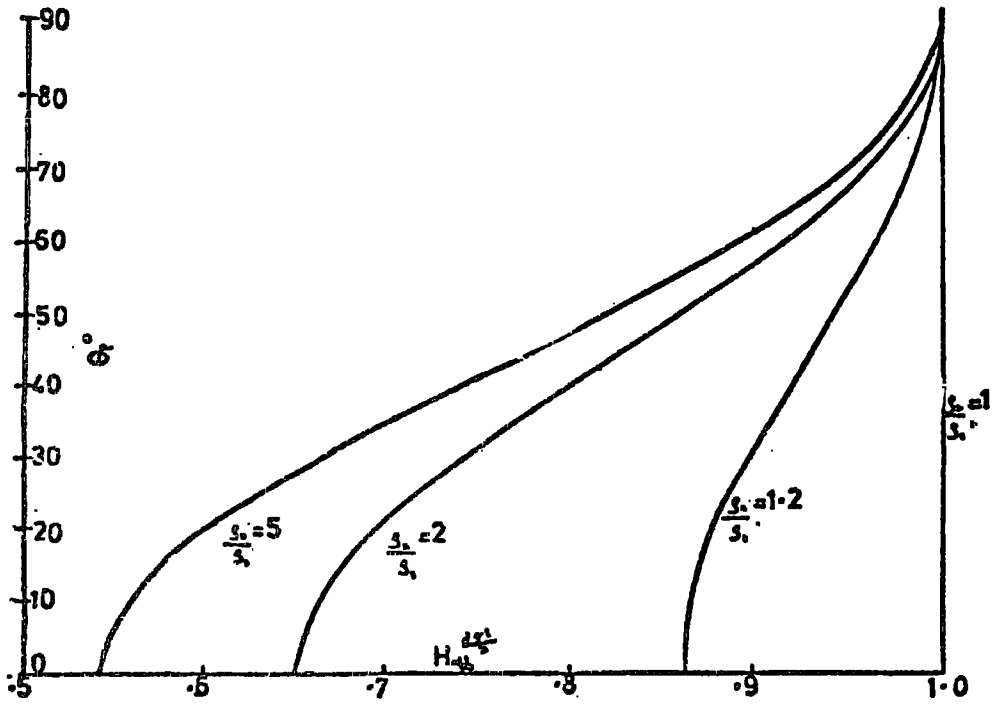

Fig. 2.7a

Variation of $H_{\phi\phi}^{\frac{d+1}{2}}$ with θ_p , for various compression ratios $\frac{s_2}{s_1}$.

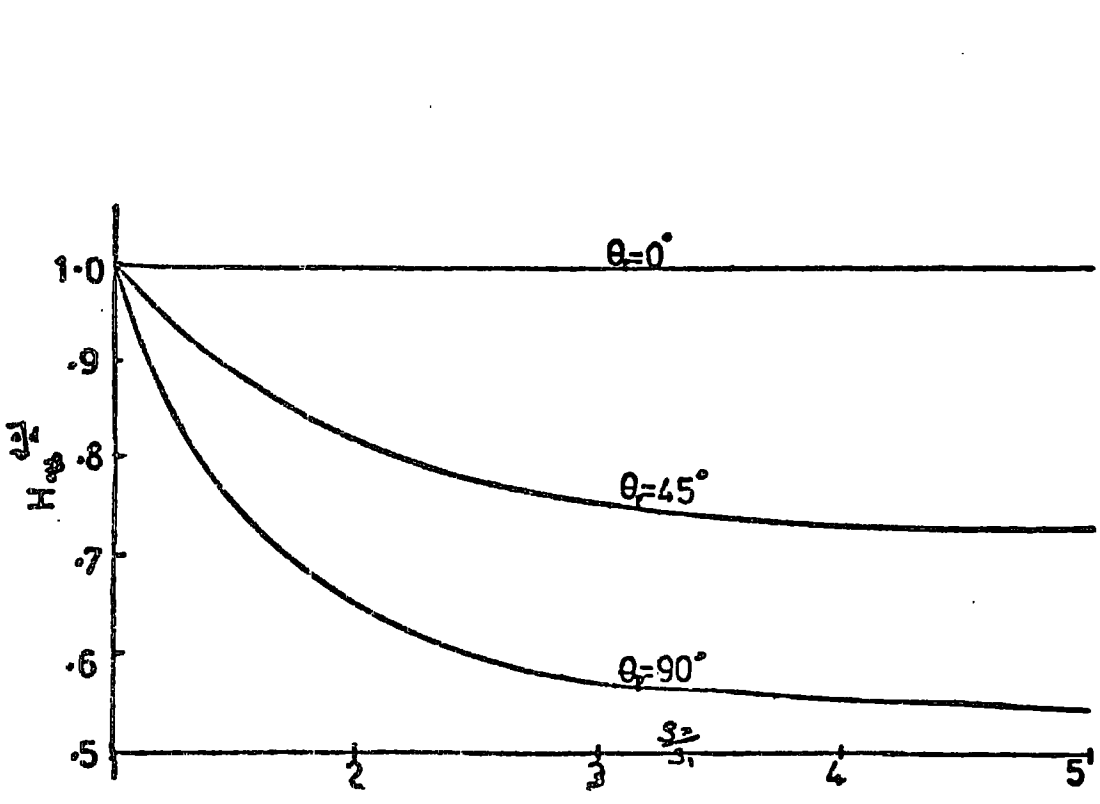

Fig. 2.7b

Variation of $H_{\phi\phi}^{\frac{d+1}{2}}$ with $\frac{s_2}{s_1}$, for various angles of θ_p .

2.4 Irregularities in the arms.

In the spiral structure used in the model of French the arms are fairly smooth (see Fig. 2.1). When radio observations of external galaxies were made, in particular M51, it was seen that the ridge lines of the arms are not smooth. The radio arms closely follow the dust lanes along the inner edge of the optical arms. This is the region where the gas is compressed the most, and hence the magnetic field, and the synchrotron emission is thus greatest here.

To investigate the effect of irregularities in the ridge lines, a simple model of the Galaxy was used. Three circular arms of radii 7, 10 and 13 kpc, concentric to the galactic centre, were used. The arms were then modified in amplitude, phase and frequency, by the relation

$$R = R + a\cos(b\phi + c), \qquad (2.17)$$

where ϕ is the angle between the line joining the observer to the galactic centre, and the line joining the centre to the point reached in the integration along the line of sight. The geometry of the two dimensional model is shown in Fig. 2.8, with the observer situated at 10 kpc from the centre.

The variation of the emissivity across an arm was represented by

$$\varepsilon = \exp(-\delta y) \qquad (2.18), \qquad y = (R - R_0)$$

is the distance to the innermost arm at the point being considered. The integration was performed out to a radius of 15 kpc, in longitude steps of 1° from 0° to 180°, the total emission being given by

$$\int_0^S \exp(-\delta y)\, ds \qquad (2.19)$$

for the case of an irregular magnetic field, and

$$\int_0^S \exp(-\delta y)\sin\theta\, ds \qquad (2.20)$$

for a regular one. θ is the angle between the line of sight and the magnetic field.

Different values of A, B and C were tried, the three arms being

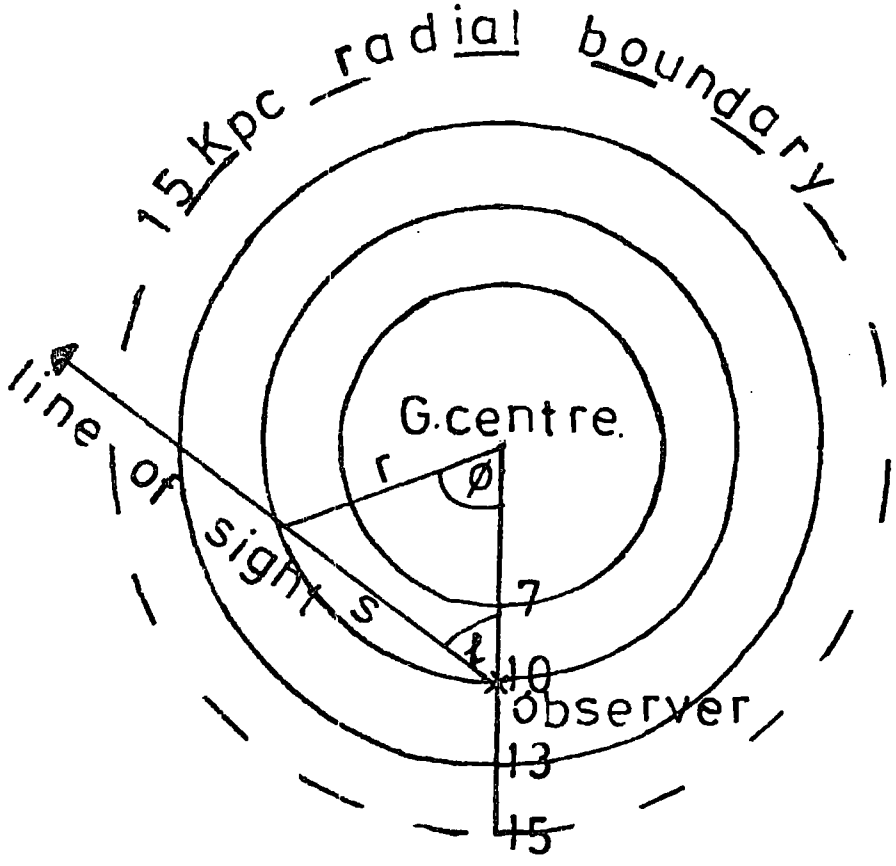

Fig. 2.8

Geometry of the model used to investigate the effect of arm irregularities on the synchrotron profile. Solid circles represent the unmodulated arms.

modified in exactly the same way. Plots of intensity against longitude were then produced, a sample of them being shown in Fig. 2.9 and Fig. 2.10. The former plots are for the emission due solely to the irregular field, and it is apparent that peaks are seen when the line of sight is tangential to a spiral arm, since in this configuration the path length through the spiral arm to the next arm is a maximum. On the other hand, when just the regular component of the magnetic field is considered, the spiral arms do not show up. This is because at the tangential points the angle θ is always very small, and therefore there is little emission from the regular field. When the arms are modulated, it is seen from Fig. 2.9 that multiple peaks arise in the emission from the irregular field. This is due to there then being several tangential points along the line of sight, with any one arm, over a small range of longitude. In the case of the regular component, high peaks are seen if the amplitude of the modulation is around one kiloparsec. This is much greater than the observed irregularities of around one tenth of a kiloparsec at the most, and so if the irregular field was superimposed on the regular one, the multiple peaks would mainly be due to the irregular component.

2.5 The Galactic plane profile.

The observed profile at 150 Mhz was obtained from the composite survey of Landecker and Wielebinski (1970). That shown as the dashed line in Fig. 2.11 follows the subtraction of thermal emission and the contribution of galactic loops, as described by French and Osborne (1976), together with a 50°K extragalactic background. The peaks close to $\ell^{II} = 270^{\circ}$ and $\ell^{II} = 90^{\circ}$ are due to the Vela supernova remnant and the Cygnus complex. The former is not part of the large scale synchrotron emission of the Galaxy, while the latter contains a large element of

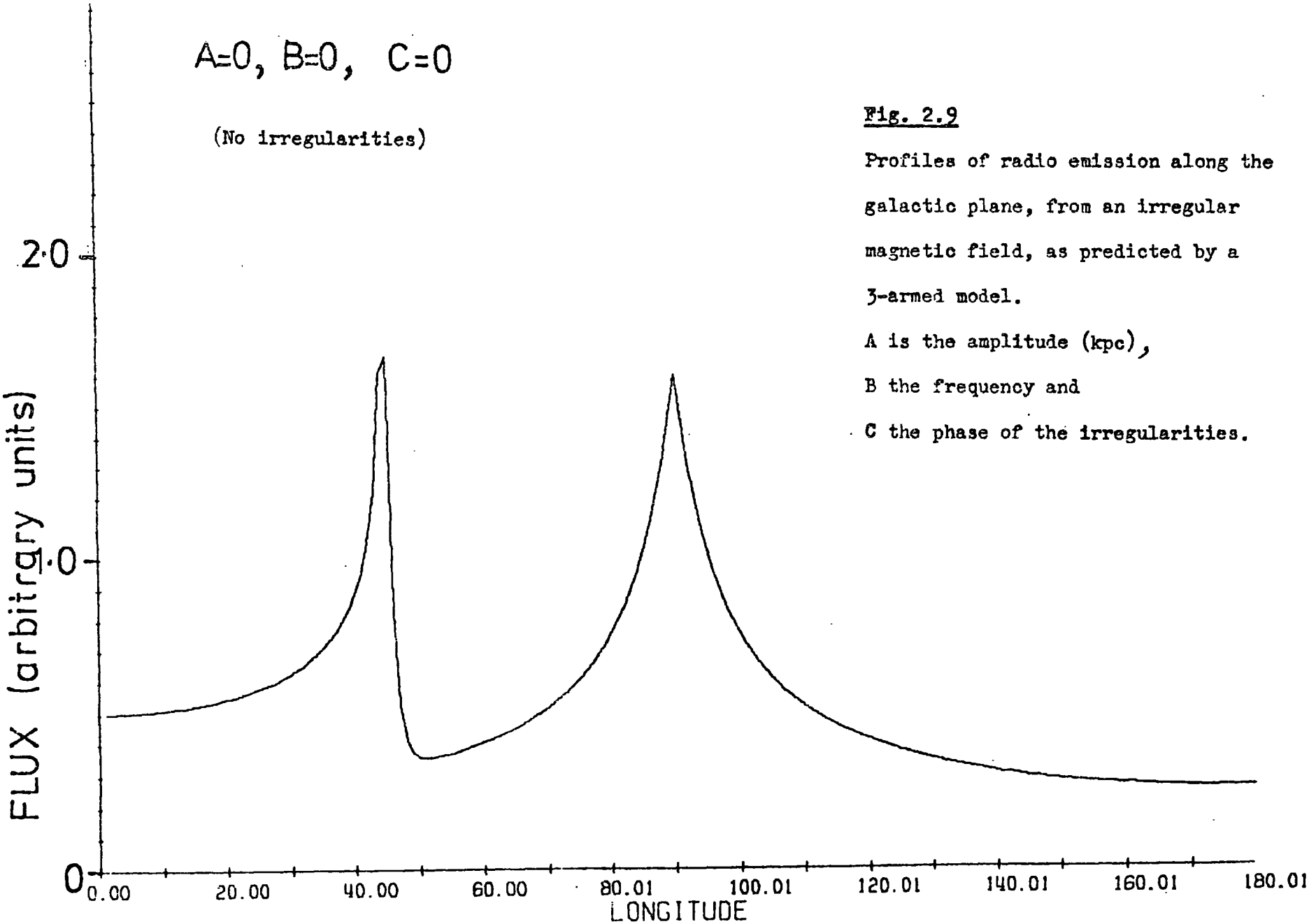

Fig. 2.9

Profiles of radio emission along the galactic plane, from an irregular magnetic field, as predicted by a 3-armed model.

A is the amplitude (kpc),

B the frequency and

C the phase of the irregularities.

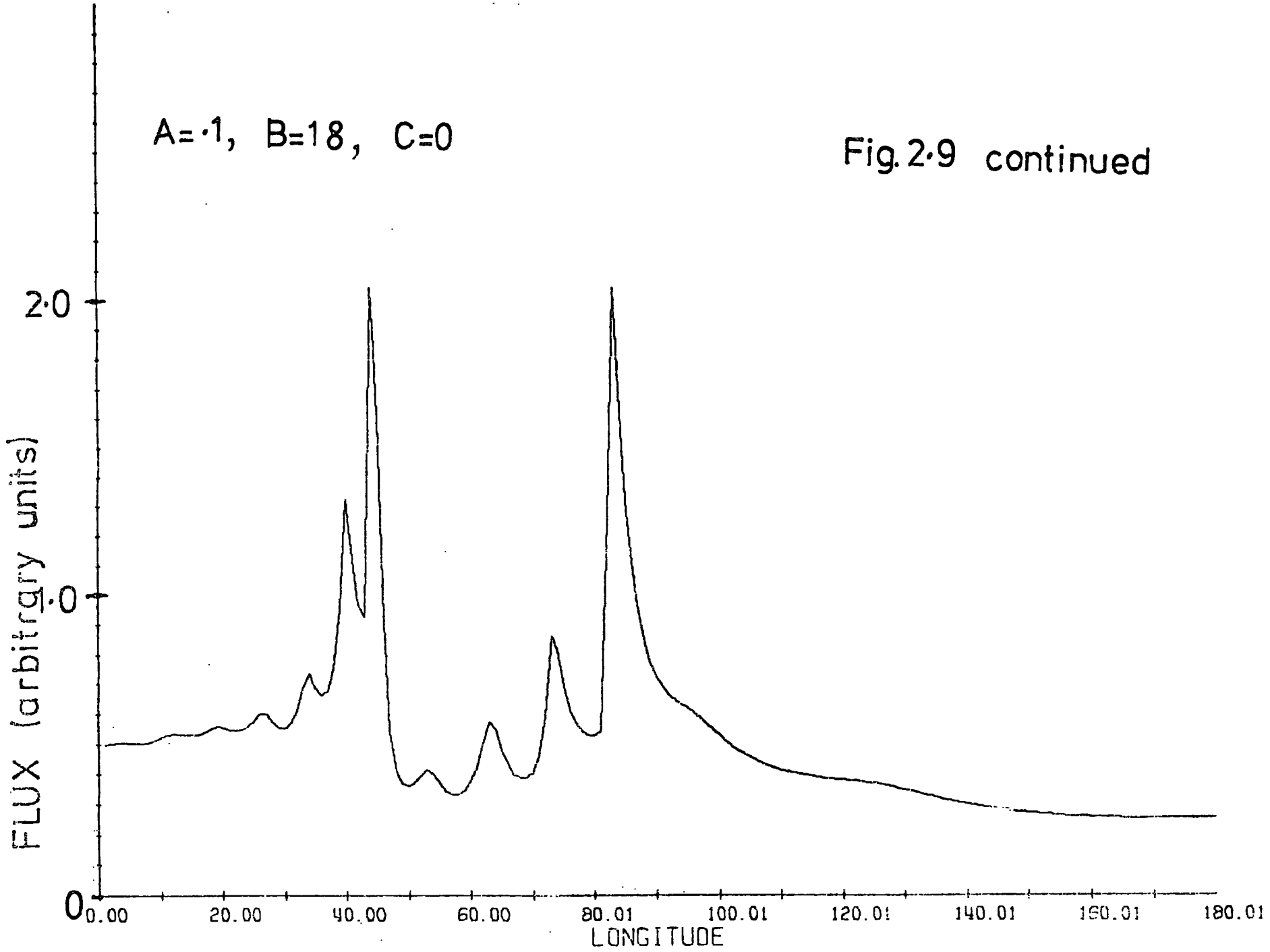

Fig. 2·9 continued

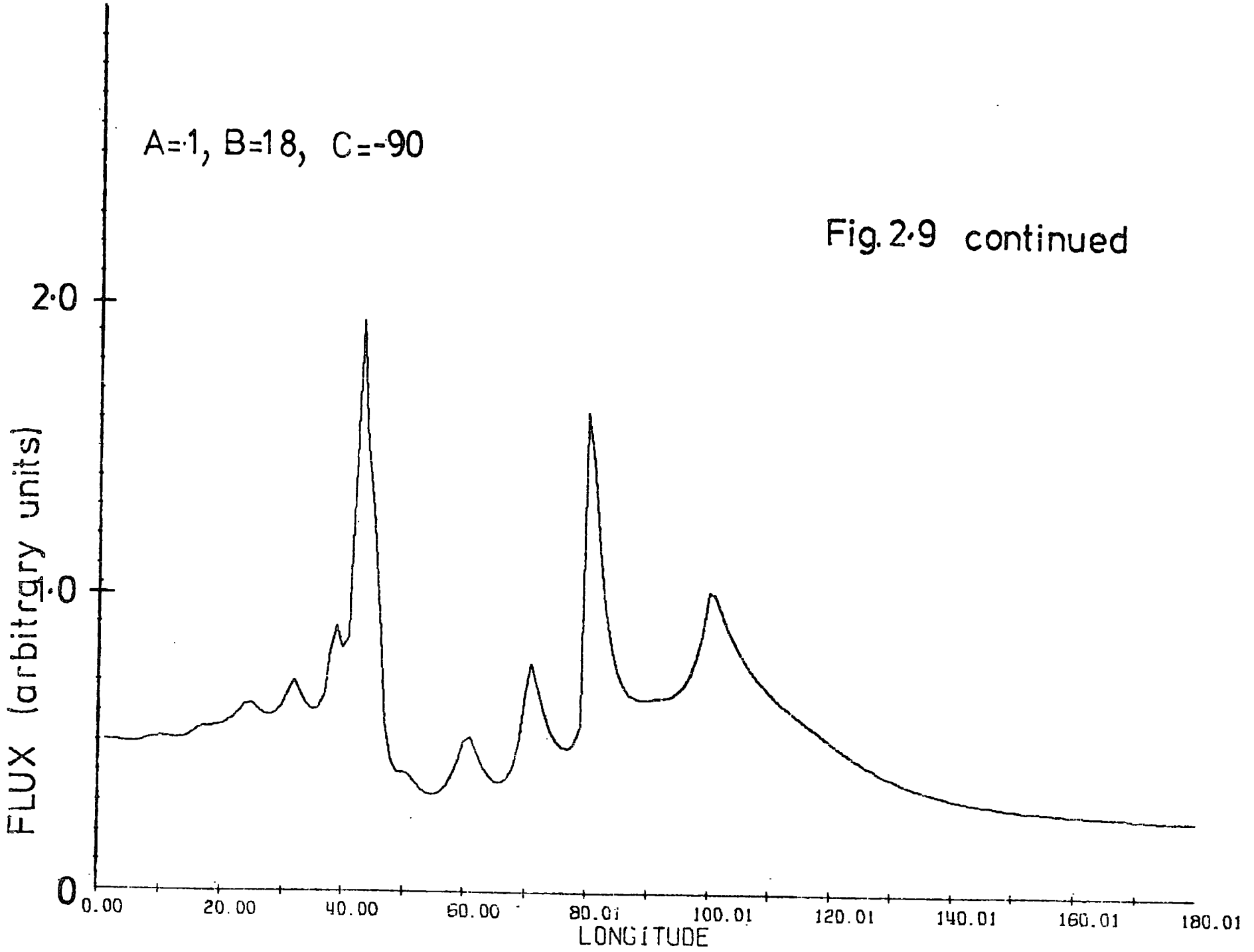

Fig. 2·9 continued

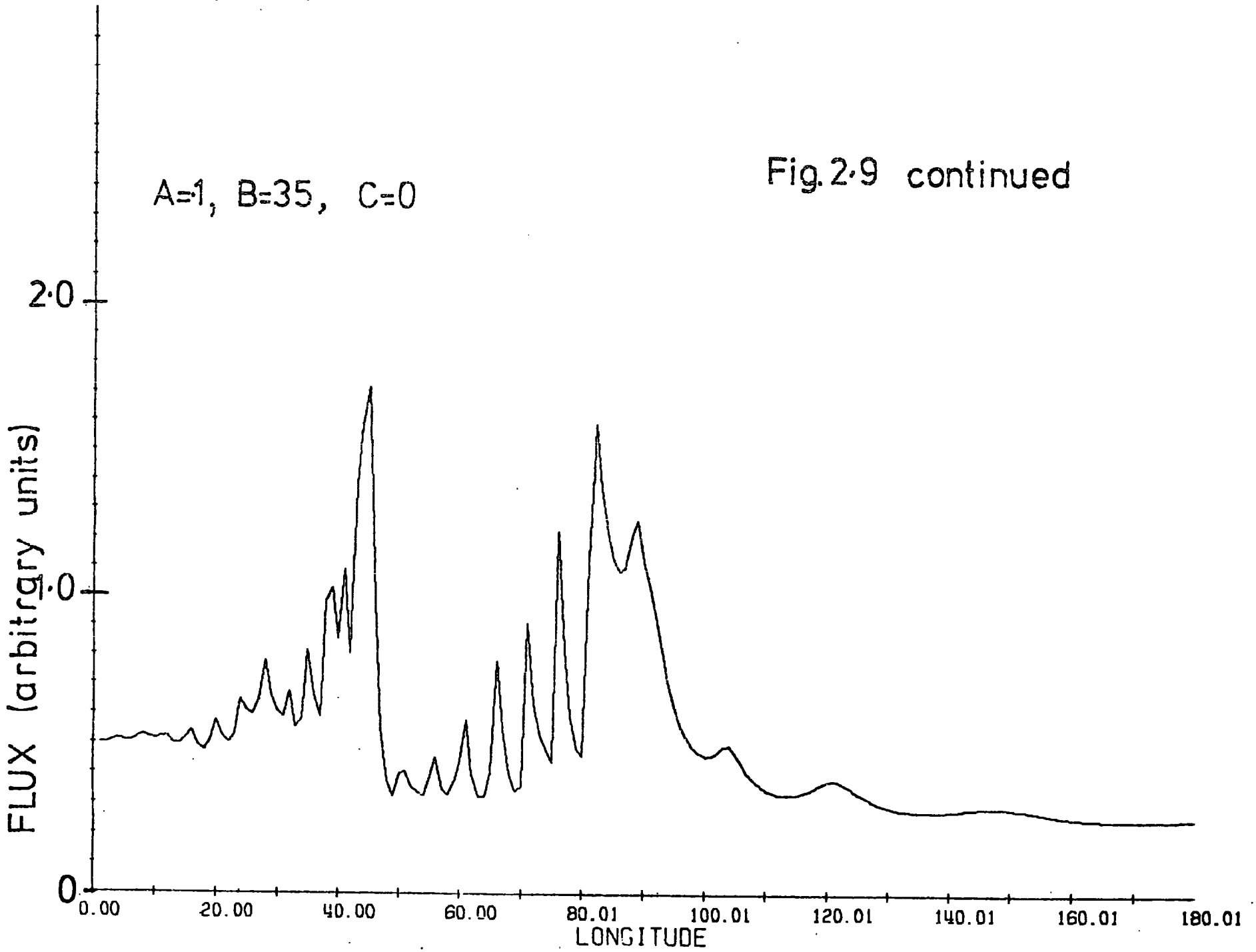

Fig. 2·9 continued

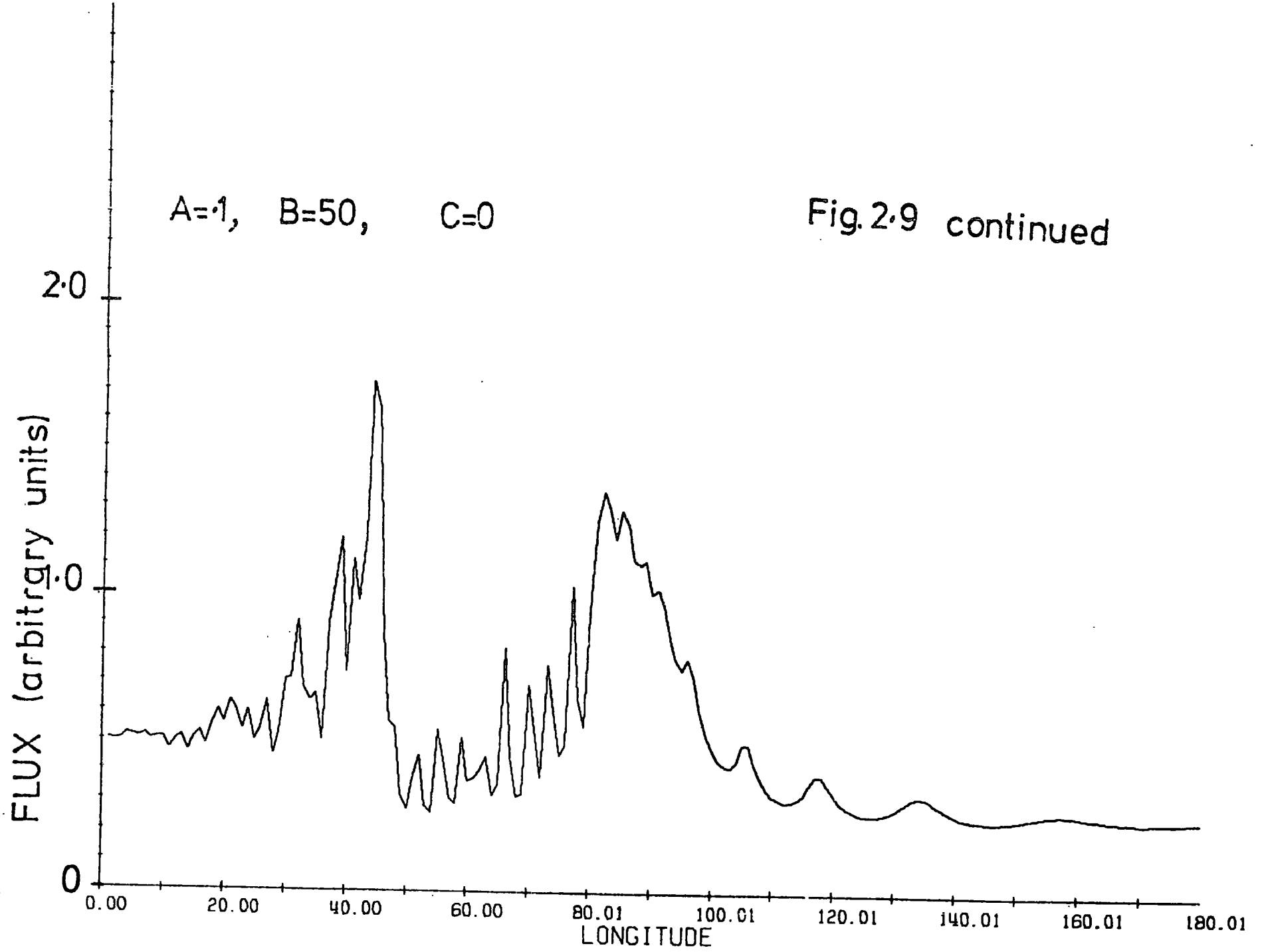

Fig. 2·9 continued

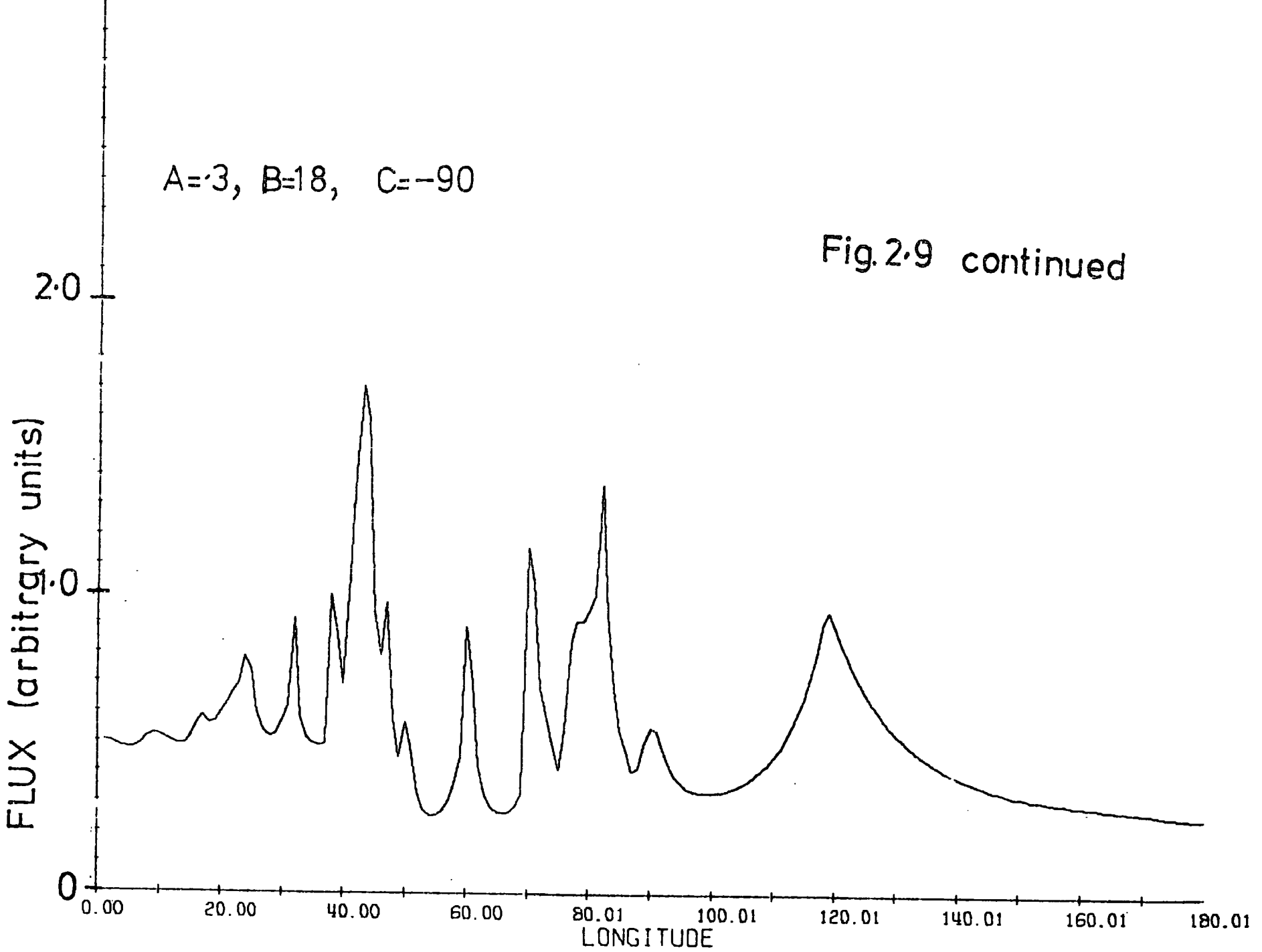

Fig. 2·9 continued

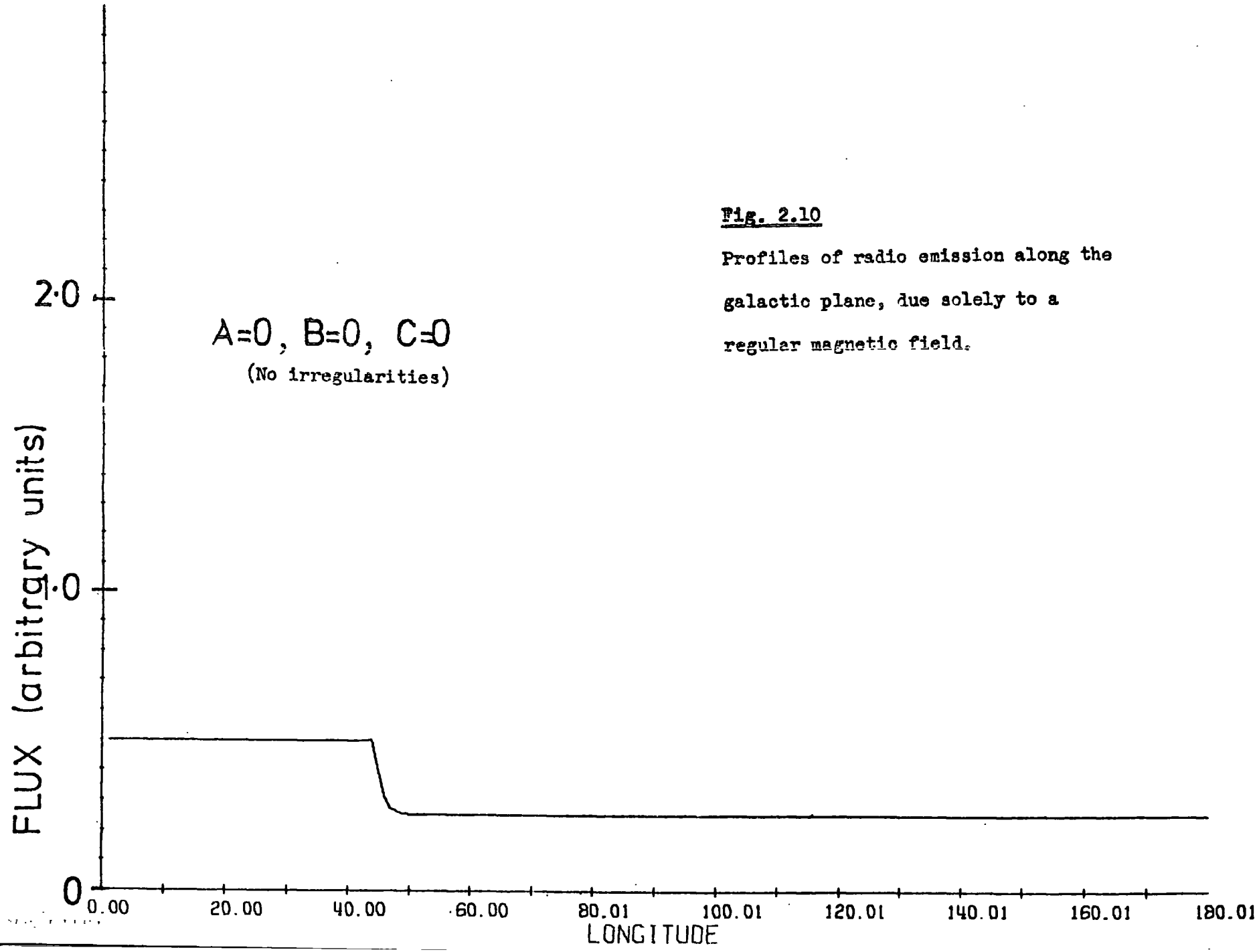

Fig. 2.10

Profiles of radio emission along the galactic plane, due solely to a regular magnetic field.

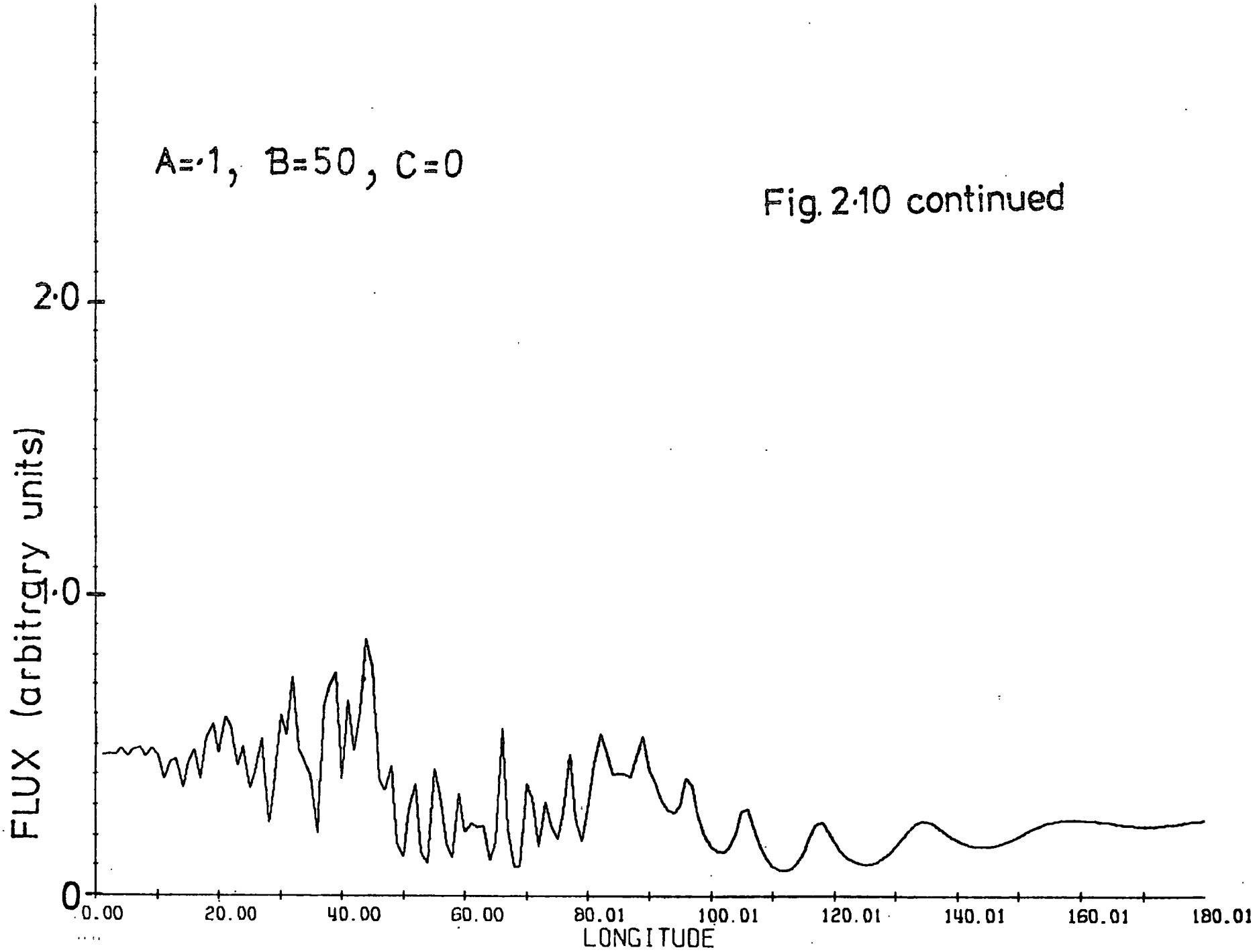

Fig. 2·10 continued

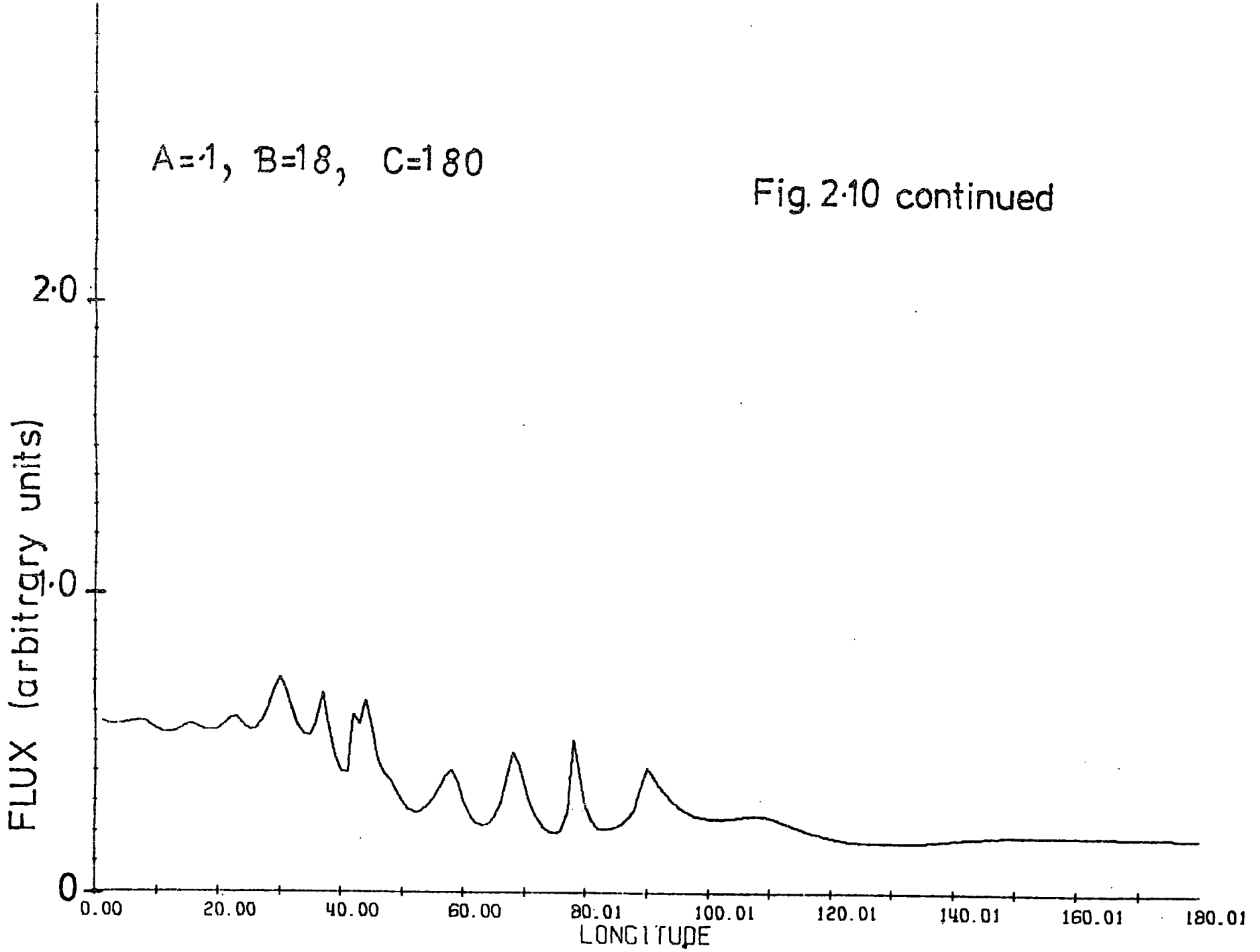

Fig. 2·10 continued

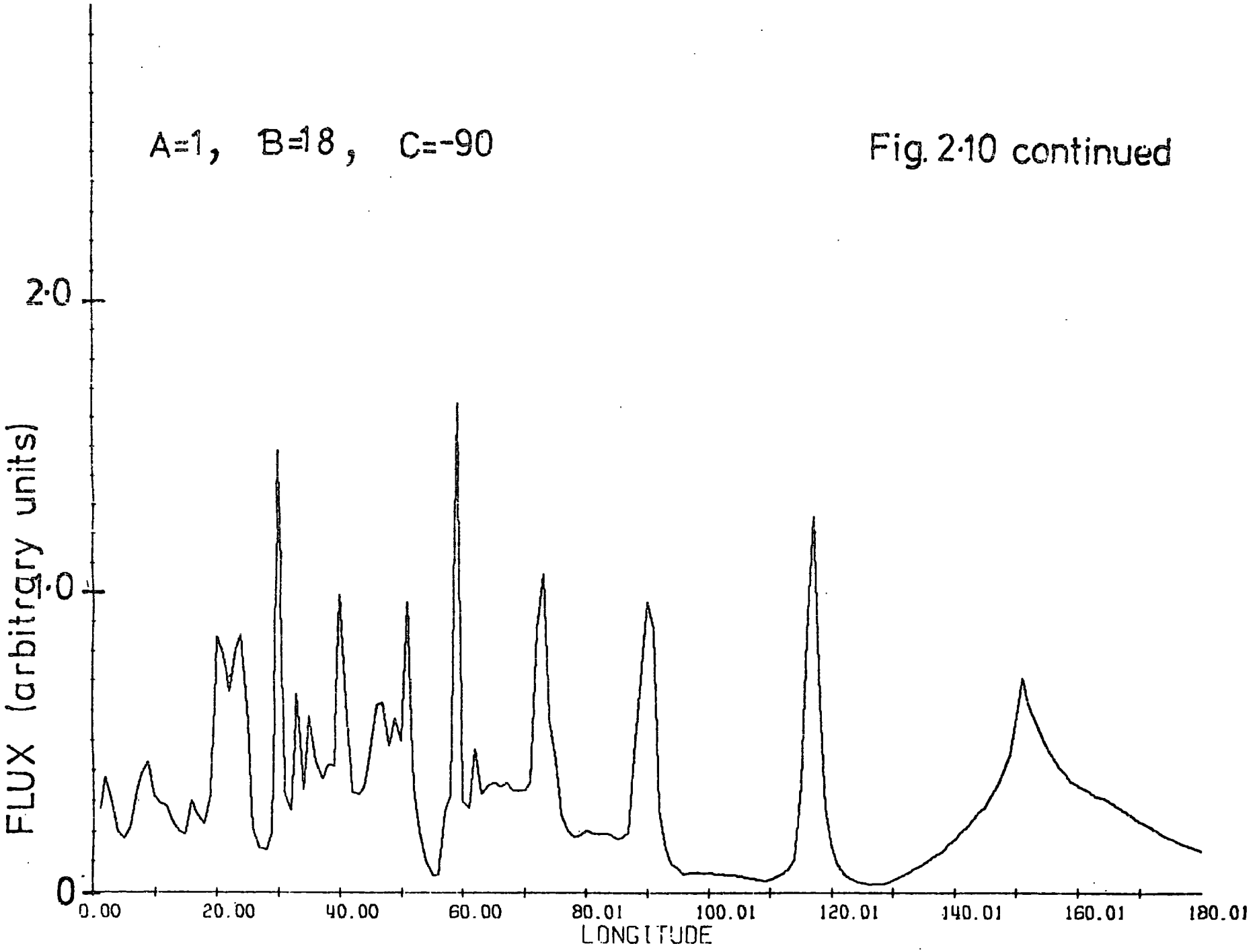

Fig. 2·10 continued

thermal emission. They were discounted in obtaining a fit to the profile.

As mentioned above, the values of the free parameters R_o^2 = 131 kpc^2 and F = 0.75 produced the best fit to the observations. This is indicated by the solid line in Fig. 2.11. No attempt is made to fit the observations within 30° of the galactic centre, due to the lack of information on spiral structure within the 3 kpc ring.

It can be seen that the observed profile has more rounded steps, in the directions tangential to the spiral arms, than the predicted profile, although the latter has been convolved to conform with the angular resolutions ($\sim 3°$) of the three surveys from which the Landecker and Wielebinski map was built up. In Fig. 2.12 these observations are compared with the 408 Mhz profile from the surveys of Green (1974) and Seegen et al. (1965), which has resolution in longitude of 0.5° and $\sim 2°$ respectively. It can be seen that there is good overall agreement in the brightness temperatures when they are scaled according to an electron spectrum having a differential exponent of 2.6. The higher frequency measurements show detailed structure in the steps in the profile which is similar to that obtained in section 2.4. There is in fact a real discrepancy in the observations in regard to these features. Although the lower frequency profile has poorer resolution, it should still be good enough to show most of the peaks appearing in the higher frequency profile.

The fit was made under the assumption of a constant electron density throughout the Galaxy. An electron density varying in proportion to the square of the magnetic field, leads to a profile which is too angular, and it is difficult to account for the measured emissivity in front of HII regions. Similar arguments, of rather reduced weight, can be advanced against a linear relation between field strength and electron density. The important feature of the model is that the electron density is not

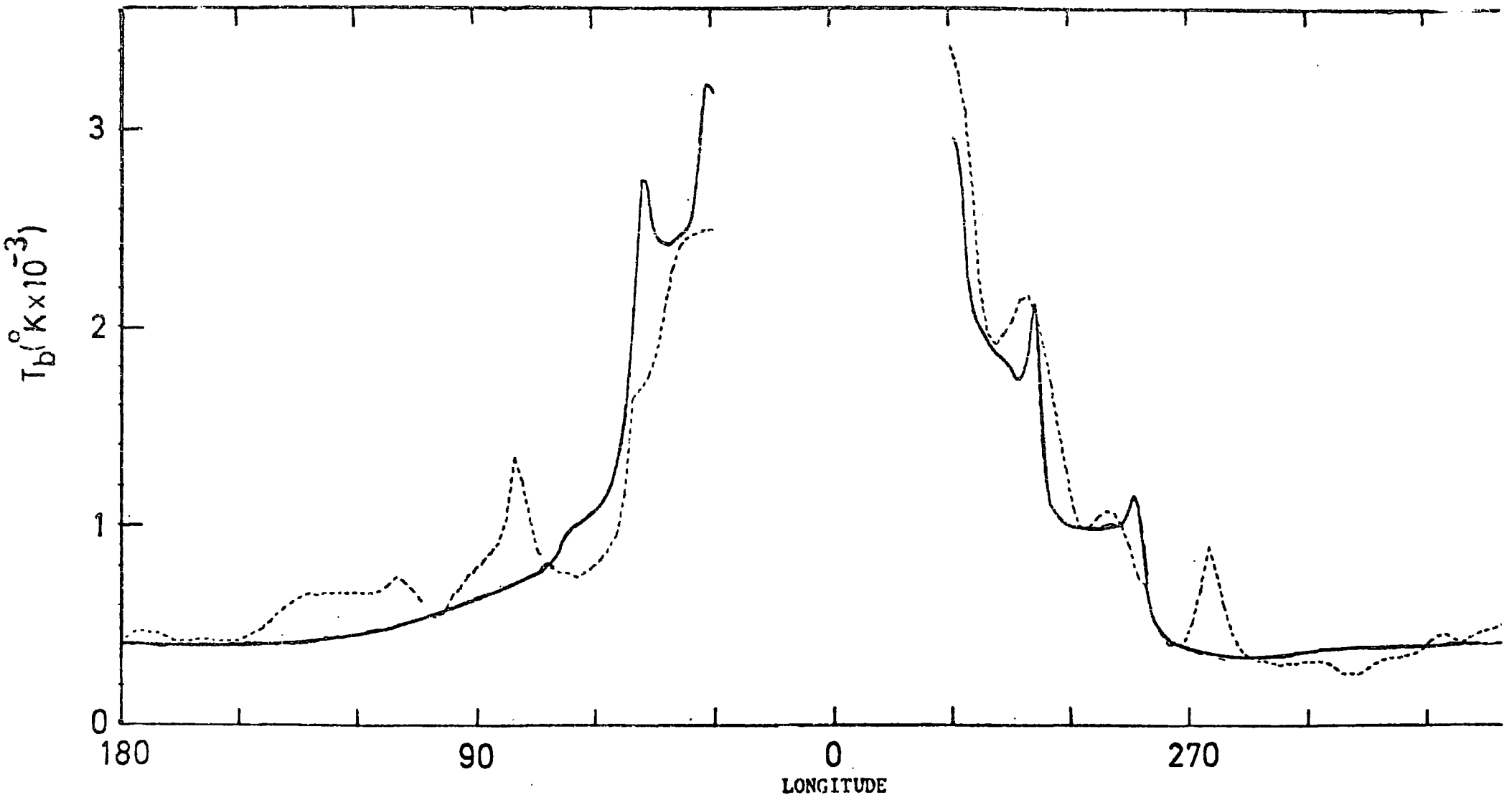

Fig. 2.11 Observed galactic plane longitude profile, from the Landecker and Wielebinski map (1970), after subtraction of extragalactic and thermal emission and that due to galactic loops, (French and Osborne, 1976).

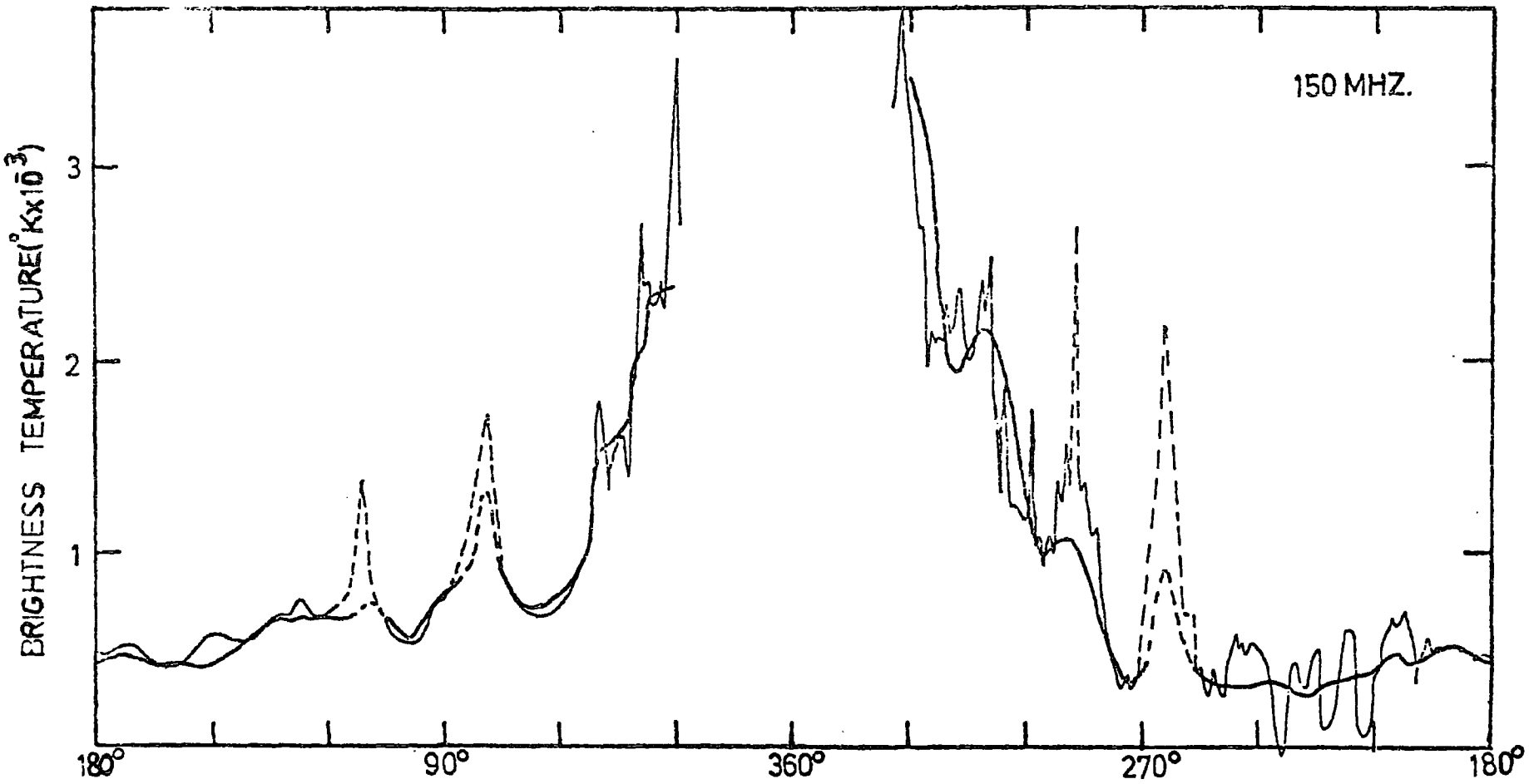

Fig. 2.12

Galactic plane profiles at 150 Mhz. —— profile from Landecker and Wielebinski map (1970). —— profile from surveys of Green (1974) and Seeger et al. (1965) scaled by $\left(\frac{408}{150}\right)^{2.8}$. Both profiles are corrected for extragalactic, thermal and spur emission. Dotted regions indicate emission from the following sources:-

1) Cas A supernova remnant ($l^{II} \simeq 112°$, $b^{II} \simeq -2°$)
2) Cygnus X complex ($l^{II} \simeq 80°$, $b^{II} = 0°$)
3) Vela supernova remnant ($l^{II} = 264°$, $b^{II} = -3°$)

modulated by the spiral arms. It is purely to simplify the calculations, that the overall radial decrease in emissivity is attributed solely to a radial decrease in magnetic field. A radial decrease in electron intensity is allowed, provided that the radial dependence of the magnetic field is adjusted to compensate and give the same emissivity variation.

An important feature of the model concerns the location of the Sun with respect to the local Orion arm of the Galaxy. It is generally agreed that this is a branch of the overall spiral pattern of the Galaxy, and that the Sun is near to its inner edge. The locally measured value of the regular component of the galactic magnetic field is 3 μ-gauss. To reconcile this with the general level of synchrotron radiation throughout the Galaxy, it is necessary to place the Sun in an interarm region, rather than in a region of compression. If the compression region of the Orion arm is then situated within a distance of 0.5 kpc in the anticentre direction, one can account for the relatively high values of emissivity measured in front of HII regions by Caswell (1976).

2.6 The Z - variation of the Emissivity.

Due to the variation of compression of the field in the arms with distance Z from the plane, discussed in section 2.2.2, there will be a rapid variation of emissivity with Z out to Z = 0.5 kpc, for the arm regions of the Galaxy. This will be superimposed on a more slowly varying emissivity applicable to the interarm regions, due to an overall decrease of magnetic field strength and electron density with Z. Brindle et al. (1978) consider various functional forms of the variation of the interarm emissivity $\varepsilon(Z, R)$, with the aim of accounting for the distribution of brightness temperature over the whole sky.

With the Sun in an interarm region, the local emissivity of 63 K kpc^{-1} requires that $\varepsilon(Z, R)$, at R = 10 kpc, has an equivalent half width of

2.75 kpc to account for the observed brightness temperature of 170° K at the poles, after the subtraction of the extragalactic contribution. Brindle et al. consider six different forms for $\epsilon(Z, R)$, which obey this constraint. The simplest case is that in which $\epsilon(Z, R)$ decreases linearly from its value at the plane, to reach zero at $Z = 5.5$ kpc. This corresponds to the simple diffusion loss model, which has often been applied to the propagation of cosmic rays in the Galaxy. The magnetic field remains constant at its value in the plane from the interarm region, while the variation of electron density is determined by considering sources at $Z = 0$, an absorbing boundary at $Z = 5.5$, and a constant diffusion mean free path. To account for the ratio of light to medium nuclei in the cosmic ray flux, the mean free path would be ~ 1 pc, in which case the characteristic energy loss time of the electrons of energies of a few GeV would be much greater than the escape loss time, and a linear decrease of electron density would be expected. Comparison of the predicted all-sky brightness temperature map with that observed, leads to the following conclusions. In the anticentre hemisphere the agreement is satisfactory. This is to be expected however, since the temperatures are made to agree at the Poles and in the anticentre direction at $b^{II} = 0°$, and the temperature varies by a factor of ~ 2 only between these two directions. Towards the inner parts of the Galaxy however, the predicted temperatures exceed those observed at intermediate latitudes. For example, at $l^{II} = 330°$ the predicted temperature is nearly two times too high at $b^{II} = 30°$.

A simple way to decrease this emission is to decrease the width of the emissivity distribution. The width at $R = 10$ kpc is fixed, however, so that the implication is that the width decreases as the galactic centre is approached. The scale height of the neutral hydrogen gas does follow this behaviour (Jackson and Kellmann 1974), decreasing to half the local

value at R = 4 kpc, and increasing to double at R = 15 kpc. The width of the proposed emission region is much greater than that of the gas layer, but as both depend on the balance between gas, magnetic field and cosmic ray pressures, and the gravitational force towards the plane, they may depend in a similar way upon galactic radius.

After considering a number of variants of $\mathcal{E}$ (Z, R) along these lines, Brindle et al. conclude that a best fit to the observations can be obtained with,

$$\frac{\mathcal{E}(Z,R)}{\mathcal{E}(0,10)} = 1 - 0.355\,Z/\omega(R) - 0.0473\left(Z/\omega(R)\right)^2 - 0.00213\left(\frac{Z}{\omega(R)}\right)^2,$$

where $\omega(R) = 0.59 - 0.65R + 0.0106R^2$. (2.21)

The Z - dependence is a polynomial approximation of an exponential decrease out to $^{Z}/_{W}$ (R) = 5 kpc, followed by a tail of essentially constant emissivity which cuts off at $^{Z}/_{W}$ (R) = 10.85 kpc.

Fig. 2.13 (Brindle et al. Fig. 6), is the all-sky contour map predicted by this model after the addition of the galactic loops and an extragalactic background. It may be compared with the observed map of Landecker and Wielebinski Fig. 2.14 (Brindle Fig. 5). It can be seen that the overall agreement is good, although there are some discrepancies remaining.

The aim in the succeeding chapters is to apply such models to the edge-on galaxies NGC 891 and 4631, and to make further comparisons with observations.

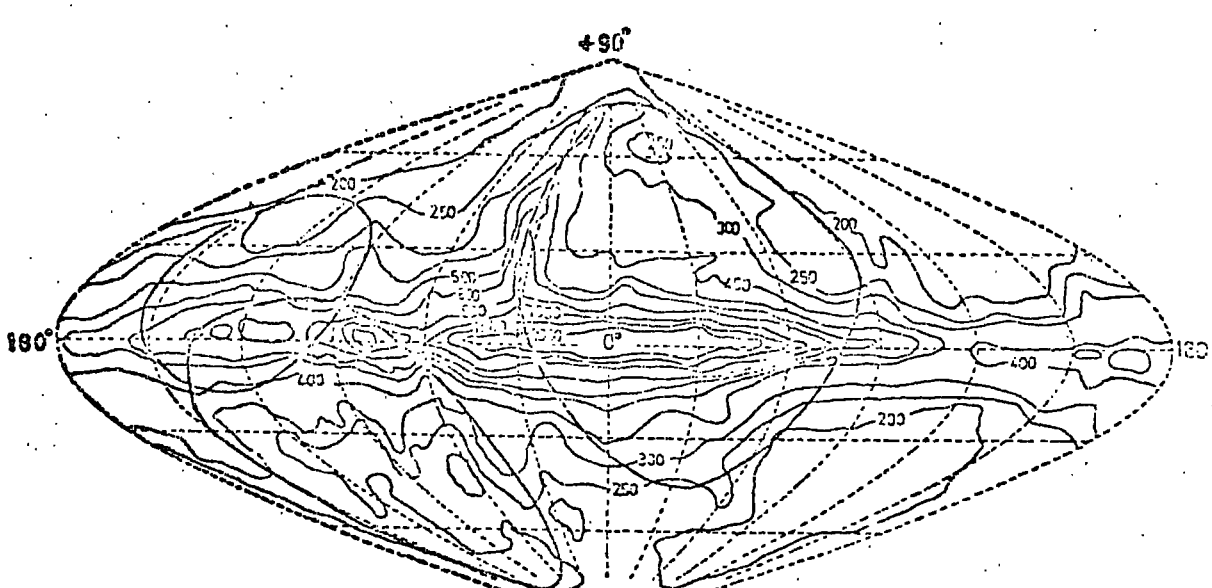

Fig. 2.14

The map of observed brightness temperature at 150 Mhz of Landecker and Wielebinski. The number of contour levels has been reduced to make comparisons easier.

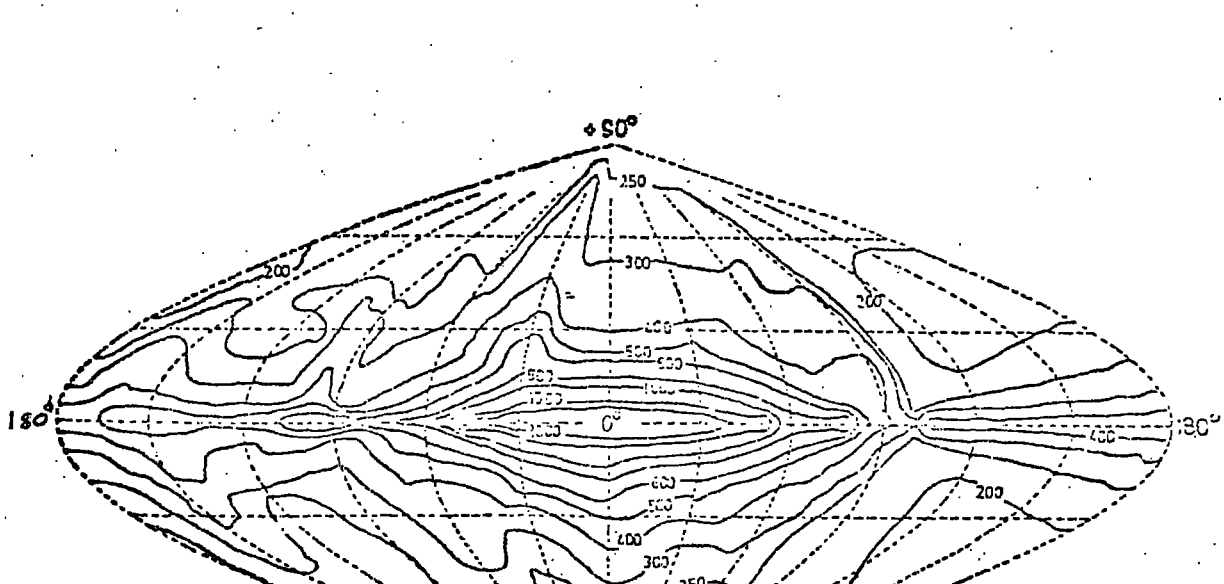

Fig. 2.13

The predicted map of brightness temperature, with an emissivity that varies with galactic radius and Z- distance. In the region $330° < l^{II} < 30°$, the model has been extrapolated.

Chapter 2 - References.

Brindle, C., French, D. K. and Osborne, J. L. 1978 Mon. Not. R. Astr. Soc. (in the press).

Caswell, J. L. 1976, Mon. Not. R. Astr. Soc. 177, 601.

French, D. K. and Osborne, J. L. 1976, Mon. Not. R. Astr. Soc. 177, 569.

Georgelin, Y. M. and Georgelin, Y. P., 1976. Astr. and Astrophys., 49, 57.

Green, A. J. 1974, Astron. and Astrophys. Suppl. 18, 267.

Jackson, P. D. and Kellman, S. A. 1974, Astrophys. J. 190, 53.

Landecker, T. L. and Wielebinski, R. 1970, Austr. J. Phys. Astrophys. Suppl. No. 16.

Price, R. M. 1974, Astron. and Astrophys. 33, 33.

Seegen, Ch. L., Westerhout, G., Conway, R. G., and Hoekenna, T. 1965. Bull. Astr. Inst. Netherlands. 18, 11.

Verschuur, G. L., 1973. Astr. and Astrophys., 49, 57.

White, M. 1977, PhD. thesis University of Durham.

Chapter 3

Comparison of NGC 891, NGC 4631 and the Galaxy.

3.1 Introduction.

High-resolution radio-continuum maps are available for NGC 891 and NGC 4631. Both these galaxies are relatively nearby galaxies and have inclination angles of between 85° and 90°, and are thus virtually 'edge-on'. They also have radio continuum emission at large Z distances above their galactic planes, and the Westerbork radio maps should enable some meaningful comparisons to be made between a model of an edge-on view of the radio-continuum emission of our Galaxy and the observations. The object of the next two chapters is to do just this. The purpose of the present chapter is to compare the three galaxies so that a meaningful comparison can be made.

3.2 Morphological Classification.

Since some of the physical properties of galaxies are correlated with the overall structure of the galaxy, it would be ideal if the three galaxies all had the same classification. The original Hubble sequence of galaxies (Hubble 1926), has been revised so that the spiral sequence now has the following stages : Sa, Sb, Sc, Sd, Sm and Im. Physical parameters such as, colour, nuclear concentration, resolution, and hydrogen content, vary steadily along this sequence. Spiral structure decays regularly through stages Sc to Im, being prominent but somewhat irregular at Sc, and vanishing or absent at Im. Half steps of the sequence are designated Sab, Sbc, · · · , Sdm. Types Sd, Sdm, and Sm, Im encompass the "Magellanic irregulars" group of Hubble's classification, but types Sd, Sdm, Sm show definite spiral structure, with irregularity increasing from Sd to Sm. Flattening towards an equitorial plane is maximum near

stage Sd where the axis ratio is $\simeq 1/10$. Both earlier stages Sb, Sc and the later stage Sm have larger axial ratios, about $\frac{1}{4}$ to $1/5$. There is a correlation between angular velocity and type, in that earlier stages (Sa -> Sc) rotate faster than later stages (Sc -> Sm), with typical rotation periods in the outer regions of spirals increasing from 3 to 10 x 10^7 years, in the early stages, to 3 to 10 x 10^8 years in the later stages. Studies have shown that barred spirals SB are as common and just as "normal" as the ordinary (non-barred) type, denoted SA in the revised classification system. Many galaxies also show transition characteristics noted SAB. The very late stage of spiral structure is encountered in both families of spirals, SA and SB. Among both types two distinct varieties are present, the ring type, noted S(r), in which the spiral arms emerge tangentially at the periphery of a circular (SA) or elliptical (SB) annulus, and the more peculiar spiral type, noted S(s), in which the arms emerge from the nucleus (SA) or at the opposite ends of a bar structure (SB). Both varieties are common and merge through the transition types S(rs) in which the ring is broken or fragmentary. From a sample of 1500 bright galaxies with revised types (de Vaucoleurs 1963b), 994 are classified as spirals and among them 31.3% are SA, 36.8% SB, 27.6% SAB and 4.3% have no family assignment.

Our Galaxy has a spiral structure intermediate between that of an Sb and Sc galaxy. The spiral structure has been mainly determined from the 21cm emission of HI and the study of the distribution of HII regions. Although the overall grand structure is still not known particularly well, the spacing of the nearby spiral arms is well determined, and this together with the brightness of the nucleus, is the basis of its classification (Tamman, 1975).

In the case of NGC 4631 its morphological classification is not well defined. Sandage (1961) classified it as late Sc, Morgan (1958) as S7

or Sl, G. and A. de Vaucoleurs (1963a) as a Magellanic-type barred spiral viewed along the bar. They interpreted this galaxy as an SB(s)d or possibly SB(s)m type, of a similar type to NGC 1313 or the Large Magellanic Cloud. This latter classification was based upon a detailed comparison with the Large Cloud, NGC 55, NGC 4C27, and other galaxies, and the assymmetry of the light distribution. They derived an angle of inclination of 85 ± 1° and found that the optical centre is shifted by 40" (~1 kpc) from the centre of symmetry of the best fitting rotation-curve, the shift being about the same as that between the optical centre and the bar of the Large Magellanic Cloud, and the centre of symmetry of the velocity curve. In 1966 de Vaucoleurs and de Vaucoleurs revised their classification of NGC 4631 to SB S7, and some time later to SBm. The difficulty in recognizing the spiral structure is due to the edge on aspect, it being particularly difficult to recognize barred spirals. Support for this classification has come from 21cm HI line observations (Robinson and Van Damme, 1964, 1966; Roberts, 1968). Both radio and optical studies disclose the characteristic asymmetry of the mass, luminosity and velocity distributions with respect to the bar. Although the detailed luminosity distribution in NGC 4631 had not been mapped in 1972, de Vaucoleurs and de Vaucoleurs interpreted the photographs as dust clouds seen projected against the bar and in the region where the main arm and secondary arms emerge from the bar (see fig. 3.1).

NGC 891 is a late Sb type with an inclination of around 88°. The classification is based upon the brightness of the nucleus, the brightness of the nucleus decreasing in the sequence Sa, Sb to Sc. On optical photographs the galaxy is seen to be surrounded by an absorbing ring, partially resolved into distinct clouds (Dufay, 1968). Infrared observations by Osterbrock and Sharples (1952) of the Milky Way, supports the claim that NGC 891 is similar to the Galaxy. In the infrared the dark rift in the Milky Way runs all the way through the galactic bulge. The structure

of the galactic rift is regular and sharply defined, particularly near the nucleus. There is a very rapid decrease in surface brightness of the Milky Way from the galactic bulge northwards. The two observers found the similarity with NGC 891 very pronounced. In both cases the nuclei and dark rifts are of the same form, and there is a steep gradient of light from the centre of the galaxies out to the edges. In the Hubble Atlas of Galaxies, Sandage draws attention to dust filaments extending to heights of about 1 kpc normal to the equatorial plane, which do not exist in the Galaxy (see fig. 3.2).

3.3 Distances.

The distance to NGC 4631 has been estimated by various people to be between 3 and 15 Mpc. Using diameters of H II regions, Sérsic (1960) placed NGC 4631 in the Ursa Major II Group of galaxies, and assigned it a distance of 5.2 Mpc. This group lies in the region of the Canes Venatici cluster as defined by Van den Bergh (1960). From galaxy luminosity criteria he placed the cluster at a distance of 4.4 Mpc, and assigned NGC 4631 to the CVn cluster. The distance was also adopted by de Vaucoleurs and de Vaucoleurs (1963a) in their optical study of the galaxy. In a later discussion of groups of galaxies, de Vaucoleurs (1976) placed NGC 4631 in the CVn II cloud, at a distance of 8 Mpc. The CVn II Cloud membership is similar to Sérsic's Ursa Major II Group. de Vaucoleur's CVn I Cloud, at 3.8 Mpc, is similar to Sersic's Ursa Major 1 Group. Corrections to the distance scales adopted by Sersic and Van den Bergh were proposed by Sandage (1962) and de Vaucoleurs (1976) recalibrated Van den Bergh's luminosity class. Sandage (1974), in his attempt to obtain an accurate value for the Hubble Constant, obtained the distances to 39 late-type (Sc - Sd - Sm - Ir) nearby galaxies, including NGC 4631. He measured the angular sizes of the three largest H II regions, and obtained a distance of 5.2 Mpc to NGC 4631. From these distance measurements

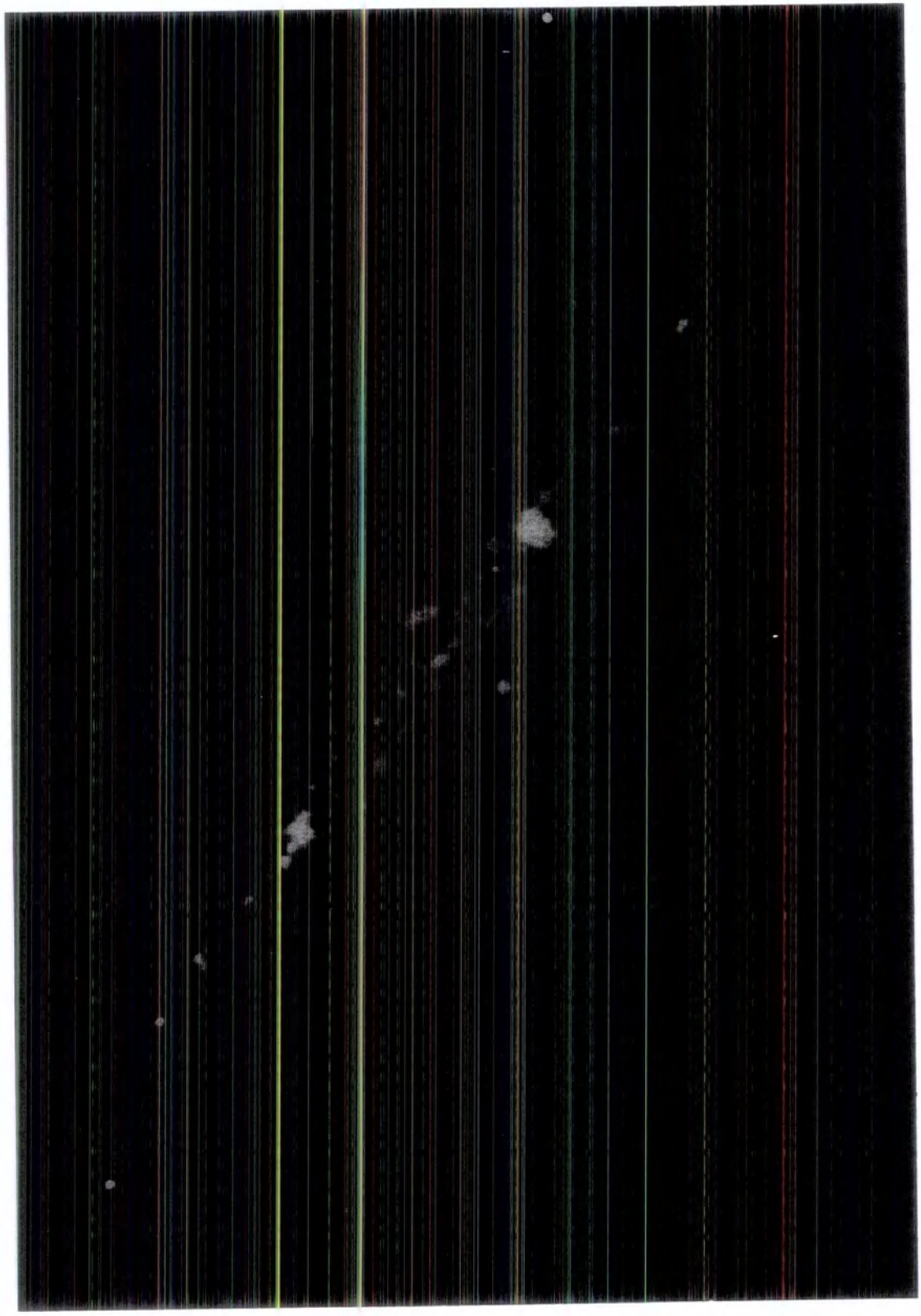

Fig. 3.1 NGC 4631 in blue light.
McDonald Observatory, 82-inch reflector.

Fig. 3.2 NGC 891 in Andromeda.
Mount Wilson, 60-inch reflector.

Sandage and Tammann computed a value for the Hubble constant of 57 ± 6 Kms^{-1} /Mpc.

This method of using the diameters of the largest HII regions, was first mentioned by Dufay (1952). It relies on the existence of an upper limit to the physical size of HII regions in a given galaxy, but since this limit is not very well defined, there is some uncertainty as to the reliability of the method. Superassociations exist (e.g. 30 Doradus in the Large Magellanic Cloud) which are ~ 5 magnitudes brighter than the next brightest HII regions, which means that the "largest" HII region may vary widely from one galaxy to another. It is also very hard to actually define the diameter of an HII region on a photographic plate. Sandage and Tammann considered two diameters, a "core" diameter and a "halo" diameter, but these terms are themselves not well defined.

To calibrate this distance scale distances to Local Group objects such as LMC, SMC and M33 have to be known accurately. The Galaxy cannot be used for this purpose because interstellar obscuration could hide the three largest HII regions. Due to the uncertainty in the amount of extinction at the galactic poles these fundamental distances are still not known very accurately. Sandage and Tammann maintain that there is no extinction while researchers such as de Vaucoleurs believe that the extinction is around 0.2 magnitudes.

Since late type spirals and the Magellanic Clouds have many more O-B stars per unit mass than do early spirals, the method is restricted to galaxy types Sc and later. Also because the apparent size of the HII region on the photographic plate depends on a number of observational factors such as plate scale, exposure time, seeing etc., there is a great risk of systematic errors (Hodge 1975, Smith 1976, de Vaucoleurs 1976b). De Vaucoleurs (1977) points out that the method is also not self consistent and that there are too many uncertainties in the procedure to be able to use it with precision at the present time. He plotted log V_o against

log θ , where V_0 is the recessional velocity of the galaxy and θ the average size of the three largest HII regions, and found that the result was not a straight line in accordance with $\theta \propto V_0^{-1}$, which follows from Hubble's law $V_0 \propto \Delta$, where Δ is the distance.

Teerikorpi (1976) reanalyzed the data on nearby Sc galaxies provided by Sandage and Tammann, in order to take into account the luminosity selection effect still existing in the velocity range $V < 2000$ km S^{-1} Mpc^{-1} . He calculated H to be 41 ± 3 km S^{-1} Mpc^{-1} , assuming the Sandage Tammann calibration for bright luminosity classes to be valid. Noonan (1977) obtained a value for the Hubble constant from galaxy rotation curves. The linear radius (8 ± 1 kpc) of the maximum rotational velocity in the Galaxy, with the angular radii of maximum rotational velocity in other galaxies, enabled him to obtain a value for H of $54 \pm^{58}_{28}$ km S^{-1} Mpc^{-1} . Lynden-Bell (1977a) obtained a value for H of 110 km S^{-1} Mpc^{-1} , by applying Perrine's "light-echo" theory to observations of 3C 120 and 3C 273. This value is close to the value advocated by S. van den Bergh and G. H. de Vaucoleurs, but the value causes a problem in that the age of the Universe is then less than 9×10^9 years, whereas the oldest stars in the Galaxy are around 12×10^9 years.

It is clear that the distances to extragalactic objects beyond the Local Group are uncertain by about a factor of two. Thus, true linear extents of radio halos of external galaxies are uncertain by this amount and their luminosities by a factor of four.

The Hubble distance of NGC 4631, assuming H = 55 kms^{-1} /Mpc is 11 Mpc. In this thesis the value of 5.2 Mpc will be used, this giving a scale of one minute of arc approximately equal to one and a half kiloparsecs.

NGC 891 is a member of the NGC 1033 group of galaxies. After correction for galactic rotation, and taking H to be 55 Kms^{-1}/Mpc the distance to NGC 891 is 13.0 Mpc. A distance of 14 Mpc will be assumed in

this thesis, giving a scale of one minute of arc approximately equal to four kiloparsecs.

3.4 Linear Sizes.

The Holmberg radius for the Galaxy is 15 kpc. This radius is that at which the blue photoelectric surface brightness has fallen to 26.6 mag. $sec.^{-2}$ This is about the limit that one can see by eye inspection of Palomar Sky Survey blue prints.

The optical dimensions of NGC 4631 (Holmberg 1958) are 19.0' x 4.4', corresponding to a linear size of about 28 kpc x 6 kpc, at the adopted distance of 5.2 Mpc. These are the same as the dimensions published by Danver (1942), but the two photographs published by G. and A. de Vaucoleurs (1963a) show images of the disc only about 50" wide.

In the case of NGC 891, Kormendy and Bahcall (1974) measured the extent along the major axis as 13.3' (53 kpc) diameter at 25.9 mag. $(arcsec)^{-2}$ in the green ($\lambda\lambda$ 3900 - 5400Å). The usual quoted optical dimensions of the image of NGC 891 are 12' x 1', corresponding to a linearsize of about 48 kpc x 4 kpc.

3.5 HI Distribution.

3.5.1 The Galaxy.

The HI gas is concentrated in the spiral arms. An overall major pattern can be seen, but there is a great deal of splitting and interconnection of the main features. In the few places where spiral arms stand out clearly, there is an arm-interarm contrast of density of around 5 to 1. Most of the gas is confined to a disc shaped region, with a thickness at half intensity of a few hundred parsecs. Outside the Solar radius the gas appears to depart significantly from the plane. In the longitude range $l^{II} \sim 20^{\circ}$ to 140° it lies above the plane, and in the range $l^{II} = 240^{\circ}$ to 340°, below the plane (Kerr and Westerhout 1965). This warp can be explained by the tidal effect of the Magellanic Clouds (Hunter and Toomre, 1969). Weak HI emission has been found extending from the plane to Z - distances of 3 or 4 kpc (Habing, 1966; Kepner, 1970; Verschuur, 1973). The low latitude survey by Weaver and Williams (1973) shows gas extending 1 - 2 kpc above spiral arms, the amount being a few per cent of the peak arm intensity. Observations have been made of high velocity clouds ($V > 70$ km s^{-1} relative to the Local Standard of Rest), which do not appear to be related to the spiral structure. There is a preponderance of negative velocities in the region at positive latitudes between $l^{II} = 40^{\circ}$ and 190°, coinciding with the tilt of the galactic plane. In the Southern sky the velocities of the clouds are mainly positive. The sense of both of these velocities is the same as that due to galactic rotation, but the magnitude of the velocities is larger. According to Oort (1966, 1969, 1970), these clouds are material that is moving into the galaxy. Another interpretation is that the gas has been ejected from the arms due to the Parker instability.

According to Verschuur (1973) the HI layer broadens out considerably

in the outer regions, the thickness between half-intensity points increasing from 80 - 100 pc near the centre, and 200 pc in the solar region, to 3 kpc at distances of 16 kpc from the galactic centre.

In a HI study using the 18-meter reflector at Parkes, a long filament of gas, extending from the region of the Small Magellanic Cloud to the South Galactic Polar cap and beyond, was discovered. This so-called "Magellanic Stream" had been suspected for some time from star counts. The gas follows a great circle over its entire 180^{c} across the sky. Assuming all the HI in the stream to be at the distance of the Small Magellanic Cloud (63 kpc), the mass would be about 10^{9} $M_{\odot}$ Computer simulations have shown that gravitational interaction between the SMC. and the galaxy could have pulled the HI from the SMC. The radial distribution of HI is shown in figure 3.3a (Jackson and Kellman 1973), and the Magellanic Stream in fig. 3.3b and fig. 3.3c.

3.5.2 NGC 4631

HI gas streaming along the line of sight near the centre of the galaxy has been observed, and interpreted by some, notably G. and A. de Vaucoleurs, to be gas streaming along a bar. An early estimate by Epstein (1964) of the total hydrogen mass is $(3 \pm 2) \times 10^{9}$ $M_{\odot}$, the total mass flowing in the two halves of the bar being about one solar mass per year. The derived hydrogen mass of Winter (1975) is 4.9×10^{9} $M_{\odot}$. NGC 4631 has a companion galaxy about 50 kpc away, 30′ to the South East. This galaxy, NGC 4656, is probably of type IRR1. A third galaxy, NGC 4627, lies 2′ North of the centre of NGC 4631. HI observations have shown that there is a bridge of HI extending from NGC 4631 to NGC 4656. Observations have also shown that there is HI at distances up to 12 kpc above the plane of NGC 4631, and also that there is complex structure in the bridge joining the galaxies. No optical counterpart of this material is visible on the Palomar Sky Survey prints, but a photograph by Arp (1966) shows

optical emission up to 2′ (~ 3 kpc) above the plane. The material has a wide range of velocities, the mass being estimated as 10^9 $M_\odot$, assuming negligible self-absorption. A rotation curve fitted to the HI observations shows that the eastern half of the galaxy could be disturbed, due to its companion NGC 4656. The rotation curve of NGC 4656 shows that it has a disturbed velocity field, the estimated mass being 1.8×10^{11} $M_\odot$. Computer simulations have shown that the bridge could have been formed by a tidal interaction between the two galaxies. The same interaction could also have produced the large Z-distribution in NGC 4631, although it is possible that NGC 4627 could be responsible. The mass of NGC 4627 has been estimated as being $^1/16$ of that of NGC 4631, assuming it is an elliptical galaxy with an $^M/_L$ ratio of 10. If it orbits close to NGC 4631 then tidal forces could have raised the HI from the plane to heights of several kiloparsecs. Fig. 3.4 shows a map of the HI distribution between the two galaxies.

3.5.3 NGC 891.

The HI distribution has been mapped by the Westerbork aperture synthesis telescope. The results obtained are consistent with a thin disc of HI of thickness $\leq$ 500 pcs, inclined at about 2^o to the line of sight. In the plane the HI does not extend to larger distances from the centre than the optical image on the Palomar Sky survey prints. No traces of HI have been found outside the disc in the Z direction. Asymmetry has been observed in the HI distribution between the Northern and Southern sides, the Northern side having stronger emission, while the emission from the Southern sides extends to a larger radius. The Westerbork map of the HI distribution is shown in fig. 3.5.

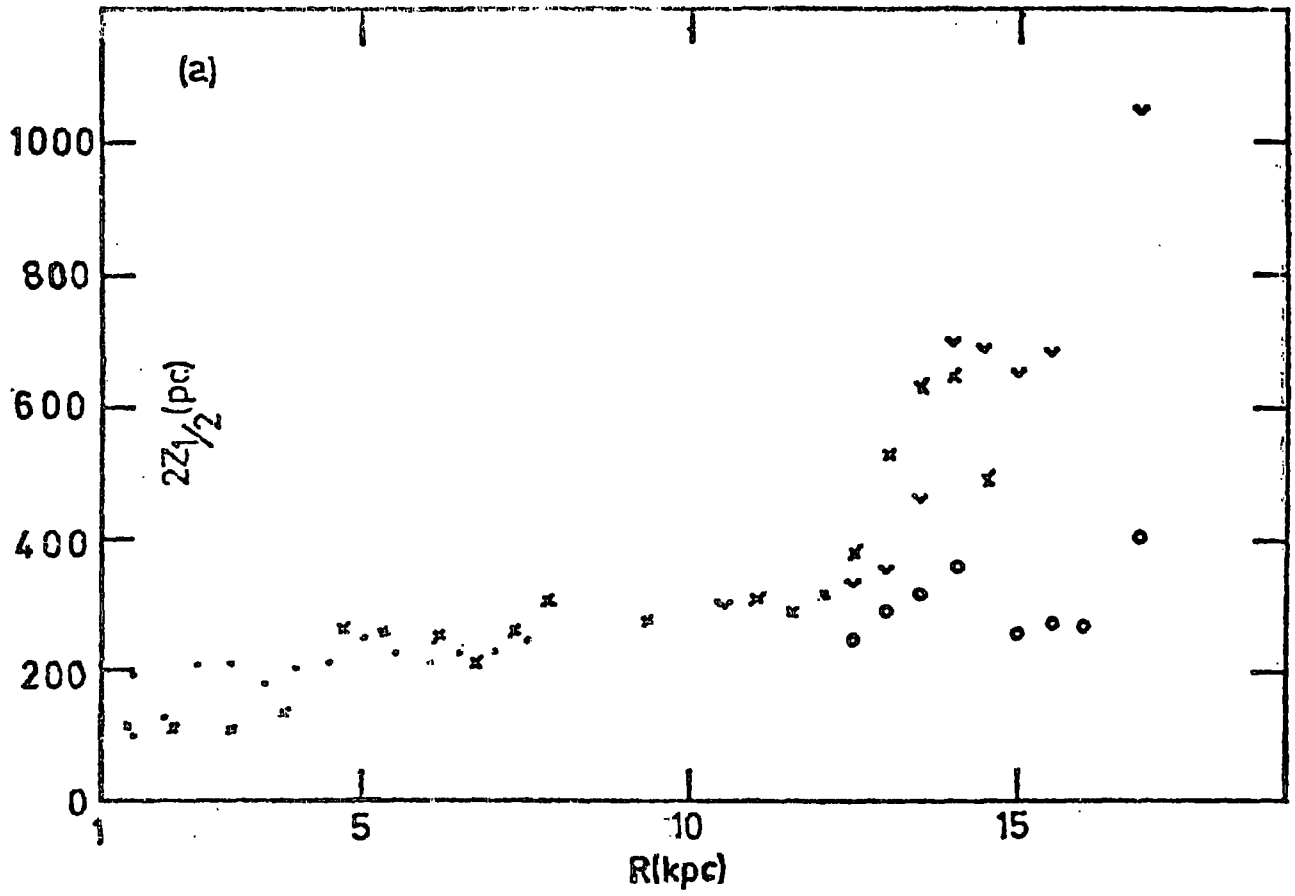

Fig. 3.3a

Variation of the full width at half maximum of the HI gas with distance from the galactic centre, (Jackson and Kellman 1973).

ν — l^{II} = 200° - 300°

$\times$ — l^{II} = 0° - 105°

$\circ$ — l^{II} = 270° - 360°

o — l^{II} = 110° - 160°

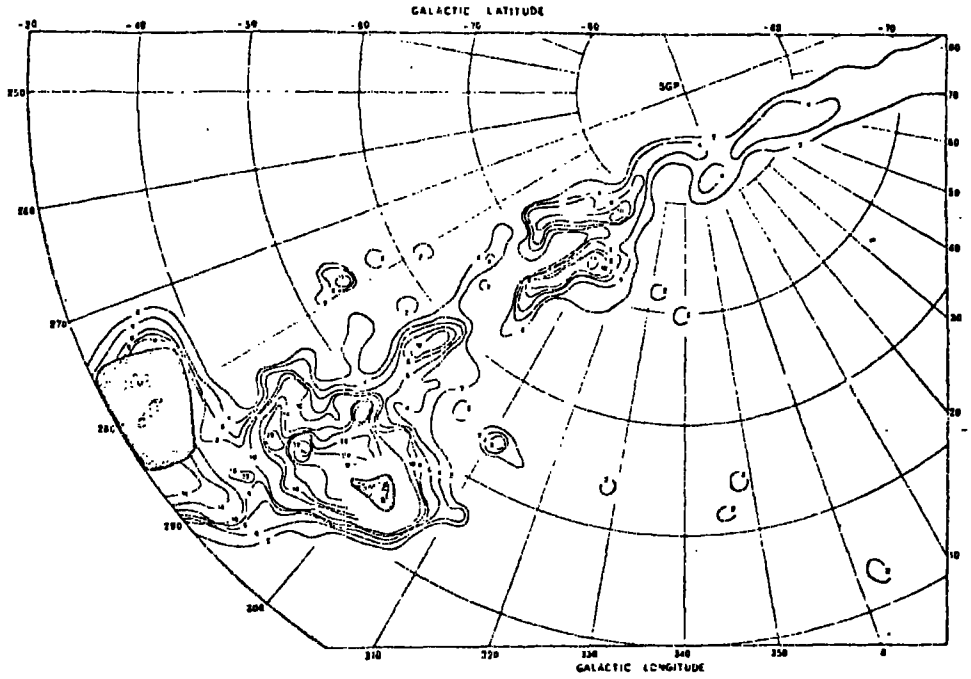

Fig. 3.3b

HI distribution between the Magellanic Clouds and the South Galactic Polar region, from Mathewson et al. (1974). All HI within the velocity range -340 km.S^{-1} to +380 km.S^{-1} is plotted, except the 'zero' - velocity HI (ie local spiral arm gas). The contours give the surface densities of the HI in the Magellanic Stream, from a survey at Parkes. The contour unit is 2 x 10^{19} atom cm^{-2} . The hatched areas represent the approximate extent of the Large and Small Magellanic Clouds.

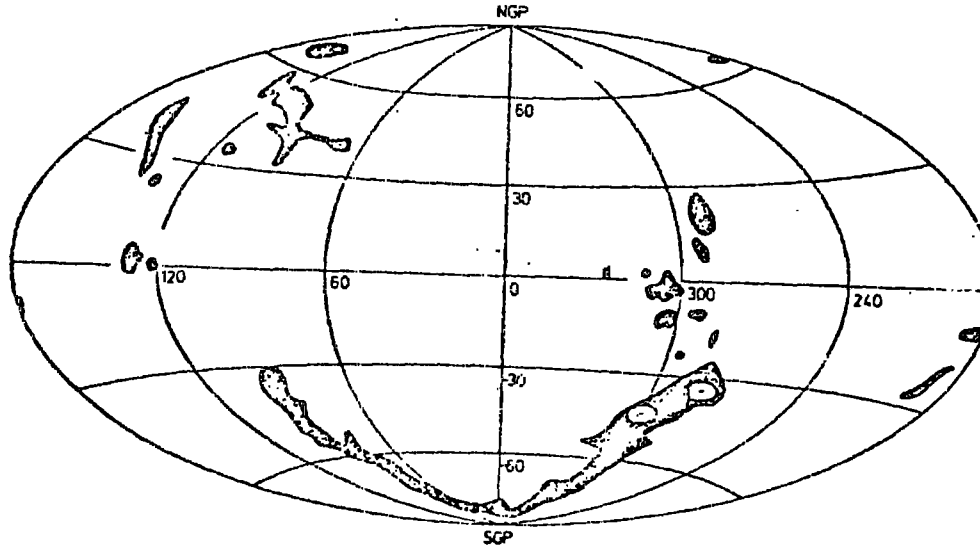

Fig. 3.3c

The Magellanic Stream drawn on an Aitoff projection in galactic coordinates by Mathewson et al. (1974). The shaded areas are the areas surveyed by Dieter (1965), Hulsbrosch and Raimond (1966), von Kuilenburg (1972), and Wannier and Wrixon (1972). The cross-hatched areas are high velocity HI clouds discovered much earlier by northern hemisphere observers (cf. Hulsbrosch, 1972).

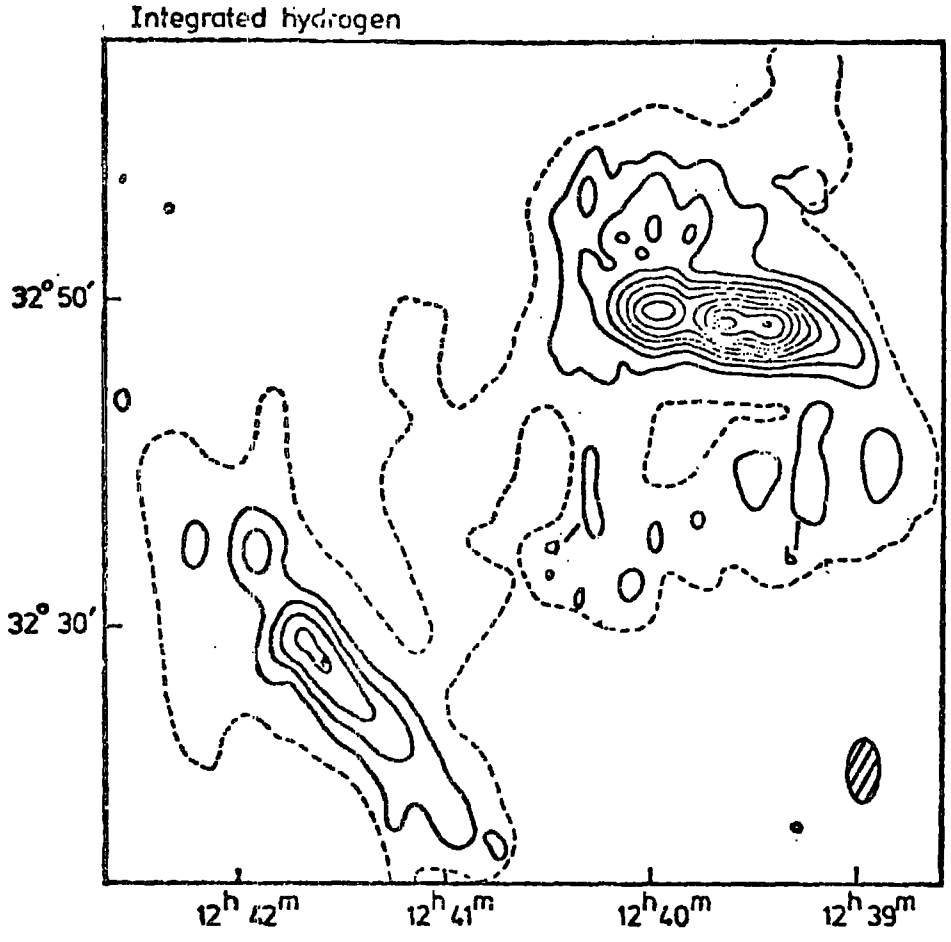

Fig. 3.4

Integrated hydrogen map of NGC 4631 and NGC 4656, by Winter (1975). The contour interval is 130 K km s^{-1} , and the lowest contour is at 130 K km s^{-1} . The dotted contour is at 15 K km s^{-1} . The mass of the feature a is estimated to be 10^8 $M_\odot$ and that of b 2.6×10^8 $M_\odot$.

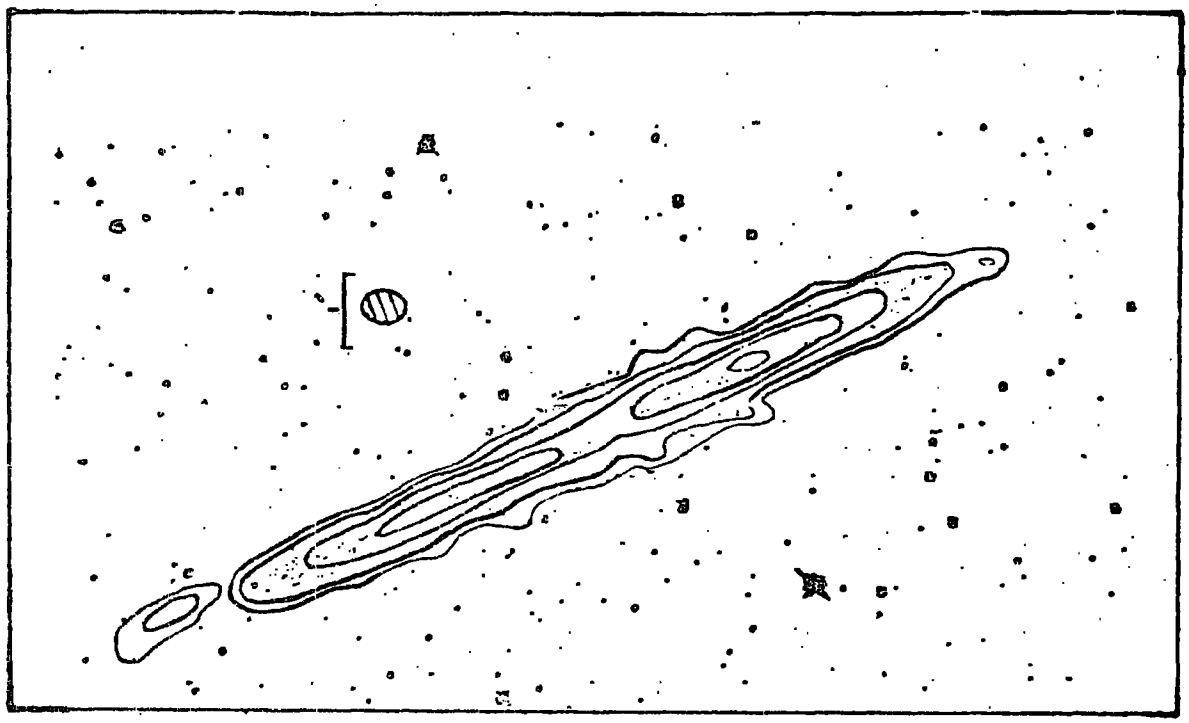

Fig. 3.5

Distribution of HI column density in NGC 891, by Sancisi et al (1974). The contours (0.2, 0.4, 1.2, 2.0, 2.8) are in units of 3×10^{21} cm^{-2}. These values are underestimates of the actual column densities, because of HI self-absorption and absorption against the radio-continuum emission from the disc of the galaxy itself. The map is based on incomplete data and therefore preliminary.

3.6 Rotation and Masses.

3.6.1 The Galaxy.

The rotation curve of the Galaxy has been obtained from 21-cm line observations of HI, together with the observations of the motions of the nearby stars which gives the Sun's orbital speed. The theoretical curve computed by Schmidt (1965) from a model of the mass distribution inside the Galaxy, and the rotation curve obtained by Shane and Smith (1965), are shown in fig. 3.6 . The accepted mass of the Galaxy is $2 \times 10^{11} M_{\odot}$, but could be as high as $4.3 \times 10^{11} M_{\odot}$ (Lynden - Bell, 1977b)

3.6.2 NGC 891.

The Westerbork 21 cm observations of NGC 891 have shown that there is a great degree of regularity in the large-scale motions in the galaxy. The observed HI line spectrum is similar to the longitude-velocity diagrams which have been constructed for our Galaxy from 21 cm line observations. The highest rotational velocity is 240 km/s, and the rotation curve is symmetrical to within $\pm$ 10 km/s in the southern and northern side, and stays high and approximately constant from 2′ to 5′ from the centre. The total mass is $3 \times 10^{11} M_{\odot}$ from the HI observations. Fig. 3.7shows the distribution of HI radial velocities along the major axis of NGC 891.

3.6.3 NGC 4631.

In 1969 Crillon and Monnet studied the ionized hydrogen in NGC 4631, and discovered and catalogued 88 HII regions. The rotation curve was obtained from radial velocity measurements. The centre of symmetry of the optical rotation curve is 1′ away from the rotation curve of HI, and the bar-like motions mentioned by de Vaucoleurs (1963a) were not found. In

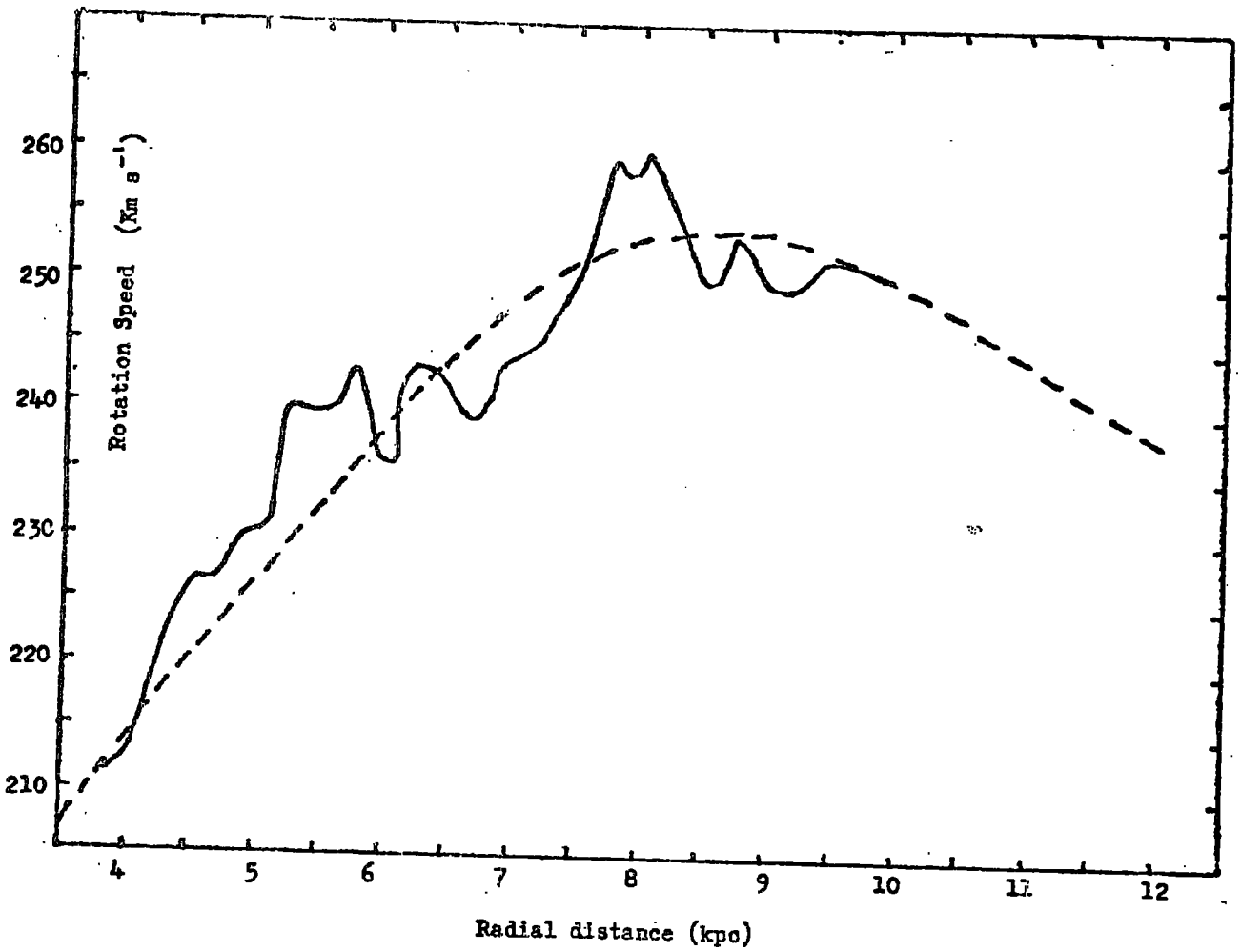

Fig 3.6

Rotation curve of the Galaxy by Shane and Smith (1965), from HI observations, together with the theoretical curve computed by Schmidt (1965).

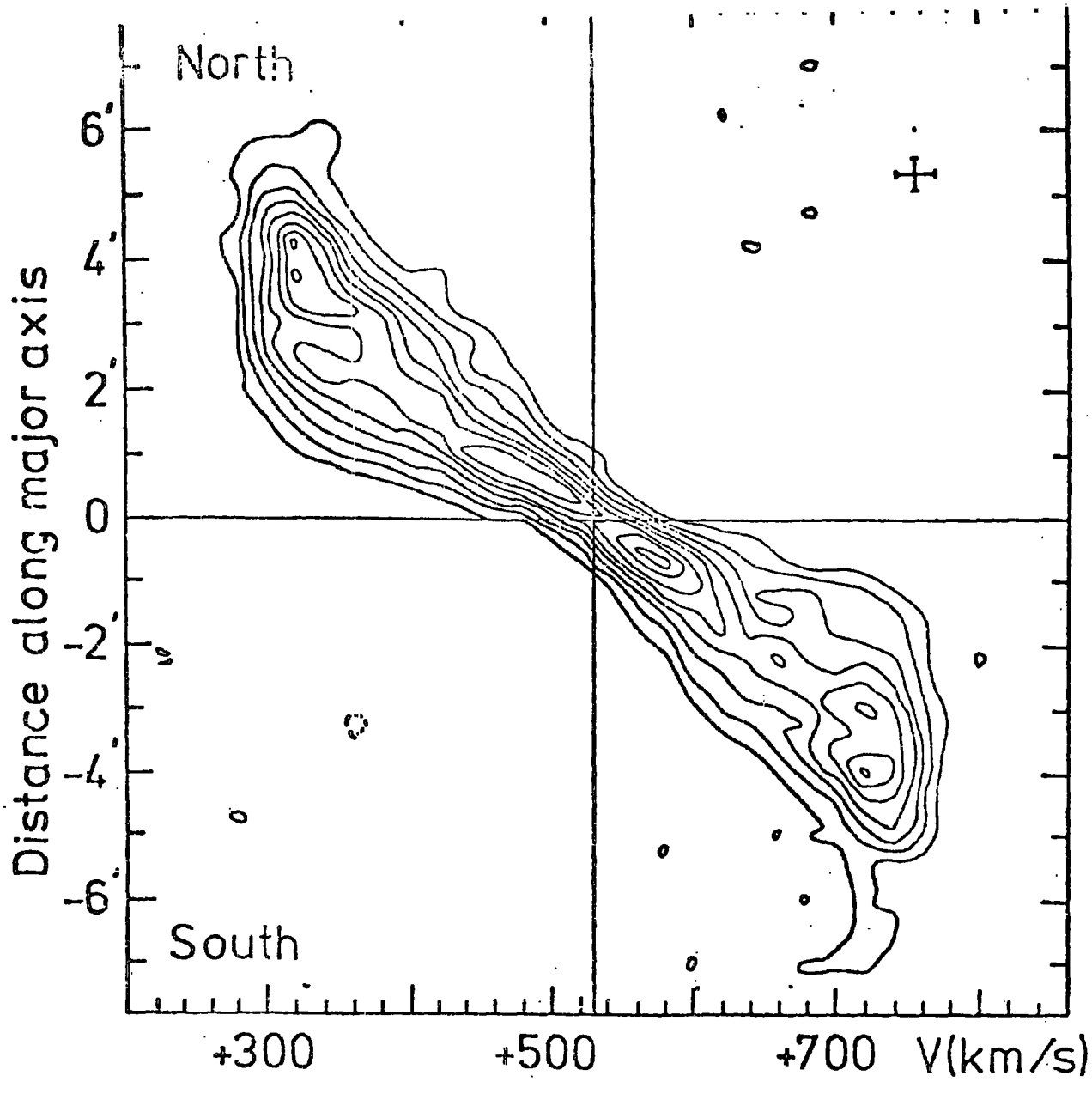

Fig. 3.7

Distribution of HI radial velocities along the major axis of NGC 891, by Sancisi et al. (1974). The radial velocities are heliocentric. The contours give the beam-averaged brightness temperature T_b . The lowest contour and the contour interval are 6° K. The cross in the upper-right corner shows the velocity and spatial resolutions.

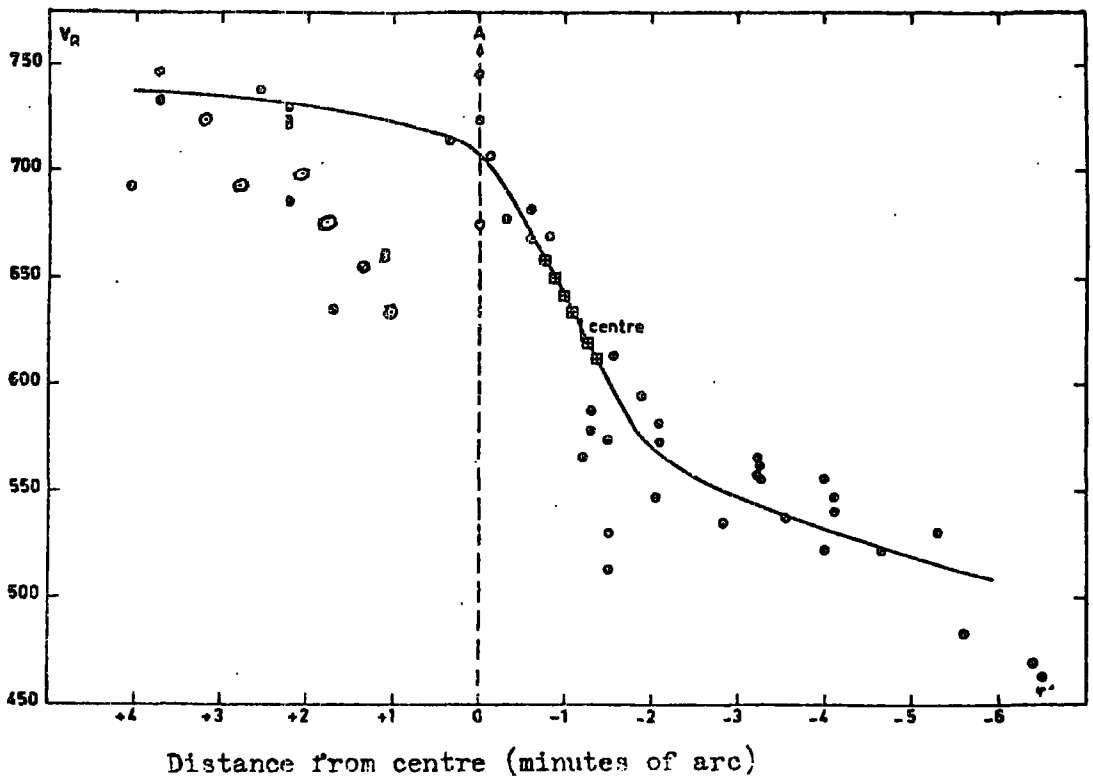

Fig. 3.8a

Rotation curve of NGC 4631 by Crillon and Monnet (1969).

- HII regions in the galactic plane.
- HII regions outside the plane.
- General emission near to the centre of rotation.

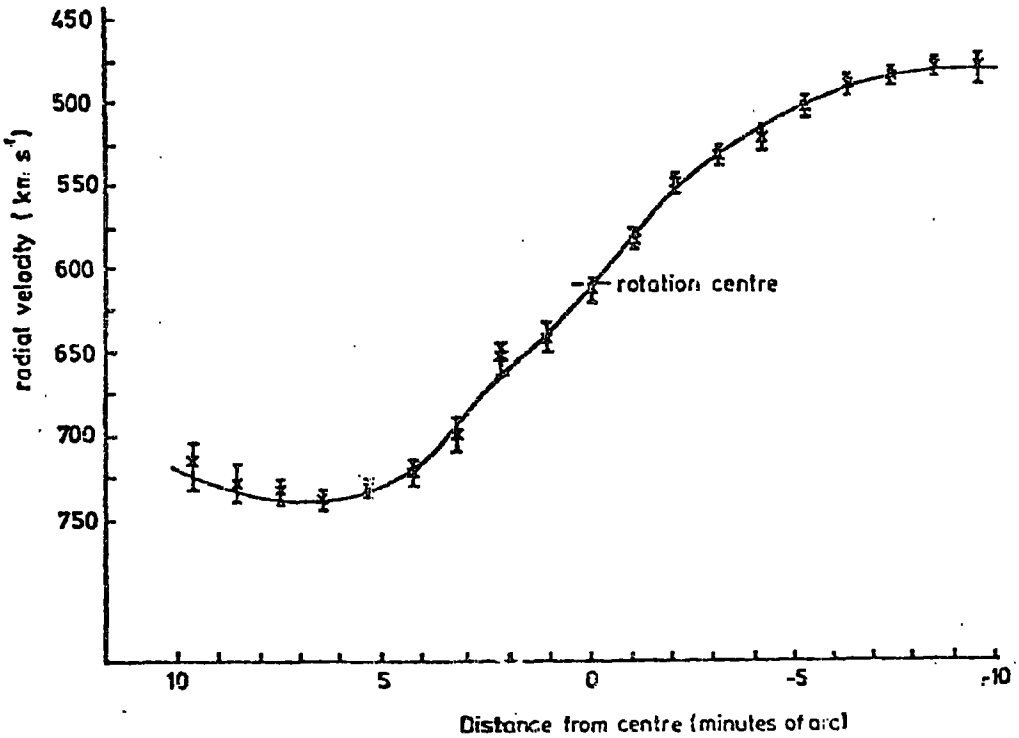

Fig. 3.8b

Rotation curve of NGC 4631 by Winter (1975), from HI observations. Radial velocities are geocentric.

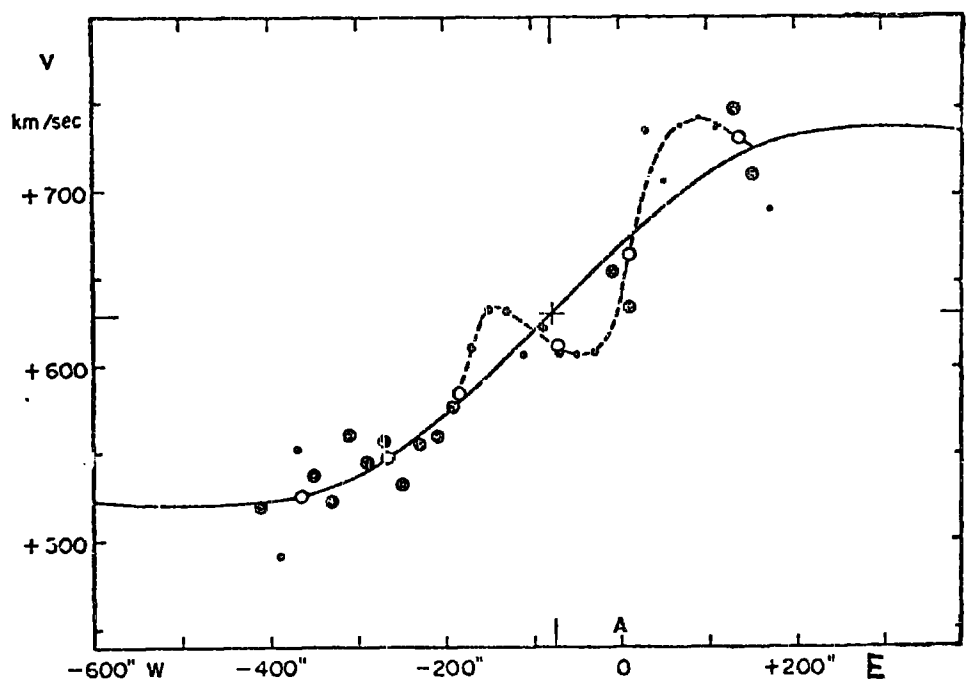

Fig. 3.13

Rotation curve of NGC 4631 by de Vaucoleurs and de Vaucoleurs (1963a), from Hα and six other emission line measurements. The probable error of the filled circles range from 10 to 18 km. s^{-1}, and that of the open circles 5 - 7 km. s^{-1}. The continuous curve is that computed for a model, while the dashed line is a freehand interpolation of the observed velocities. Cross marks centre of symmetry of regular rotation-curve. Projection of bar is alleged to be $\sim 40''$ west of A.

the south-east, outside the galactic plane, the radial velocities of HII regions are 50 km/sec smaller than that of the neighbouring regions in the galactic plane, suggesting that some ejection of matter has occured. The total mass of the galaxy is $\simeq 3.5 \times 10^{10} M_\odot$. A.J.B. Winter (1975) derived the rotation curve of NGC 4631 from his 21 - cm observations, and the total mass from his curve is $(1.95 \pm 0.2) \times 10^{10} M_\odot$, this mass lying within 10 kpc from the centre, and it is therefore a lower estimate of the mass. These two rotation curves are shown in fig. 3.8.

3.7 Continuum Radio Properties.

3.7.1 The Galaxy.

The continuum spectrum has been observed for wavelengths from a few millimeters to about 30 m (10^{11} - 10^{7} Hz), while most of the observational work has been carried out in the range 3 cm - 3 m. At high frequencies thermal emission starts to take over from the synchrotron process, as the main contributor to the radio emission, while at low frequencies synchrotron self-absorption becomes important. At low frequencies (10 - 100 Mhz), continuum radio emission is detected over the whole sky, and there are superposed 'sources', of small and extended angular diameters. The radio emission from discrete sources e.g. stars, pulsars, etc., has a negligible integrated effect on the background radiation. Supernova remnants also make a very small contribution to the total flux, but some are strong enough to be individually detectable in external galaxies.

The Landecker and Wielebinski (1970) whole sky map is the only complete map of the whole sky. It is a combination of several surveys at 85 and 150 Mhz , the observations having been mainly at Parkes and Cambridge with an angular resolution of about 2°. The map is shown in fig. 3.9. The diffuse component from the disc of the galaxy dominates the radio emission, the

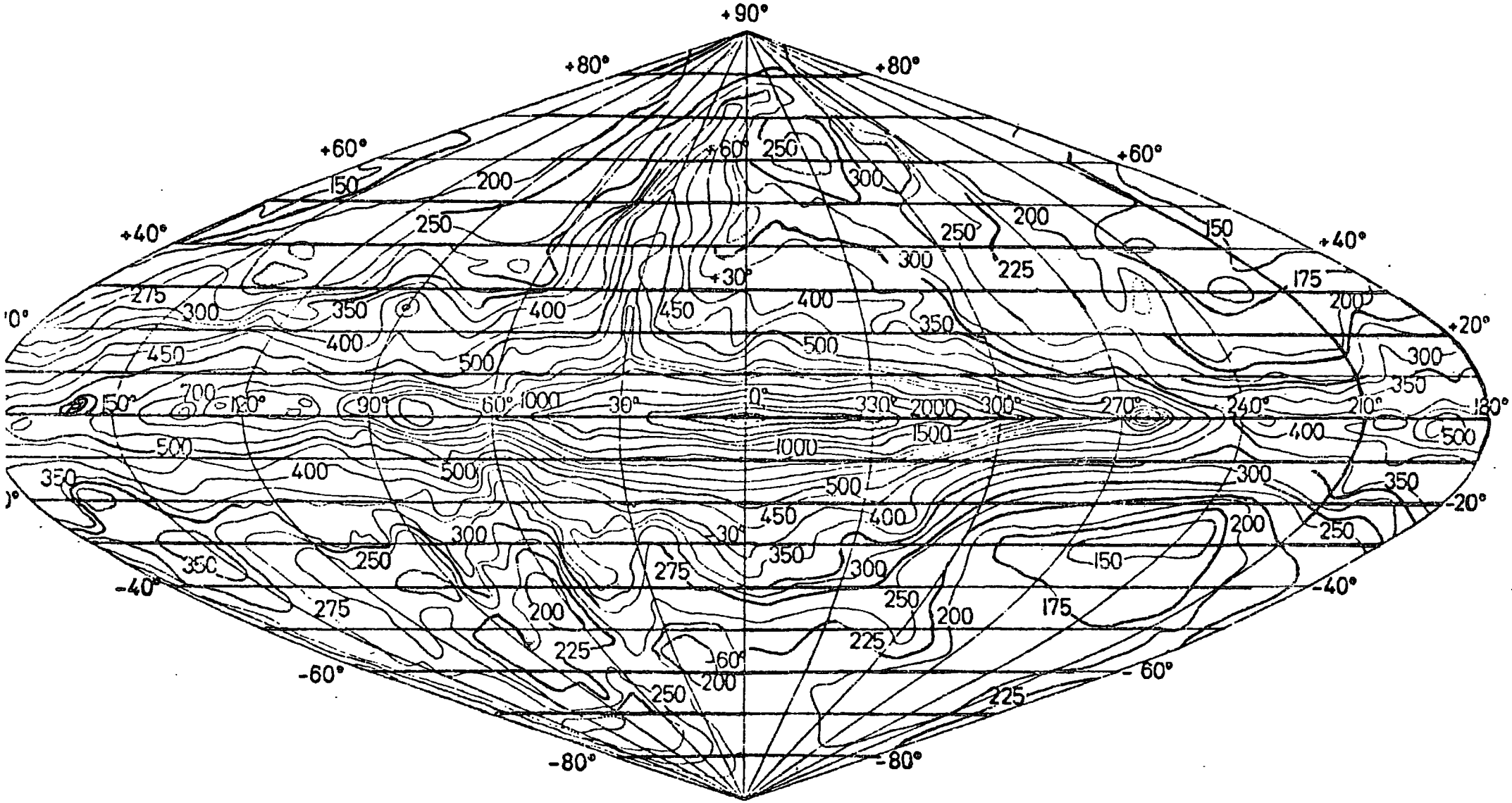

. 3.9

Landecker and Wielebinski (1970) 150 Mhz map of the Galaxy.

main emission extending over the longitude range 275° to 100°. 'Steps' are seen in directions tangential to spiral arms, and there are also a number of prominent 'spurs' starting off from the galactic plane in nearly perpendicular directions. The distribution of emission in galactic longitude, near the plane, is very irregular, but towards the galactic centre it is relatively smooth, the long path length smoothing out discrete variations. In the anti-centre direction the emission path length is much shorter, and thus local features stand out more. The radiation intensity spectral index in the disc is -0.4 ± 0.1 (Bridle, 1967) at $\sim$ 178 Mhz, steeping to -0.6 ± 0.1 at higher frequencies. From the Landecker and Wielebinski map Allen, Baldwin and Sancisi (1977), estimated that the semi-major axis extent of the radio emission of the galaxy is about 8 kpc. Baldwin (1976) derived an equivalent width of 1.5 kpc for the disc emission, at 408 Mhz. Various radio parameters of the Galaxy, along with the parameters for NGC 891 and NGC 4631 are listed in table 3.1.

3.7.2 NGC 891.

The continuum radio emission of NGC 891 has been mapped by the Westerbork radio telescope, at frequencies of 610 Mhz, 1412 Mhz and 5 Ghz (49.2 cm, 21.2 cm and 6 cm respectively). With the adopted distance of 14 Mpc, the emission is seen to extend to distances of $\sim$ 6 kpc above the plane. The overall radio emission consists of a highly flattened component coinciding with the equatorial plane, and a "thick disc" component with an axial ratio of about 3.5/1. The spectral index in the range 600 Mhz to 5 Ghz is -0.65, within 12 kpc of the centre along the major axis. In the Z direction the spectral index is about -0.65 from $Z = 0$ to $Z = 2.5$ kpc, and there is evidence that the spectrum steepens at higher Z. The equivalent width of the volume emissivity is approximately 1.8 kpc, and the semi-major axis extent of the radio emission 9 kpc,

Table 3.1

Some radio properties of the Galaxy, NGC 891 and NGC 4631. (Table based on that of Allen et al. (1977)).

Parameter	Galaxy	NGC 891	NGC 4631
Radio luminosity (10^{21} WHz^{-1} at 21 cm.)	1.4	1.8	4.2
Flux density of disc (J_y , at 21 cm.)	0.12	0.74	1.0
Equivalent thickness of radio disc in kpc, at 21 cm.	1.5	1.8	3
Exponential scale length r_o of radio emissivity, in r at Z = 0 (kpc), at 21 cm.	6	5	4
Face-on surface brightness at $r = r_o$, (K at 21 cm.)	0.3	3	1.6
Spectral index in the disc.	-0.6 ± 0.1 (Bridle 1967) -0.79 ± 0.02 (ν > 178 Mhz in anti-centre) (Brindle & Osborne 1976, unpublished)	-0.65	-0.6

approximately.

Seaquist and Bignell (1976) have mapped NGC 891 at 2695 Mhz and 8085 Mhz. The half-power beam widths at the two frequencies are 9" and 3", approximately. In both cases the radio emission is similar to the optical form of the galaxy, containing a mixture of thermal and non-thermal components. The disc appears to be resolved into a small disc component with a superimposed component of discrete sources, which are probably HII regions. These sources tend to clump together into concentrations and the clumpiness suggests the existence of a ring of emission 5 kpc from the galactic centre, and possibly another at 8 kpc. The first ring may correspond to the ring of emission in the Galaxy at 4 kpc (the so called 4 kpc arm). The 2695 Mhz map bears a strong resemblance to radio map of the plane region of our Galaxy. Fig.3.10a shows the distribution of face-on brightness at 2695 Mhz. There is seen to be a pronounced dip in the brightness distribution at 4 kpc. Similar effects are observed in M31, M51 and NGC 4631.

The radio absolute magnitude of NGC 891, according to that given by de Jong (1967), is -19.6, the absolute photographic magnitude being 10.85. Fig. 5 of de Jong (1967) shows that NGC 891 is somewhat more powerful than that expected from a normal spiral galaxy. Maps of the continuum emission are shown in fig. 3.10.

3.7.3 NGC 4631.

The Westerbork observations of NGC 4631 show that the brightest radio continuum feature is the centre region, with an extent of 3 kpc along the major axis. The variation of the spectral index across the face of the galaxy shows similarities to the variation in NGC 891. In the central nuclear region the spectrum is -0.5, changing to -0.6 near the equatorial plane, and steepening at large Z distances from the plane.

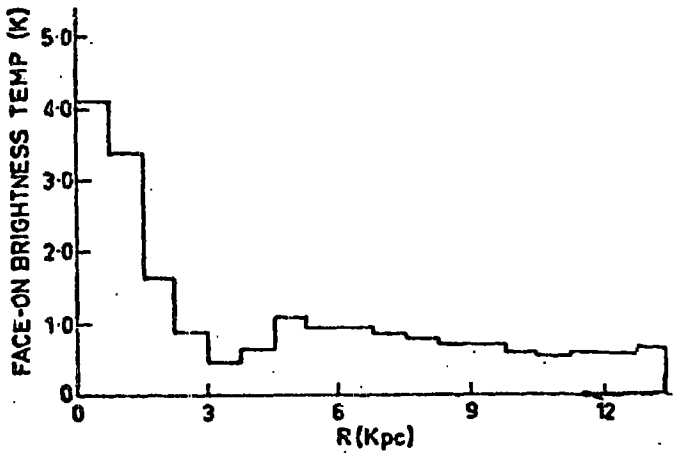

Fig. 3.10a

Distribution of face-on brightness temperature at 2695 Mhz of NGC 891 by Seaquist and Bignell (1976). The computations were made by averaging the profiles on opposite sides of the brightest point of the galactic nucleus. It was assumed that the emissivity is isotropic and distributed with circular symmetry.

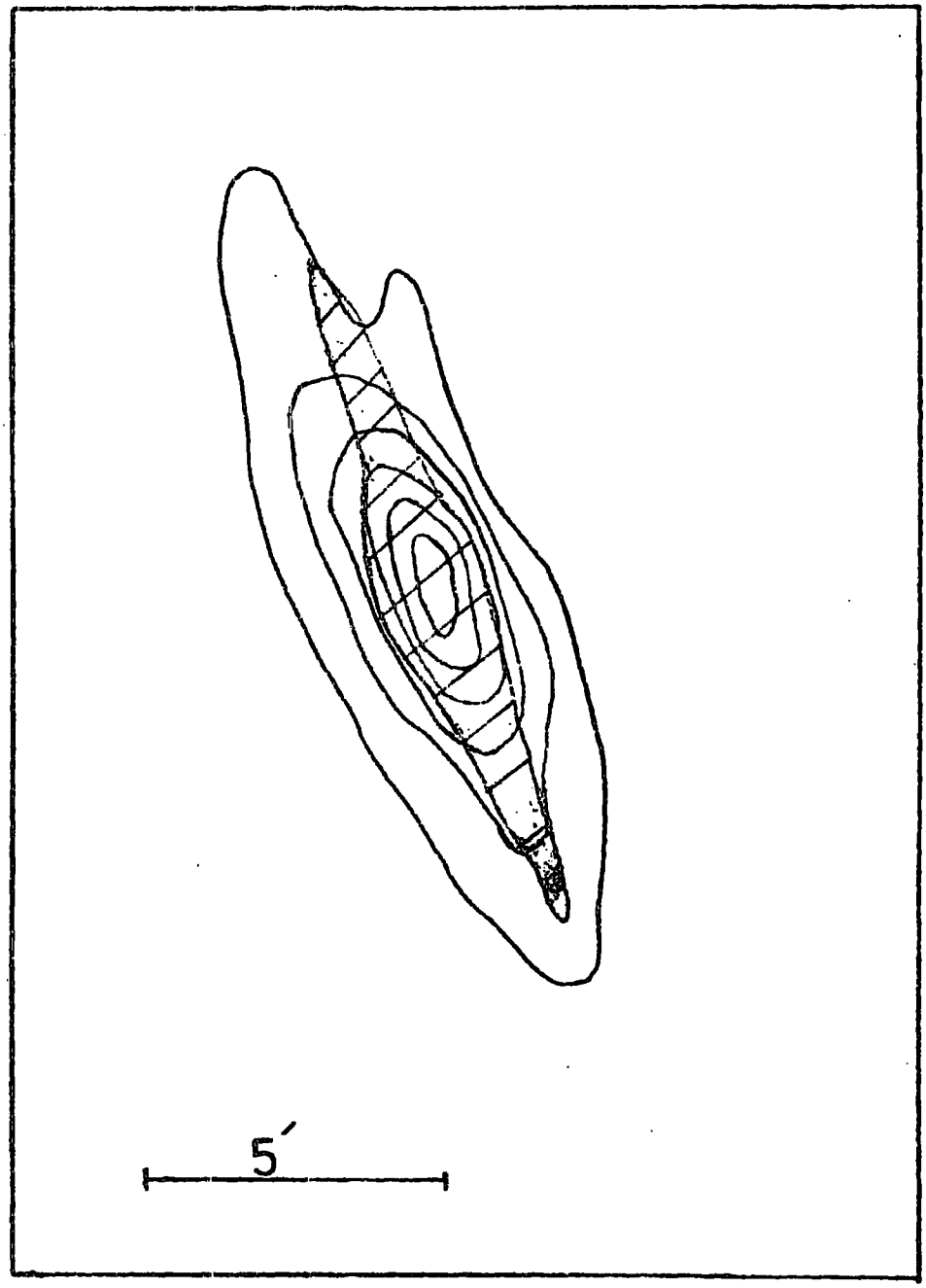

Fig. 3.10b

408 Mhz map of NGC 891, redrawn from Baldwin and Pooley (1973). The beamwidth is 80″ x 120″, and the contour interval 100K after the first contour level at 50K. The optical image is shown shaded in.

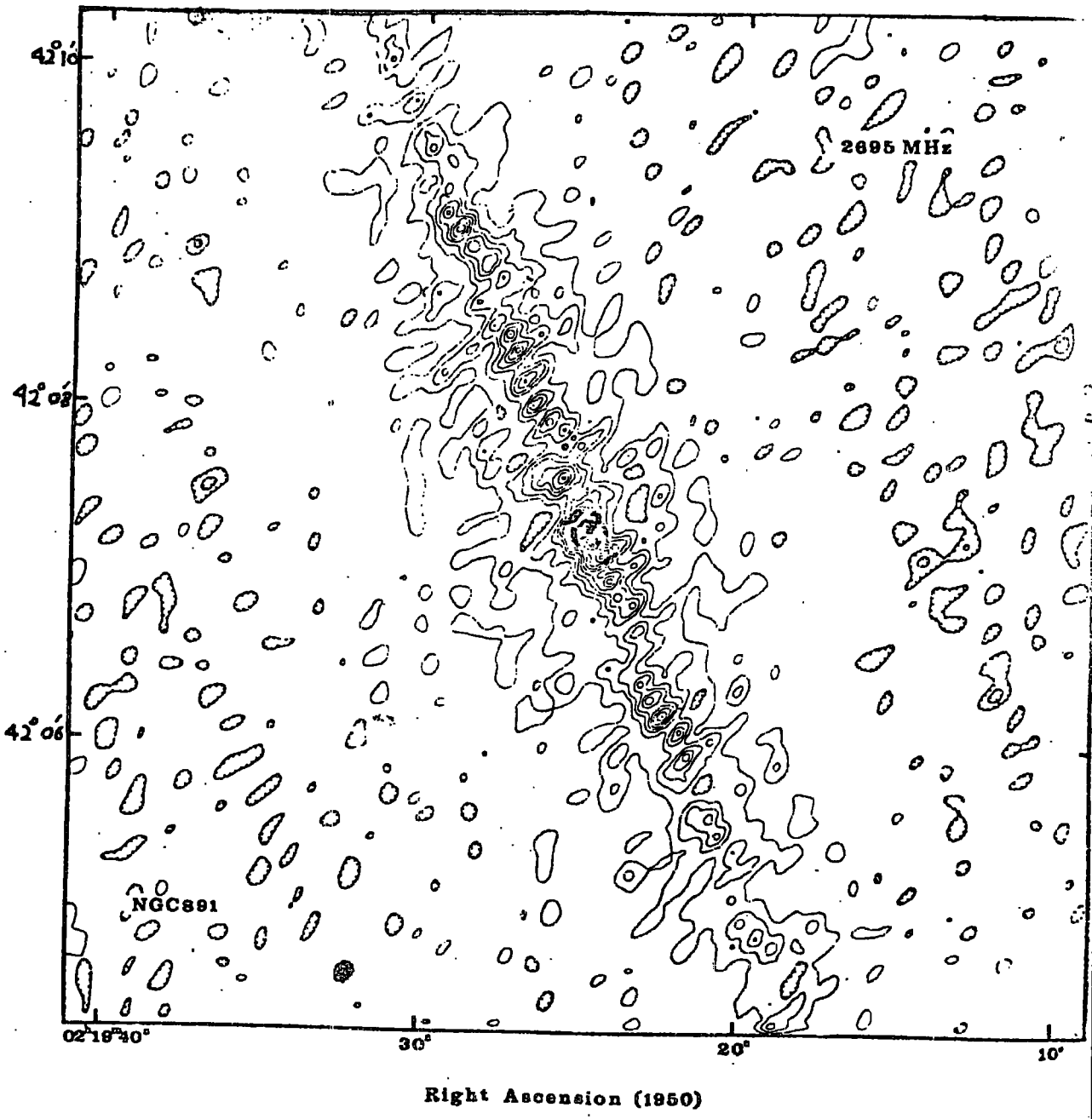

Fig. 3.10c

2695 Mhz map of NGC 891 by Seaquist and Bignell (1976). The zero contour has been omitted, and the contour interval is equivalent to the brightness temperature of 2.2°K.

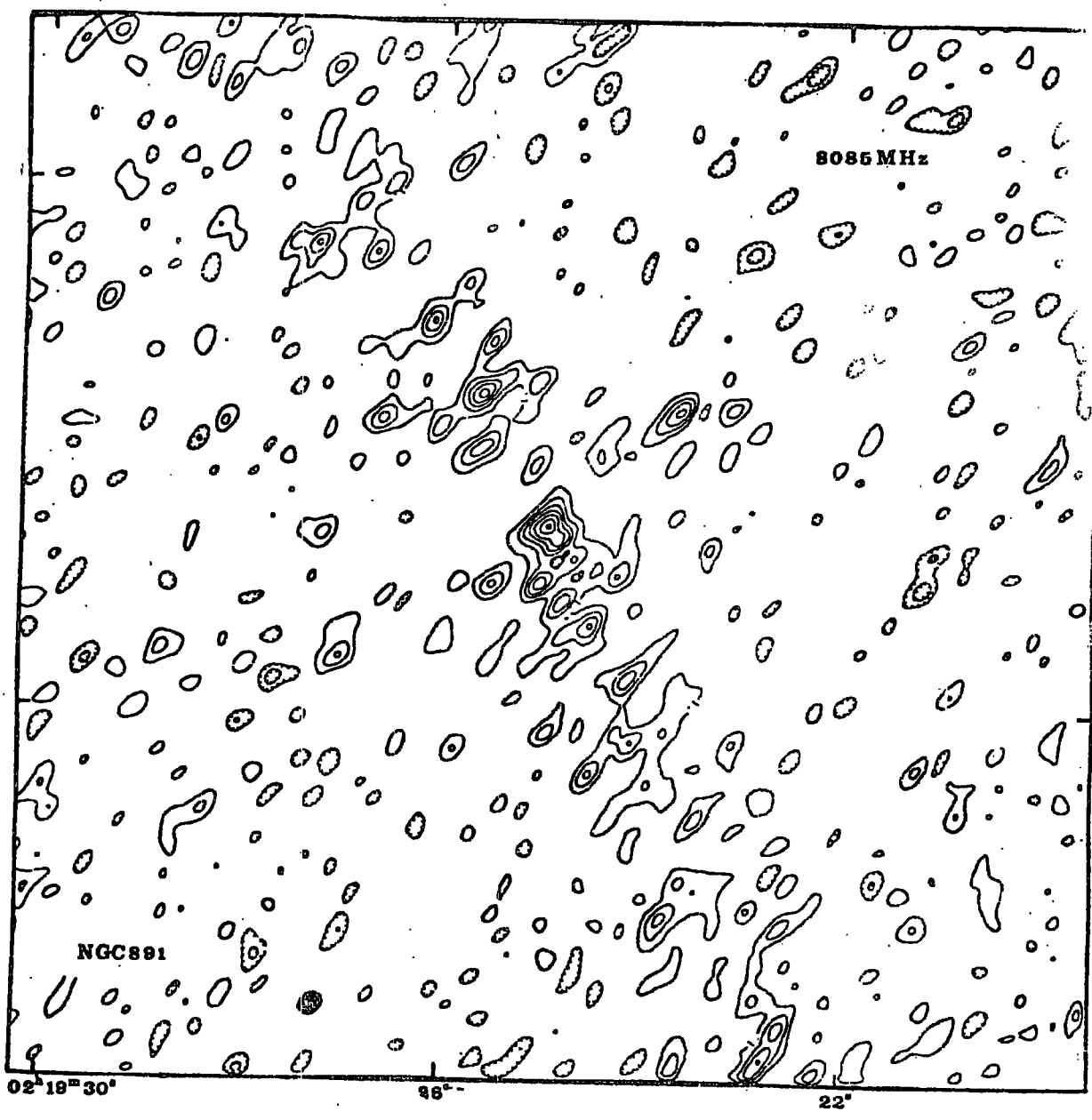

Fig. 3.10d

8085 Mhz map of NGC 891 by Seaquist and Bignell (1976). The zero contour has been omitted, and the contour interval is equivalent to an increment in brightness temperature of 1.3°K.

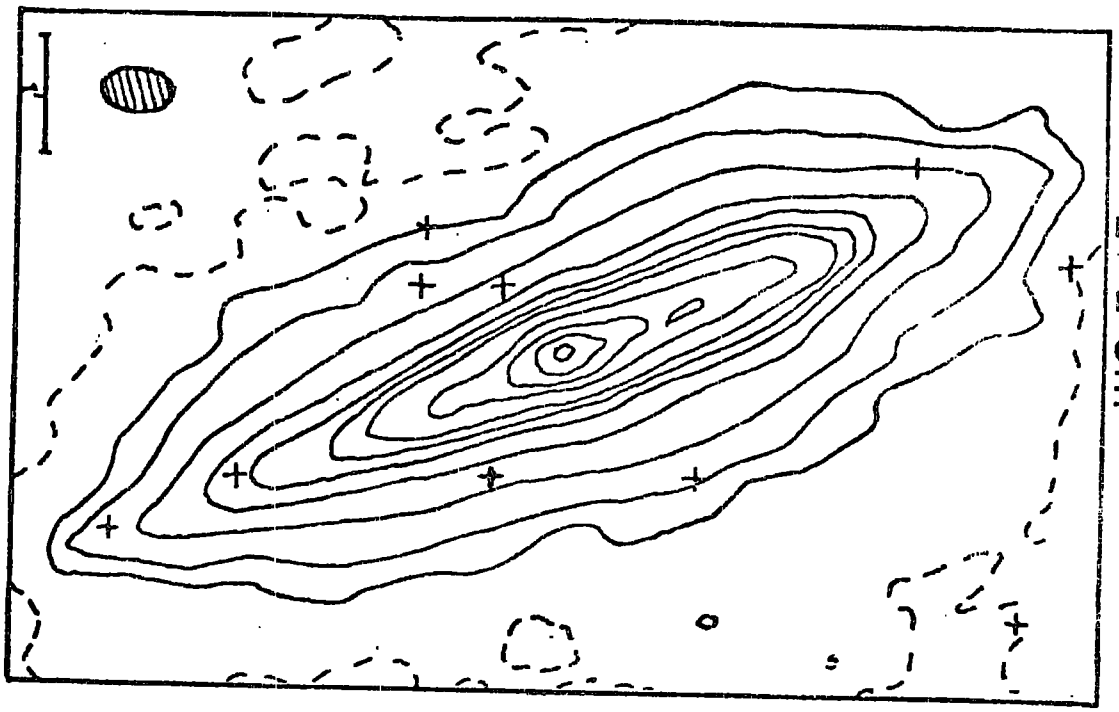

Fig. 3.10e

The 1412 Mhz map of NGC 891 by Allen et. al. (1977). The lowest contour values are 0 (thin dashed), 1 ($\simeq 4\sigma$), and 2 mJy/beam area, thereafter in steps of 4.55 from 4.55 to 22.75 mJy/ beam area, continuing in steps of 11.35 mJy/beam area.
(T_b (°K)/S (mJy)/beam area = 0.66)

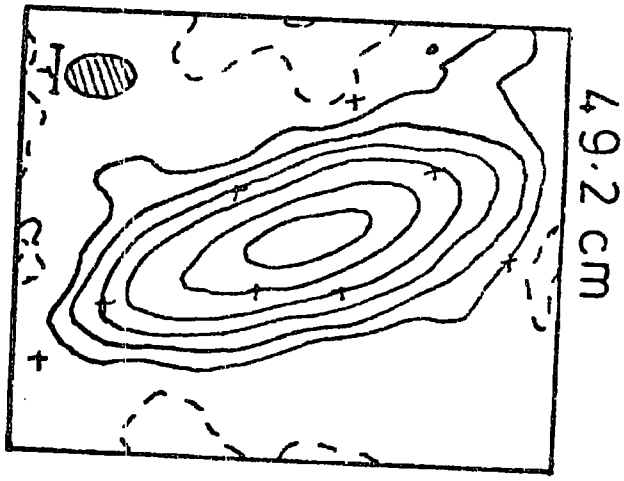

Fig. 3.10f

The 610 Mhz map of NGC 891 by Allen et. al. (1977). The contour values are 0 (thin dashed), 5 ($\simeq 3\sigma$), 10, 19.6, 39.2, 98.05, 196.1, and 294.15 mJy (beam area)$^{-1}$ (T_b (°K)/S (mJy/beam area) = 0.68).

The radio disc has about the same radial extent in kpc as that of NGC 891, but the emission decreases much less rapidly with increasing Z. Maps of the continuum emission are shown in fig. 3.11. Fig.3·11d and 3·11e show the cross-sections through the brightness distribution in NGC 4631 at 408 Mhz and at 1415 Mhz (van der Kruit 1973).

3.8 The Galactic Nuclei.

The nucleus of our Galaxy is the only one that has been studied in detail. Due to large obscuration by dust particles the galactic centre cannot be seen at optical wavelengths. Since the initial discovery of the radio source, known as Sagittarius A, near the centre, the central region has been extensively studied at radio wavelengths, and also more recently, infrared wavelengths. Complex molecules have been detected in the region, and also present are several X-ray sources.

The emission from the galactic centre consists of three main components : a non-thermal source, Sagittarius A (9 x 7 pc) very close to the centre, an extended source, about 180 x 70 pc, elongated along the galactic plane, which appears to be non-thermal, and a complex of giant HII regions in a similar area. Sgr A itself consists of two main features : Sgr. A East, which has a steep non-thermal spectrum and Sgr. A West, which is a centrally peaked source of linear size $\sim$ 3 pc with a flat spectrum which could be thermal.

Both NGC 891 and NGC 4631 have nuclei with much higher radio luminosities. Fig. 3.12 shows a plot of the monochromatic radio power of the nuclear source against the disc brightness, for various galaxies (Ekers, 1975).

The observations of Seaquist and Bignell (1976) show that the nuclear region (within a few hundred parsecs of the nucleus) of NGC 891 is composed of an unresolved source with a half-power width less than

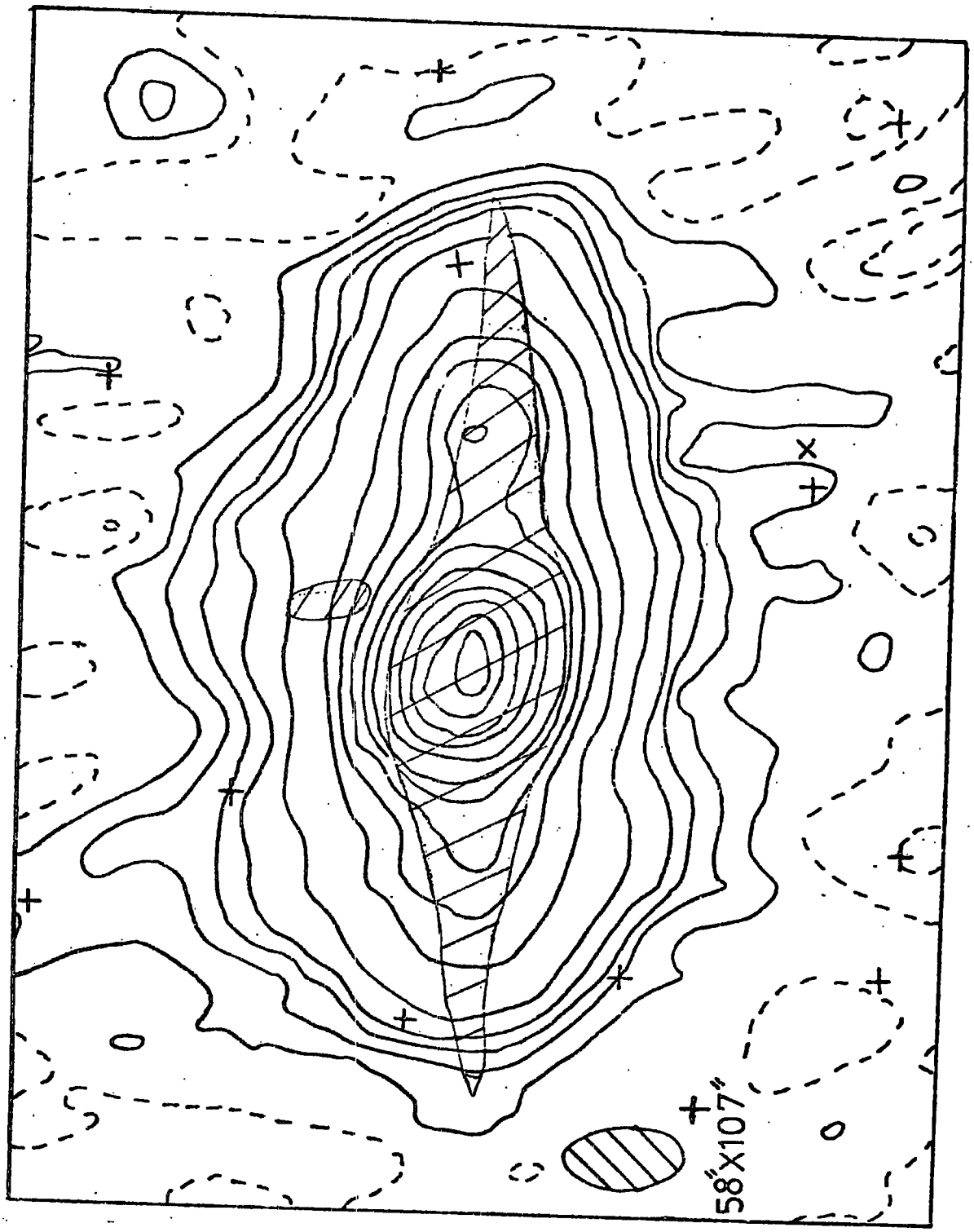

Fig. 3.11a

610 Mhz map of NGC 4631, redrawn from Ekers and Sancisi (1977). The half-power beam width is 58" x 107", and the contour interval 1.5 from 1.5 to 6, 10 from 10 to 60, and 20 from 20 to 160K. The dashed line represents the -1.5K and 0 K contour. The optical image is shown shaded in.

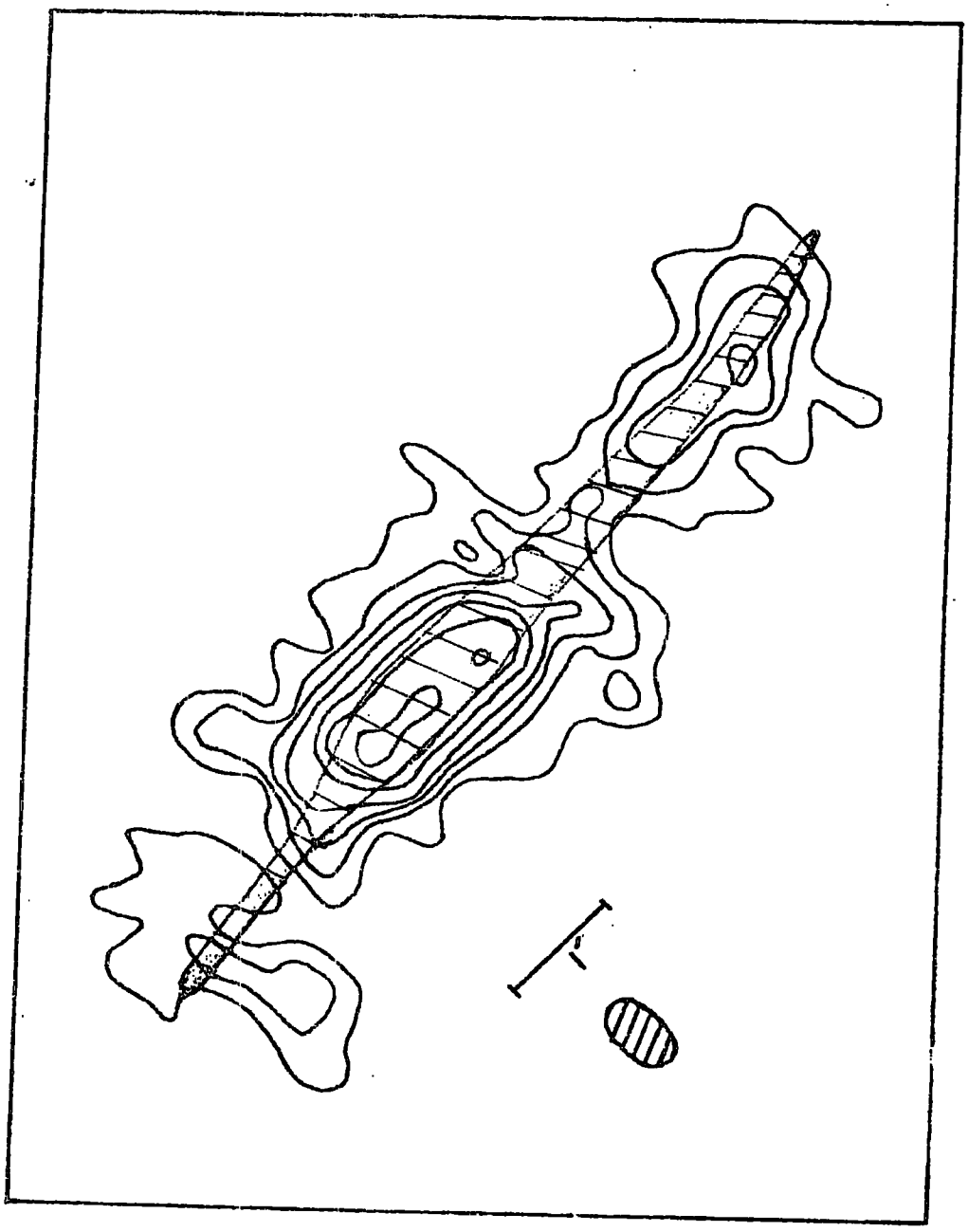

Fig. 3.11b

1407 Mhz of NGC 4631, redrawn from Pooley (1969b). The beam width is 23″ x 42″ , and the contour interval 3°K up to 12°K, and 6° thereafter. The optical photograph of G. and A. de Vaucoleurs (1963a) is shown shaded in.

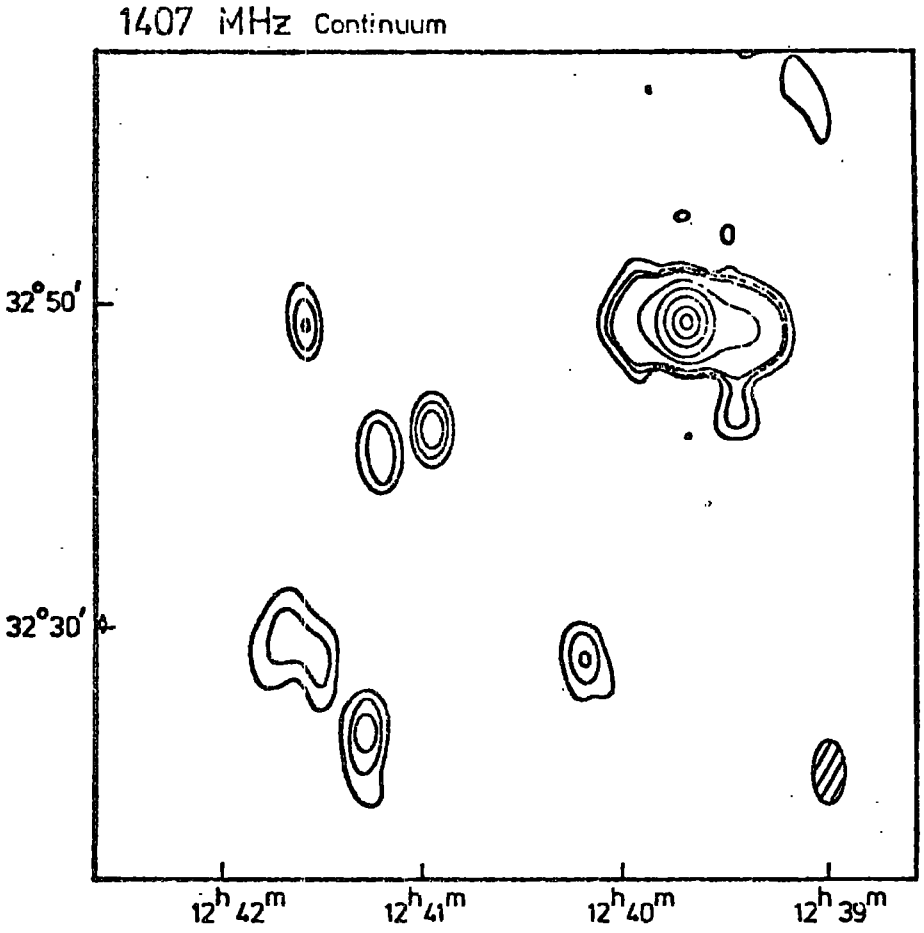

Fig. 3.11c

1407 Mhz radio survey of NGC 4631 and NGC 4656 by Winter (1975). The lowest contour is at zero and the contour interval 0.25K, for the first three contours, and 1K for higher ones.

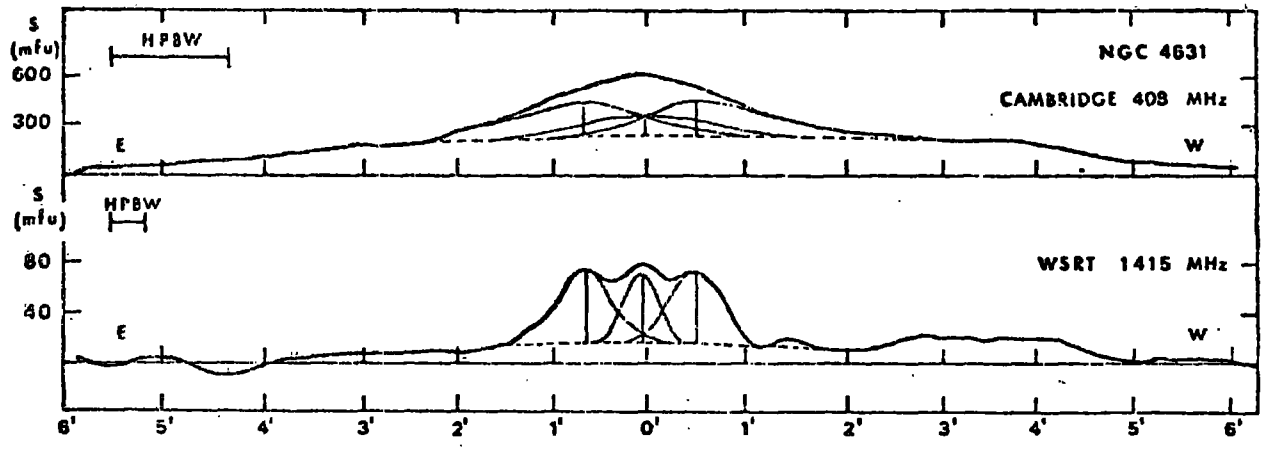

Fig. 3.11d

Variation of the brightness distribution along the major axis of NGC 4631 at 408 Mhz (Pooley 1969), and at 1415 Mhz (van der Kruit 1973).

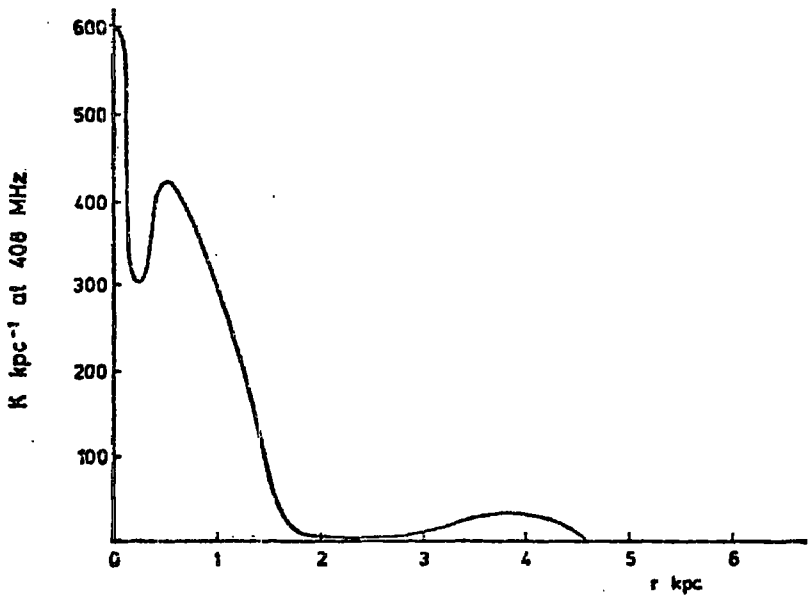

Fig. 3.11e

The variation of emissivity with distance from the nucleus of NGC 4631 (Baldwin and Pooley 1973).

5" (350 pc), superimposed on an extended region with h.p.w. of $\sim$ 20" (1400 pc). Both components are non-thermal and superimposed upon the underlying galactic disc radiation. The peak brightness at 8085 Mhz is about one beamwidth away from the corresponding peak brightness point on the 2695 Mhz map. The radiation to the immediate north of the nuclear source appears to be thermal, while immediately to the south of the nuclear source it is non-thermal. The 8085 Mhz map shows a small, probably unresolved source ($\sim$ 140 pc), superimposed on a complex background. At 2695 Mhz the luminosity of the unresolved component is 8×10^{18} W Hz^{-1} (D = 14 Mpc), compared to the luminosity of Sgr. A of 10^{17} W Hz^{-1} The source in NGC 891 appears to be a flattened region lying in the galactic plane, with a brightness temperature of $\sim 4^{\circ}$K above the level of the surrounding disc, when referred to half-power points ($\pm$ 700 pc). The mean brightness at a similar distance from Sgt. A is $\sim 5^{\circ}$K at 2650 Mhz from the map of Beard et. al. (1969). If the surrounding disc brightness is subtracted, the amount attributable to the extended nuclear source in our Galaxy, is probably less than 1°K.

The central source in NGC 4631 is resolved into a triple structure at high resolution.

3.9 Conclusions.

NGC 891 appears to be more similar to the Galaxy than NGC 4631, but is substantially larger, whereas NGC 4631 is smaller. At radio wavelengths NGC 891 has a luminosity about 18 times that of the Galaxy, while NGC 4631 is about 3 times more luminous. The HI distribution in NGC 891 appears to resemble more closely the distribution in the Galaxy, than does the distribution in NGC 4631, but there is no evidence for a broadening of the HI layer at large Radii. NGC 891 is different from the other two galaxies in having no close companions which could exert tidal forces, and

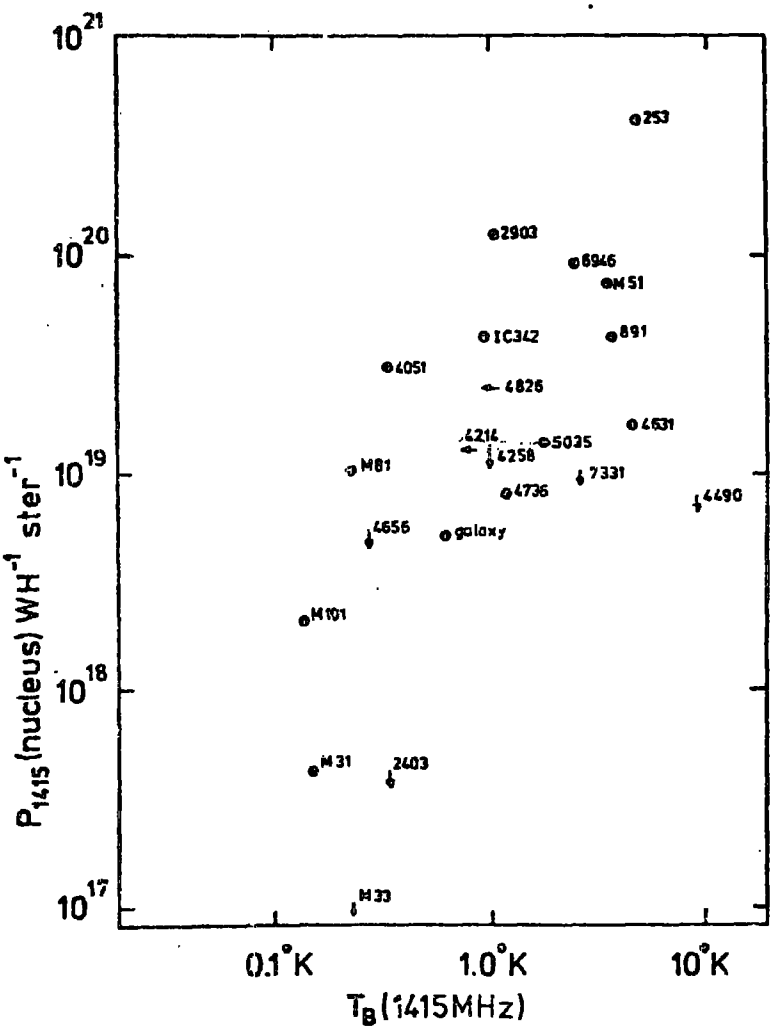

Fig. 3.12

Plot of the Monochromatic radio power of the nuclear source against the disc brightness in °K at 1415 Mhz for the spiral galaxies (Ekers, 1975).

is therefore in a completely undisturbed state.

Although NGC 4631 has some properties which associate it with being a "Magellanic barred-spiral", its radio properties are not consistent with this. The barred-spirals NGC 1300, 5383, 7640 and 7741, have been observed by the Westerbork telescope. In only two of the four galaxies was radiation detected from the nucleus, and for NGC 7640 and NGC 7741 no radiation at all was found (van der Kruit, 1973). Its radio properties are also dissimilar to those of the Large Magellanic Cloud, which has a nucleus with a similar emissivity, but disc component roughly one-third, that of the Galaxy (Mathewson, 1971).

Burbidge, Burbidge and Prendergast (1964) strongly criticised de Vaucoleurs and de Vaucoleurs classification (1963a). They point out that an elongated bar seen end-on cannot be distinguished from an axisymmetric nuclear bulge, and that their comparison galaxies have usually been classified as irregular by other observers. NGC 1637 is an example of an Sc galaxy with a markedly asymmetric light distribution (Sandage 1961), and it is clearly seen not to be a barred-spiral. They conclude that there is no evidence that NGC 4631 is a barred-spiral, and that even if they concede that it is, de Vaucoleurs and de Vaucoleurs model of the rotation is theoretically implausible, since it defies both conservation of energy and momentum.

The systematic residuals which de Vaucoleurs and de Vaucoleurs found in NGC 4631 (fig. 3.13) which they interpreted as departures from circular motions, are not apparent in Winter's rotation curve (fig. 3.8).

Van der Kruit (1973) concluded that no correlation had been found between morphological type and radio properties, except that the nuclei are fainter in Sc d spirals, and that there is no clear distinction between nuclei of normal and barred-spirals. However, Lequeux (1971) found that nuclear radio emission is more common among Sb's, while bright Sc's have a relatively stronger disc.

It would therefore be safer to attach more significance to a comparison of the radio-emission of the Galaxy with NGC 891, than with NGC 4631.

Chapter 3 - References.

Arp, H. C., 1966, Atlas of Peculiar Galaxies. (Pasadena : California Institute of Technology).

Allen, R. J., Baldwin, J. E. and Sancisi, R., 1977. Astron. and Astrophys. (in the press)

Baldwin, J. E., 1976, in The Structure and Content of the Galaxy and Galactic Gamma Rays, ed. F. W. Stecker (NASA Goddard Space Flight Center, Preprint) p. 206.

Baldwin, J. E. and Pooley G. G. 1973, 161, 127.

Beard, M., Thomas, B., Mac, A. and Day, G. A. 1969. Australian J. Phys. Astrophys. Suppl. no. 11 p. 27.

Bergh, S. van den. 1960. Astrophys. J., 131, and 558.

Burbidge, E. M., Burbidge, G. R. and Prendergast, K. H., 1964. Astrophys, J., 140, 1620.

Bridle, A. H., 1967. Mon. Not. R. Astr. Soc. 136, 219.

Crillon, R., Monnet, G. 1969. Astron. and Astrophys. 2, 1.

Danver, G. C., 1942. Ann. Obs. Lund. No. 10, 1.

De Jong, M. 1967. Astrophys. J. 150, 1.

Dieter, N. H. 1965. Astron. J. 70, 552.

Dufay, J. 1952, in trans. I. A. U. VIII (Rome 1952) p. 399.

Dufay, J. 1968. Galactic Nebulae and Interstellar Matter. ch. 38.

Ekers, R. D. 1975, in Structure and Evolution of Galaxies. (Nato Advanced Study Institute Series), p. 217.

Ekers, R. D. and Sancisi, R. 1977. Astron. and Astrophys. 54, 973.

Epstein, E. 1962. Ph.d thesis Harvard University.

Freeman, K. C. and de Vaucoleurs, G. 1972, in Vistas in Astronomy. vol. 14, p. 163.

Habing, H. J. 1966. Bull. Astron. Inst. Neth. 18, 323.

Hodge, P. W. 1975. Astrophys. J. 201, 556.

Holmberg, E. 1958. Medd. Lunds. Astr. Obs., Ser. 11,136.

Hubble, E. 1926. Astrophys. J. 64, p. 321.

Hulsbrosch, A. N. M. 1972, dissertation, Leiden University.

Hulsbrosch, A. N. M. and Raimond, E. 1966. Bull. Astron. Inst. Neth. 18, 413.

Hunter, C. and Toomre, A. 1969. Astrophys. J. 155, 747.

Jackson, P. D. and Kellman, S. A. 1974. Astrophys. J. 190, 53.

Kepner, M. 1970. Astron. and Astrophys. 5, 444.

Kerr, F. J. and Westerhout, G. 1965. Stars and Stellar Systems. 5, 167.

Kormendy, J. and Bahcall, J. N. 1974. Astron. J. 69, 671.

Kruit, P. C. van der, 1973. Astron. and Astrophys. 29, 249.

Kuilenberg, J. van 1972. Astron. and Astrophys. 16, 276.

Landecker, T. L. and Wielebinski, R. 1970. Aust. J. Phys. Astrophys. Suppl. 16.

Lequeux, J. 1971. Astron. and Astrophys. 15, 30.

Lynden-Bell, D. 1977(a). Nature, vol. 270, p. 396.

Lynden-Bell, D. and Lin, D. N. 1977(b). Mon. Not. R. Astr. Soc. 181, 37.

Mathewson, D. S. 1971, in The Magellanic Clouds. ed. A. B. Muller (Astrophysics and Space Science Library). p. 98.

Morgan, W. W. 1958, Pub. A. S. P., 70, 364.

Mathewson, D. S., Cleary, M. N. and Murray, J. D. 1974, in Galactic Radio Astronomy, (I. A. U. symposium no. 60) p. 617.

Noonan, T. W. 1977, Astron. and Astrophys. 55, 285.

Oort, J. H. 1966, Bull. Astron. Inst. Neth. 18, 421.

Oort, J. H. 1969, Nature. 224, 1158.

Oort, J. H. 1970, Astron. and Astrophys. 7, 381.

Osterbrock, D. and Sharples, S. 1952, Astrophys. J. 115, 140.

Pooley, G. G. 1969, Mon. Not. R. Astr. Soc. 144, 143.

Robinson, B. J. and van Damme, K. J. 1964, in The Galaxy and the Magellanic Clouds. (I. A. U. Symp. no. 20, Canberra, Australia) p. 276.

Robinson, B. J. and van Damme, K. J. 1966, Austr. Jl. Phys. 19, 111.

Roberts, M. S. 1968. Astrophys. J. 151, 117.

Sandage, A. 1961. Hubble Atlas of Galaxies. (Washington, D. C., Carnegie Institute of Washington).

Sandage, A. and Tammann, G. A. 1975. Astrophys. J. 196, 313.

Sandage, A. 1962. I. A. U. Symp. No. 15, Problems of Extragalactic Research, ed. G. C. McVittie (New York : Macmillan Co. p. 359.

Sandage, A. and Tammann, G. A. 1974. Astrophys. J. 194, 559.

Sancisi, R., Allen, R. J. and van Albada, T. S. 1974, in La Dynamique des Galaxies Spirales, ed. L. Weliachew (Colloques Internationaux du CNRS, No. 241) p. 295

Seaquist, E. R., Bignell, R. C. 1976. Astron. and Astrophys. 48, 421.

Sérsic, J. L. 1960. Zs. f. Ap., 50, 168.

Schmidt, M. 1965, in Galactic Structure. (Blaauur and Schmidt eds.)

Shane, W. W. and Bieger-Smith, G. P. 1965. Bull. Astr. Inst. Neth. 18, 263.

Smith, M. 1976, in I. A. U. Symp. 37 CNRS Coll. Paris, Sept. 1976.

Tammann, G. A. 1975. Optische Beobachtungs programme zur galaktischen struktur und Dynamik, Ed. Th. Schmidt-Kaler, Rochum, p. 1

Teerikorpi, P. 1976. Astron. and Astrophys. 50, 455.

de Vaucoleurs, G. 1976(b) in I. A. U. Symp. 37, & CNRS, Coll. Paris, Sept. 1976

de Vaucoleurs, G. 1977, in Occasional Reports of the Royal Observatory, Edinburgh. no. 2.

de Vaucoleurs, G. and de Vaucoleurs, A. 1963 (a), Astrophys. J. 137, 363.

de Vaucoleurs, G. and de Vaucoleurs, A. 1963 (b), Astron. Jl. 68, 278. (Abstract)

de Vaucoleurs, G. and de Vaucoleurs, A. 1964, Reference Catalogue of Bright Galaxies. (Austin : University of Austin Press).

de Vaucoleurs, G. 1976 (a), Stars and Stellar Systems. vol. IX 557. "Galaxies and the Universe", Ed. by Sandage, A. et. al.

Verschuur, G. L. 1973. Astron. and Astrophys. 22, 139.

Wannier, P. and Wrixon, G. T. 1972. Astrophys. J. Letters. 173, 119.

Weaver, H. F. and Williams, D. R. W. 1973. Astron. and Astrophys. Suppl. 8, 1.

Winter, A. J. R. 1975, Mon. Not. R. Astr. Soc. 172, 1.

Chapter 4

The Models of the Synchrotron Emission from NGC 891 and NGC 4631

4.1 Introduction.

This chapter will describe the models of the continuum radiation of 'edge-on', or near 'edge-on' galaxies, which have been constructed from the ingredients of the model of the galactic continuum radiation of Brindle et al. (1978).

In order to compare the continuum radiation from an edge-on aspect of the Galaxy with that from an external galaxy the resolution of the radio telescope has to be taken into account. Also when looking at external galaxies, the emission from the innermost region needs to be modelled, since the telescope beam effectively smooths the emission out over a large area (typically 2 kpc x 2 kpc).

The brightness temperature is given by the formula

$$T_b(\nu) \propto \int_0^S I(s)\, H_\perp(s)^{\frac{\gamma+1}{2}}\, ds \qquad (4.1)$$

(see Pacholczyk 1970)

where I(s) is the electron intensity at the point reached in the integration along the line of sight, $H_\perp(s)$ is the perpendicular component of the magnetic field there, and γ is the electron spectral index.

Therefore in order to calculate the emission from the galaxy, the above integral must be evaluated along lines of sight through the galaxy. the predicted values must then be convolved with the appropriate telescope beams, before they can be compared with the actual observations. The details of how this was done will be discussed later on. Only two 'edge-on' galaxies have been studied with sufficient resolution and sensitivity to make it worthwhile for a comparison to be made, namely

NGC 891 and NGC 4631. The results of the calculations will be presented in the next chapter.

4.2 Model of an 'edge-on' galaxy.

The model consisted of four circular arms of radii 4, 7, 11 and 14.5 kpc. Circular arms were chosen so as to facilitate the computations, and the radii chosen so as to give a good approximation to the arms used in the model of the Galaxy. Fig. 4.1 shows the four arms superimposed on the spiral structure, and Fig. 4.2 shows the geometry of the model. Since the model is symmetrical about the major and minor axes, the emission from the top right hand quadrant of the model was calculated, and then the emission from the whole model obtained from symmetry. The integration was performed from the boundary to the axis through the centre, the emission then being doubled.

The emission was calculated at 0.25 kpc intervals along the major and minor axes, starting at 0.125 kpc from the centre and finishing at a radial distance of 19.875 kpc.

In a region of no compression, i.e. at or above 0.5 kpc from the plane and at radial distances less than that of the first arm (4 kpc), the integral evaluated is

$$\int_{S_1}^{S_2} \left[\left(H(R) \sin\theta \right)^{1.8} + 0.6861 \left(\frac{H(R)}{F} \right)^{1.8} \right] \varepsilon(z,R)\, ds. \qquad (4.2)$$

where θ, the angle between the line of sight and magnetic field, is given by $\tan^{-1}(S/Y)$, and R by $(S^2 + Y^2)^{\frac{1}{2}}$. F is the ratio of the regular to irregular magnetic field strength, and is 0.75.

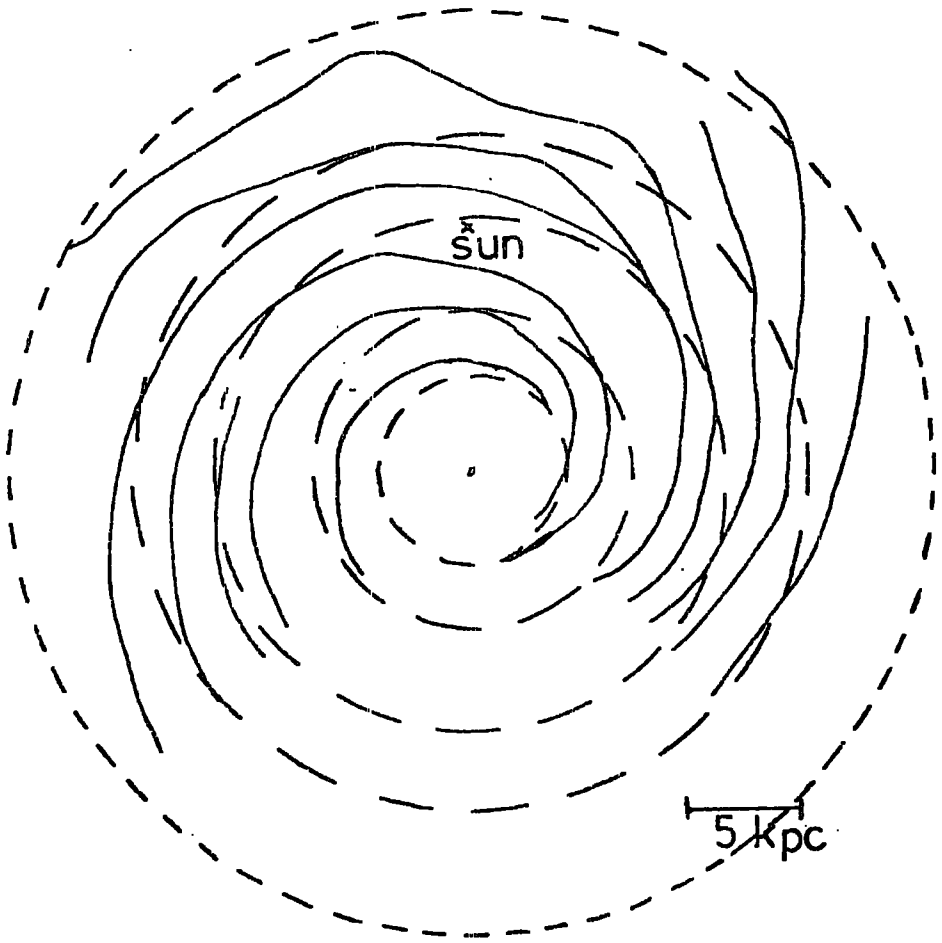

Fig. 4.1

Circular arms of radii, 4, 7, 11 and 14.5 kpc, and 20 kpc radial boundary, superimposed on spiral structure of Georgelin (1976).

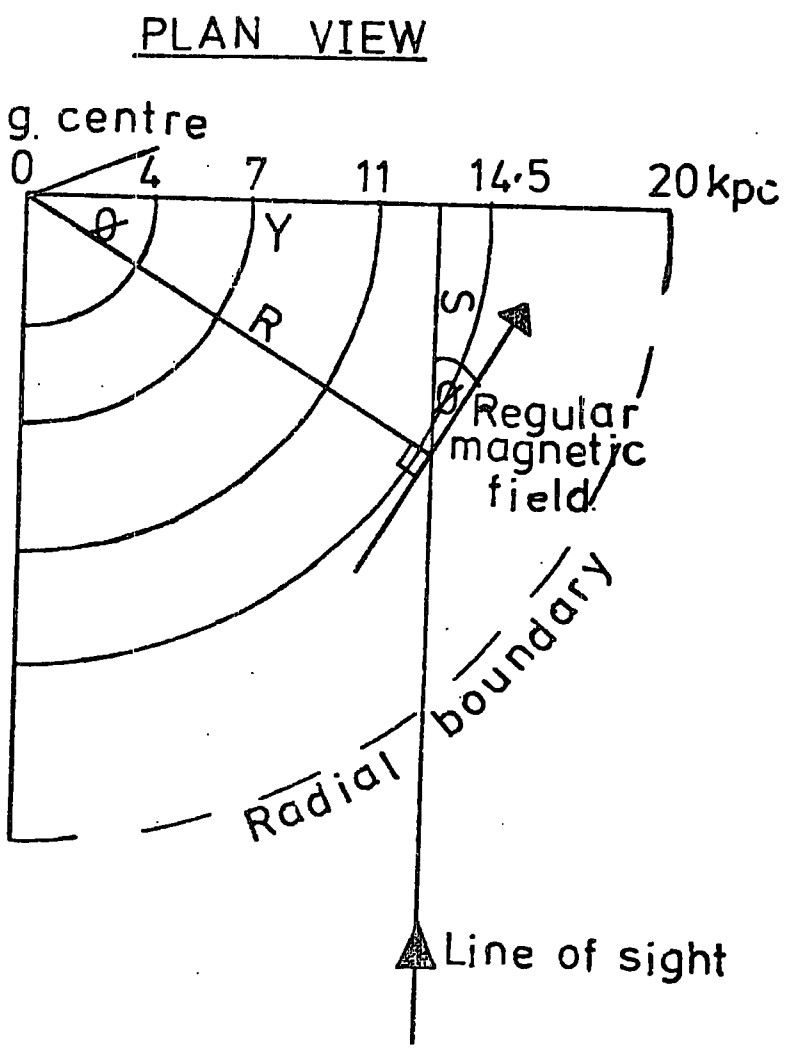

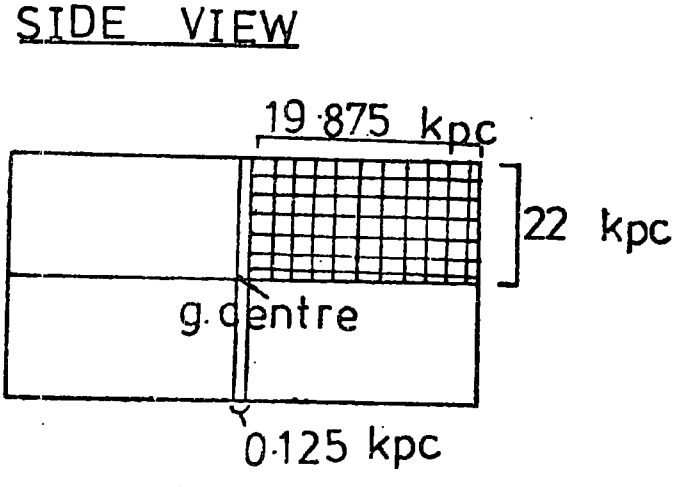

Fig. 4.2

Geometry of the model of the synchrotron radio emission from an edge on galaxy.

In compression regions the integral evaluated is

$$\int_{S_1}^{S_2}\left[\left(H(R)\sin\theta\,\frac{s-s_1}{s_1}\right)^{1\cdot8}+H_{\text{eq}}^{1\cdot8}\left(\frac{s-s_1}{s_1},\theta,F\right)\right]\varepsilon(z,R)\,ds$$

where $\varepsilon(Z, R)$, $H(R)$ and $H_{eq}\left(\frac{s-s_1}{s_1}, \theta, F\right)$ are given by equations 2.2 , 2.1 and 2.16 respectively. (4.3)

The integration was performed in stages along the line of sight, starting at the major axis, out to the first arm, then from the first arm to the second arm, and so on until a 20 kpc boundary was reached, where the emission was assumed to be zero. The integration step length was about 0.01 kpc, giving an accuracy of about one per cent.

4.3 Model of Continuum radiation from galaxy with inclination $0<i\leq 90^{\circ}$.

This model is based upon the previous model, all the various parameters being the same. The geometry of the model is shown in Fig. 4.3.

The radial distance from the centre is given by $R=(s^2\sin^2 i+y^2)^{\frac{1}{2}}$ (4.4)

and the vertical distance from the plane by

$$z=\left|\left(20\cos i+22\sin i-T\right)/\sin i-s\cos i\right|, \quad (4.5)$$

where T is the distance shown in the diagram . θ is given by

$$\theta=\cos^{-1}\left(\cos\left(\tan^{-1}\left(\frac{s}{y}\right)\times\sin i\right)\right) \quad (4.6)$$

The computer program integrated the emission along lines of sight, separated by 0.25 kpc intervals in the vertical and horizontal directions, within the rectangle ABCD (Fig. 4.3). It was arranged that lines of sight would pass through points perpendicular to E , the centre point, and the emission could be calculated out to any distance from the plane simply by changing the value B. Having reached the point D, the emission coming from the remaining part of the galaxy was obtained from symmetry. The step length was again about 0.01 kpc, though the accuracy achieved varied between one and ten per cent.

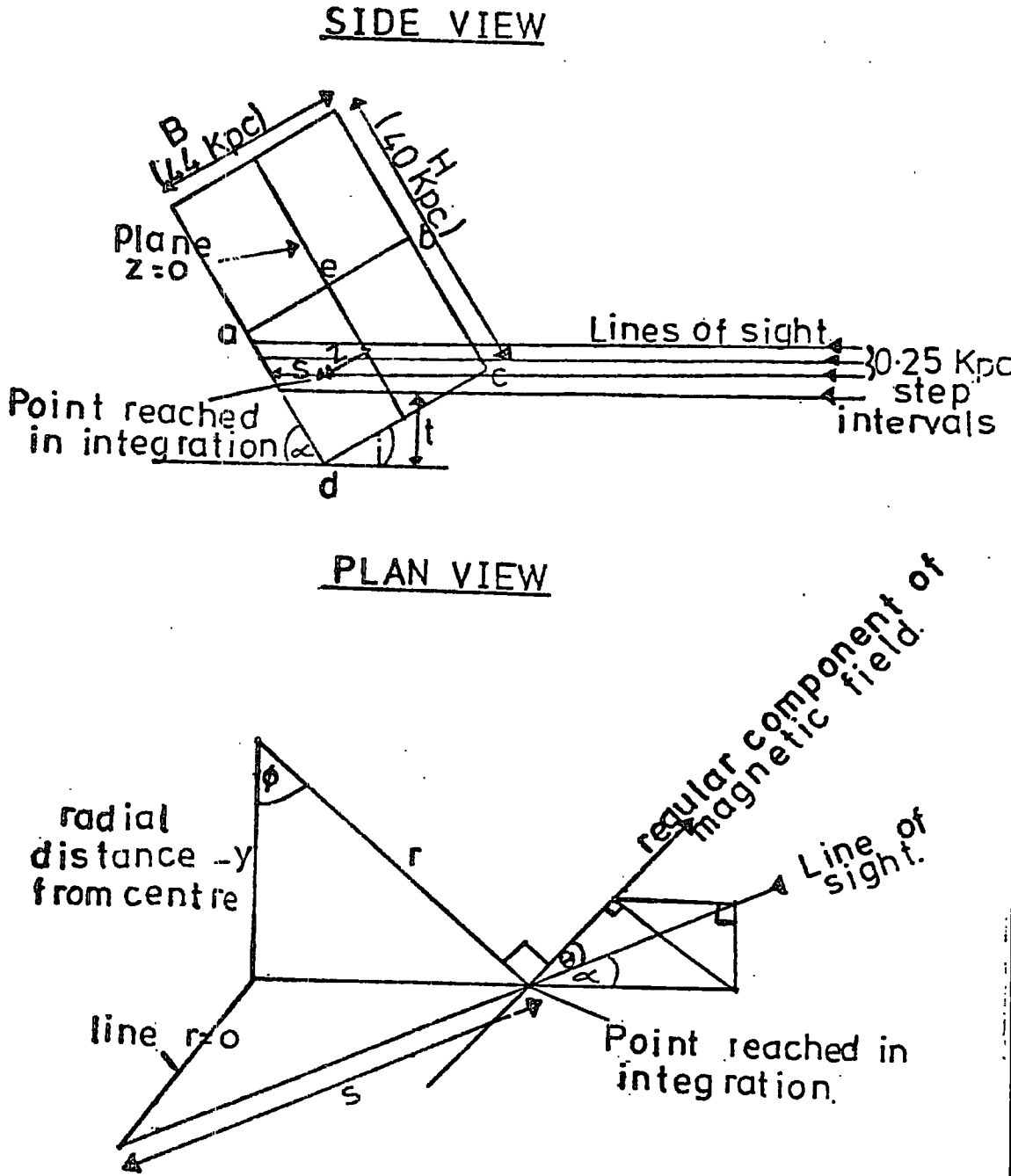

Fig. 4.3

Geometry of the model of the synchrotron radio emission from a near edge-on galaxy.

4.4 Convolution program.

Having calculated the emission at the grid points the predictions were then convolved with the appropriate beam sizes. The beam shapes are all elliptical, and the response of the telescope approximately gaussian.

The temperature of a source measured by an antenna is given by,

$$T_a(\theta) = \int_{-\infty}^{+\infty} A(\theta - B)\, T(B)\, dB \qquad (4.7)$$

where A is normalized so that

$$\int_{-\infty}^{+\infty} A(\theta)\, d\theta = 1 \qquad (4.8)$$

(see Kraus, 1966)

$T_a(\theta)$ is the measured antenna temperature at a position θ, $A(\theta - B)$ is the response of the antenna in a direction B measured from θ, and T(B) is the true temperature in the direction B.

The co-ordinate system used in the beam convolution is shown in Fig. 4.4. Since the response is approximately gaussian $A(\theta - B)$ becomes

$$\exp - \left(\frac{x_i^2 + y_i^2}{2(\sigma_x^2 \cos^2\theta_i + \sigma_y^2 \sin^2\theta_i)} \right) \qquad (4.9)$$

where σ_x is the half-power beam width in Right Ascension, σ_y that in Declination, and x_i, y_i, θ_i as shown in fig. 4.4.

Fig. 4.5 shows the set up in the convolution program. All points within the rectangle ABCD were convolved. The half-power beam widths of the telescope, expressed in seconds of arc, were first transformed into a linear distance (kpc), using the assumed distance of the object. Each point was convolved using all the points within three standard deviations of the beam centre. The following relation for an ellipse was used so as to include all the points,

$$R = \left[\frac{(\sigma_x \times n)^2 + (\sigma_y \times n)^2}{\cos^2\theta_i \times (\sigma_x \times n)^2 + \sin^2\theta_i \times (\sigma_y \times n)^2} \right]^{\frac{1}{2}} \qquad (4.10)$$

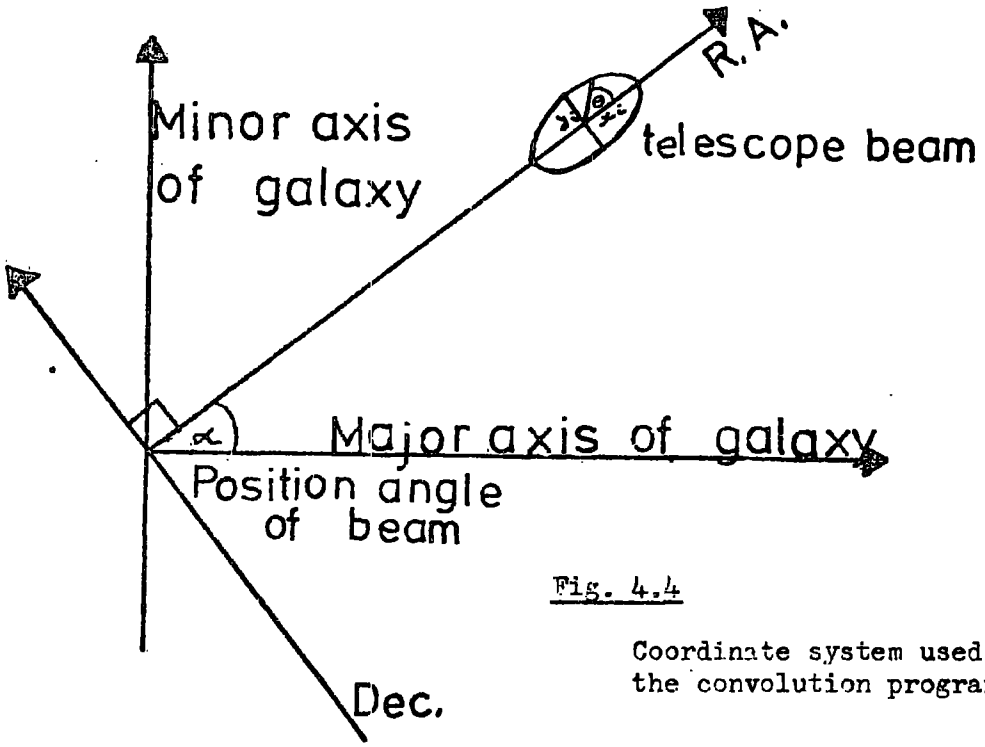

Fig. 4.4

Coordinate system used in the convolution program.

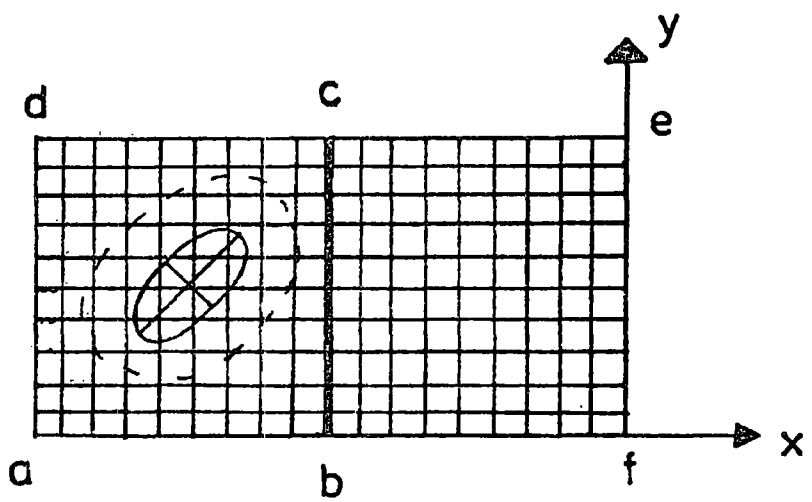

Fig. 4.5

Set up in the convolution program.

where n is the number of standard deviations convolving to. Whenever the beam fell outside the grid area the emission there was taken to be zero.

The integral was approximated by a summation over all points within 3 standard deviations of the centre of the beam, and the normalization performed by dividing by the sum of the exponential terms, so that the measured intensity is given by

$$I = \left(\sum_{i=1}^{n} T(B) \times \beta_i \right) \Big/ F \qquad (4.11)$$

$$\text{where} \quad F = \sum_{i=1}^{n} \beta_i \qquad (4.12)$$

The summation is over the points within the radius R.

Therefore to convolve the grid values with a given beam, the position angle of the beam α , the half-power beam widths and the distance to the object, have to be specified. The convolved points in the rectangle BCEF (fig. 4.5), were obtained from symmetry, the value at the point F being equal to that at the point D.

4.5 Addition of source to centre.

As already mentioned, the model of Brindle et al. (1978) has no source of extra emission at the centre of the Galaxy, and my models simply extrapolate the model to the centre. Therefore in order to make the computed maps more comparable to the observations, a point source of emission was added. This extra emission was added after the convolution had been executed, since the convolution of a point source simply mirrors the beam shape.

4.6 Presentation of Results.

Having convolved the grid points, and added a point source, a contour map was produced, and also profiles of the emission along the major and minor axes of the galaxy. The G.P.C.P. (General purpose contouring program) was used, but it was found that its memory was not sufficient to handle all the grid points, so every fourth point was in practise convolved and plotted. A flow diagram showing the production of a contour map and profiles is shown in fig. 4.6

Fig. 4.6

Flow diagram for the production of the contour maps of synchrotron emission from external galaxies.

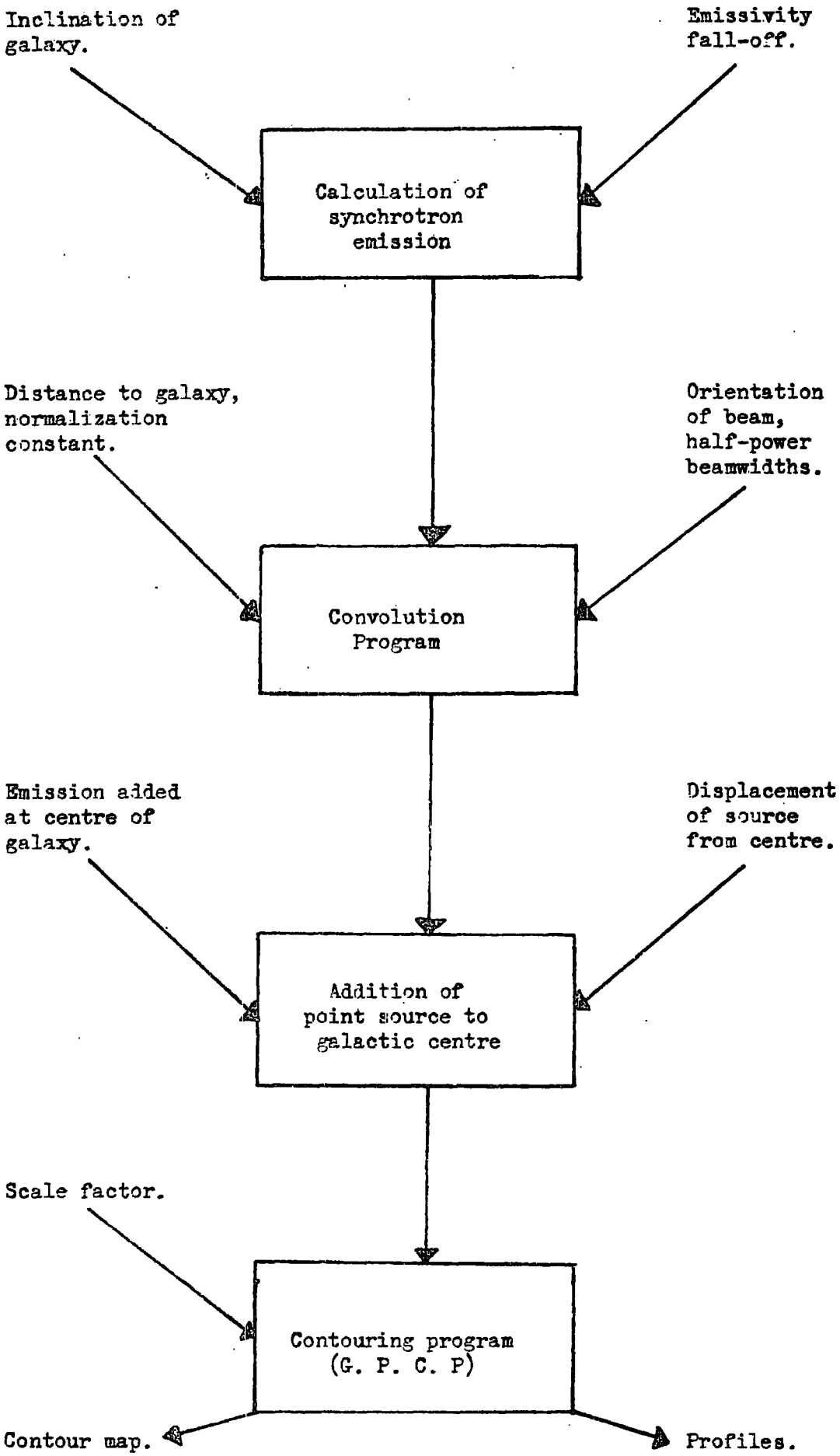

Chapter 4 - References

Brindle, C., French, D.K. and Osborne, J.L. 1978, Mon. Not. R. Astr. Soc. (in the press).

Kraus, J.D. 1966, Radio Astronomy. (McGraw - Hill) ch. 3.

Pacholczyk, A. G. 1970 Radio Astrophysics. ch. 3. W. H. Freeman & Co.

Comparison with Observations and Conclusions.

5.1 Introduction.

The object of this chapter is to present the results of the modelling of the edge-on galaxies NGC 4631 and NGC 891, and to draw some conclusions from the results.

The observations chosen for comparison with the predictions, have been made by the Westerbork Synthesis Radio Telescope. This telescope is a 12-element, Earth rotation, aperture-synthesis instrument. Ten of the elements are fixed on an East-West line at intervals of 144 meters, and two elements are moveable along a high-precision track running East-West. The elements are equatorially mounted, parabolic reflector antennae of 25 meters diameter. All twelve antennae have reflectors that have dimensions identical to within 1 mm, making the telescope essentially perfect at 21-cm observations, and usable at 6-cm. The length of the array gives a resolution in seconds of arc about equal to the operating wavelength in cm (20 arcsec. = 20 cm wavelength), in Right Ascension, the beamwidth in Declination being proportional to cosec. δ .

The design of the telescope is such that in a 12-hour observing period, 20 baselines can be measured simultaneously. Operating at 1415 Mhz, the effective bandwidth is 45Mhz, and the system noise temperature 240 K. At 610 Mhz the bandwidth is also 45Mhz, but the noise temperature has increased to 380 K. The radio receivers are equipped with parametric amplifiers, and the configuration and size of the elements leads to an r. m. s. noise of 10^{-29} Wm^{-2} Hz^{-1} , after a measurement of 12 hours duration. The radio contour maps, produced by the telescope, are made with respect to an arbitrary background level. Fig. 5.1 shows the geometrical lay-out of the radio-telescope, and 5.2 the cross-section of the synthesized beam.

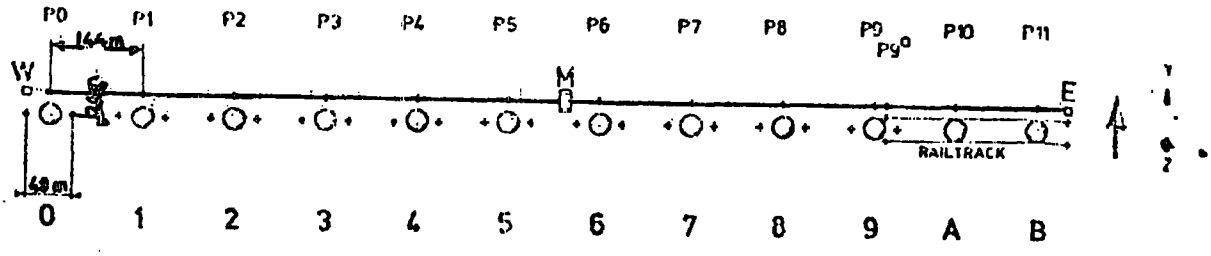

Fig. 5.1

Plan view of the geometrical lay-out of the Westerbork Synthesis Radio Telescope (Baars and Hooghoudt 1974). The points W - M - E determine the reference baseline, and the crosses indicate measuring points from which the antennae are placed on a straight, horizontal east-west line.

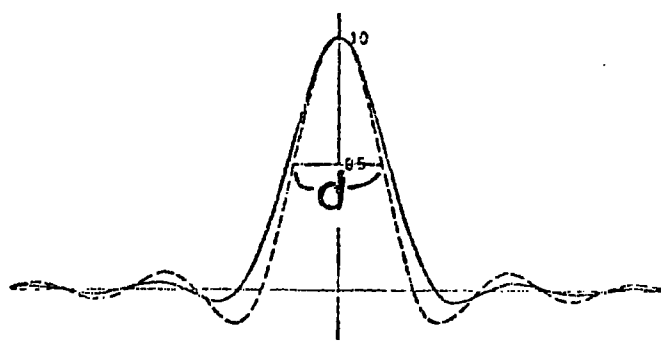

Fig. 5.2

Cross-section of the Westerbork synthesized beam (Högbom and Brouw 1974). Solid line is the response curve for the standard gaussian grading, and the dashed line the narrower beam that can be obtained with a uniform grading. The half-power beam width d is given by $0.8/R$ radians in Right Ascension, and $0.8/R \sin\delta$ radians in Declination, where R is the maximum interferometer spacing in wavelengths.

5.2 Maps of the Synchrotron Emission from an edge-on view of the Galaxy.

Two maps of an edge-on view of the Galaxy are shown in figs. 5.3 and 5.4. The former one shows the emission predicted from the model with an emissivity decreasing linearly with Z - distance, and the latter that predicted from the model with an emissivity dependent on both Z and R, as discussed in Chapter 2. From now on these two models will be referred to as model 1 and model 2, respectively. Both maps are in units of brightness temperature at 150 Mhz, and both have no extra source of emission added at the centre.

It can be seen from these two maps, that model 1 produces more emission from the central region of the Galaxy, than does model 2, whereas model 2 produces more emission at large radii and also an extensive halo of emission. Such a low brightness temperature halo would not be detectable at distances of more than a few megaparsecs, with present day telescope sensitivities.

Figs. 5.5 and 5.6 show the emission profiles along the major and minor axes, for both models, respectively. From the two maps emissivities ($^{\circ}$K / kpc), at various points, are presented in table 5.1 and compared with those given by Webster (1975). These values have been scaled to 408 Mhz using a brightness temperature spectral index of 2.8. Webster's halo is a uniformly emitting spherical region of radius between 10 and 15 kpc, so that the emissivity is constant throughout the halo. The model 2 emissivities are lower than the corresponding model 1 ones, in the inner regions of the Galaxy, but the emission extends to nearly 22 kpc above the plane instead of 5.5 kpc. Despite these differences, the ratio of the luminosity produced by model 1, to that produced by model 2, is 0.98.

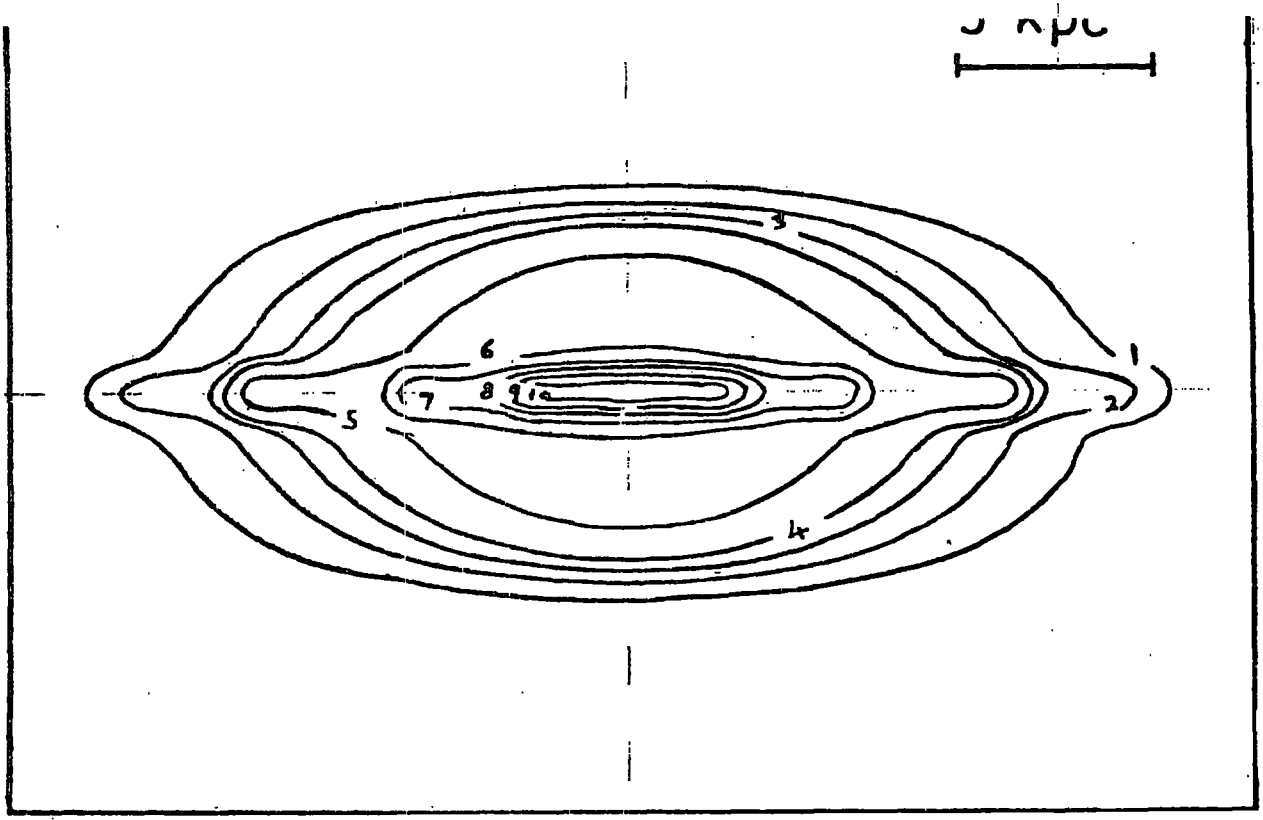

Fig. 5.3

150 Mhz brightness temperature distribution predicted by model 1. The contour levels , 1, 2 etc., are 150 from 150 to 600, and 1000 from 1000 onwards, ^{o}K.

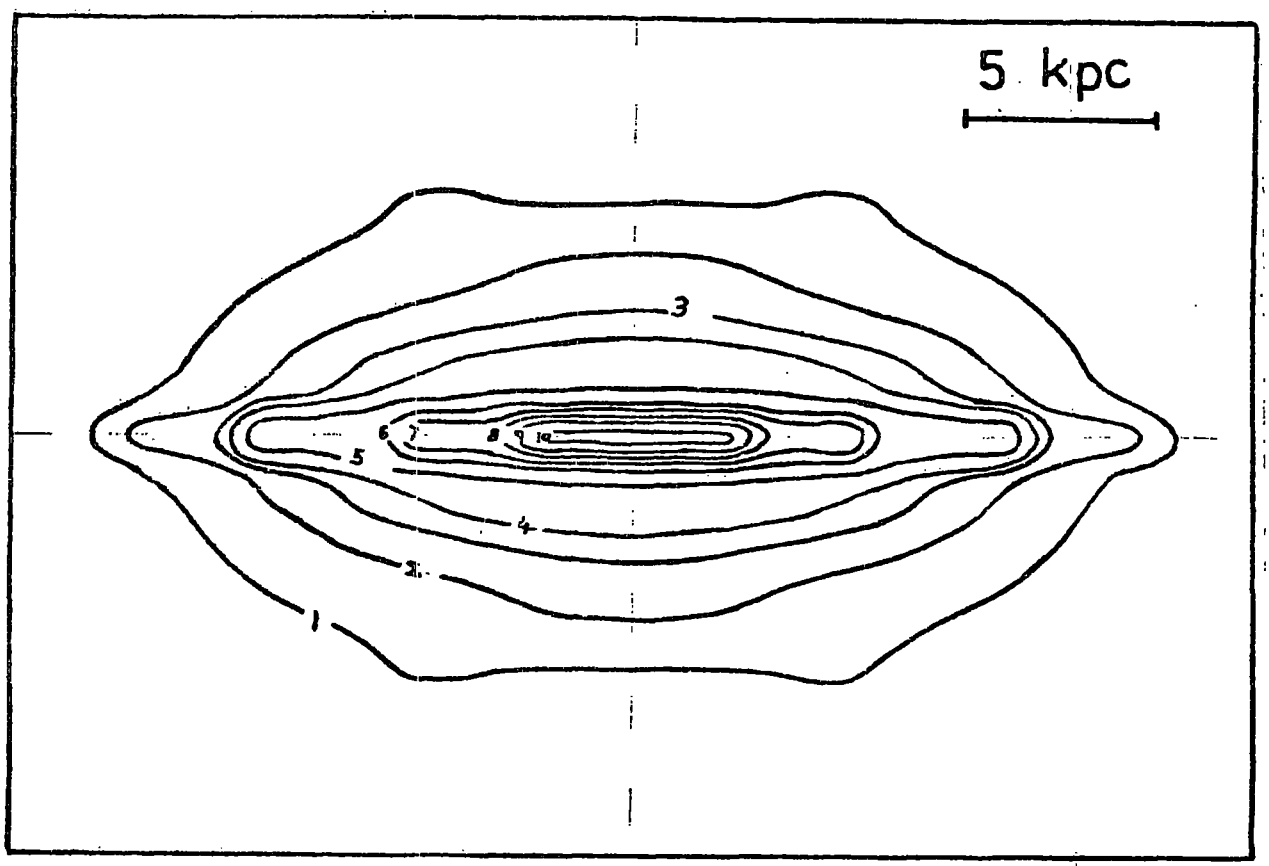

Fig. 5.4

150 Mhz brightness temperature distribution predicted by model 2. The contour levels are the same as above.

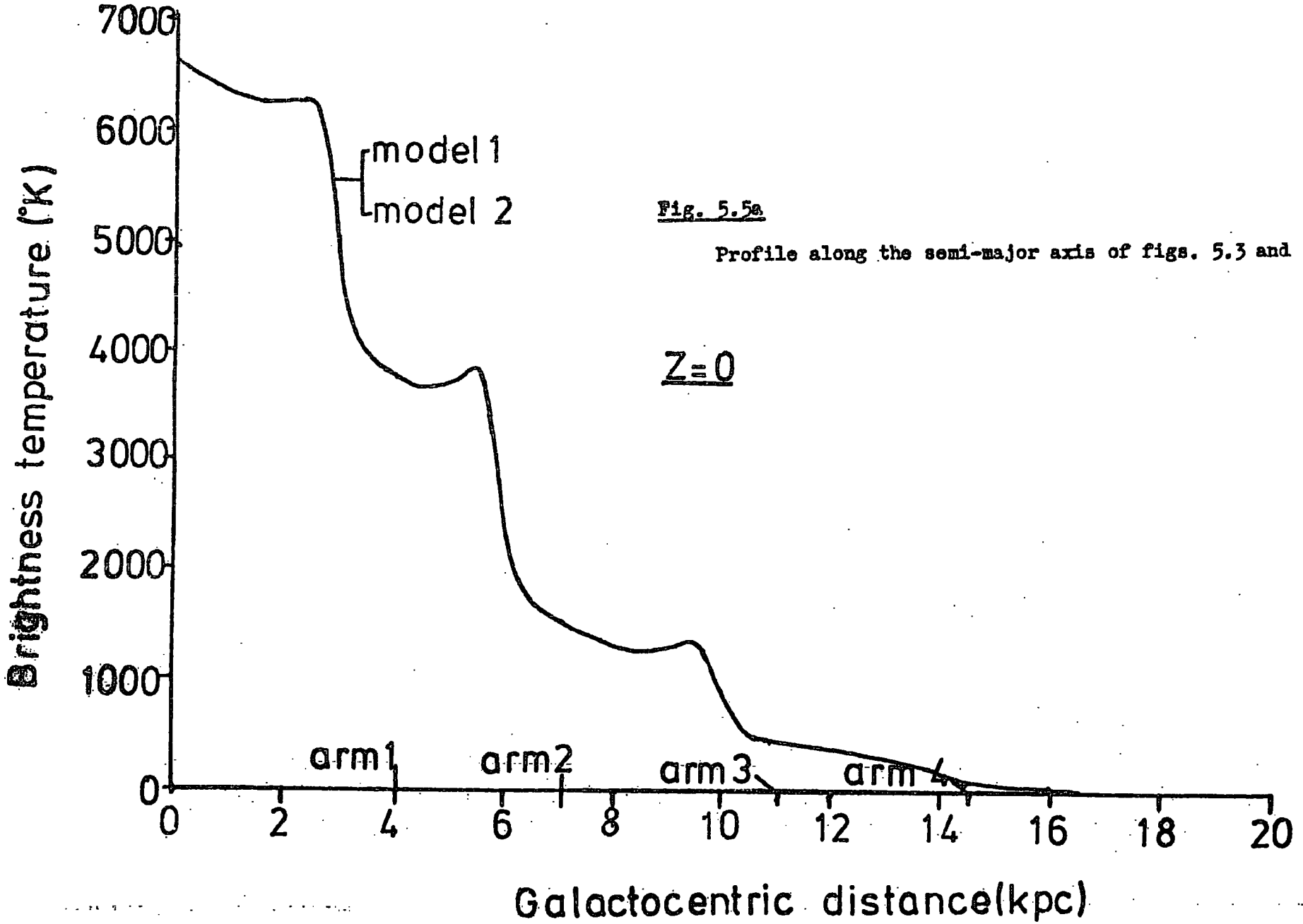

Fig. 5.5a

Profile along the semi-major axis of figs. 5.3 and 5.4

Z=0

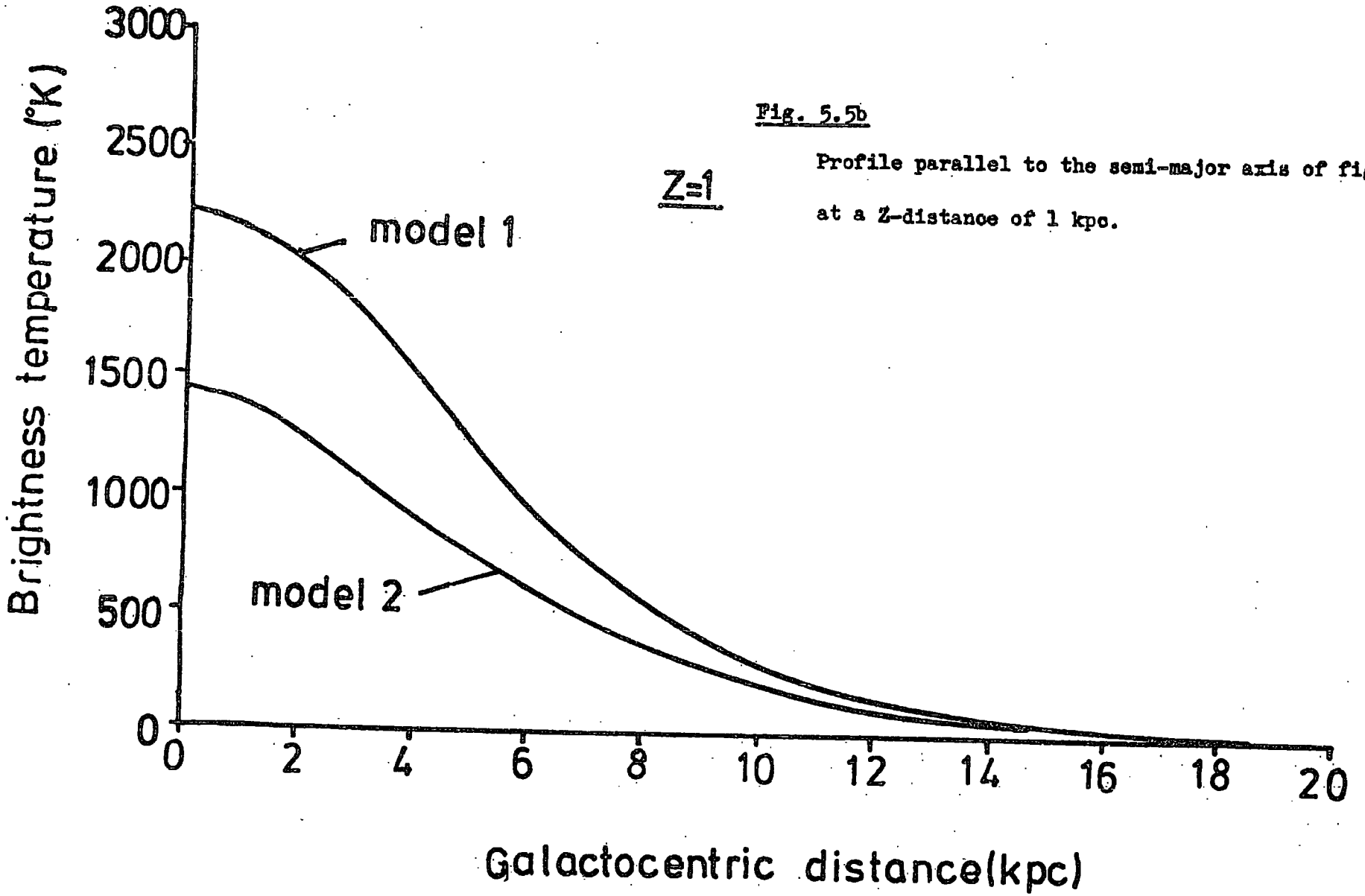

Fig. 5.5b

Profile parallel to the semi-major axis of figs. 5.3 and 5.4 at a Z-distance of 1 kpc.

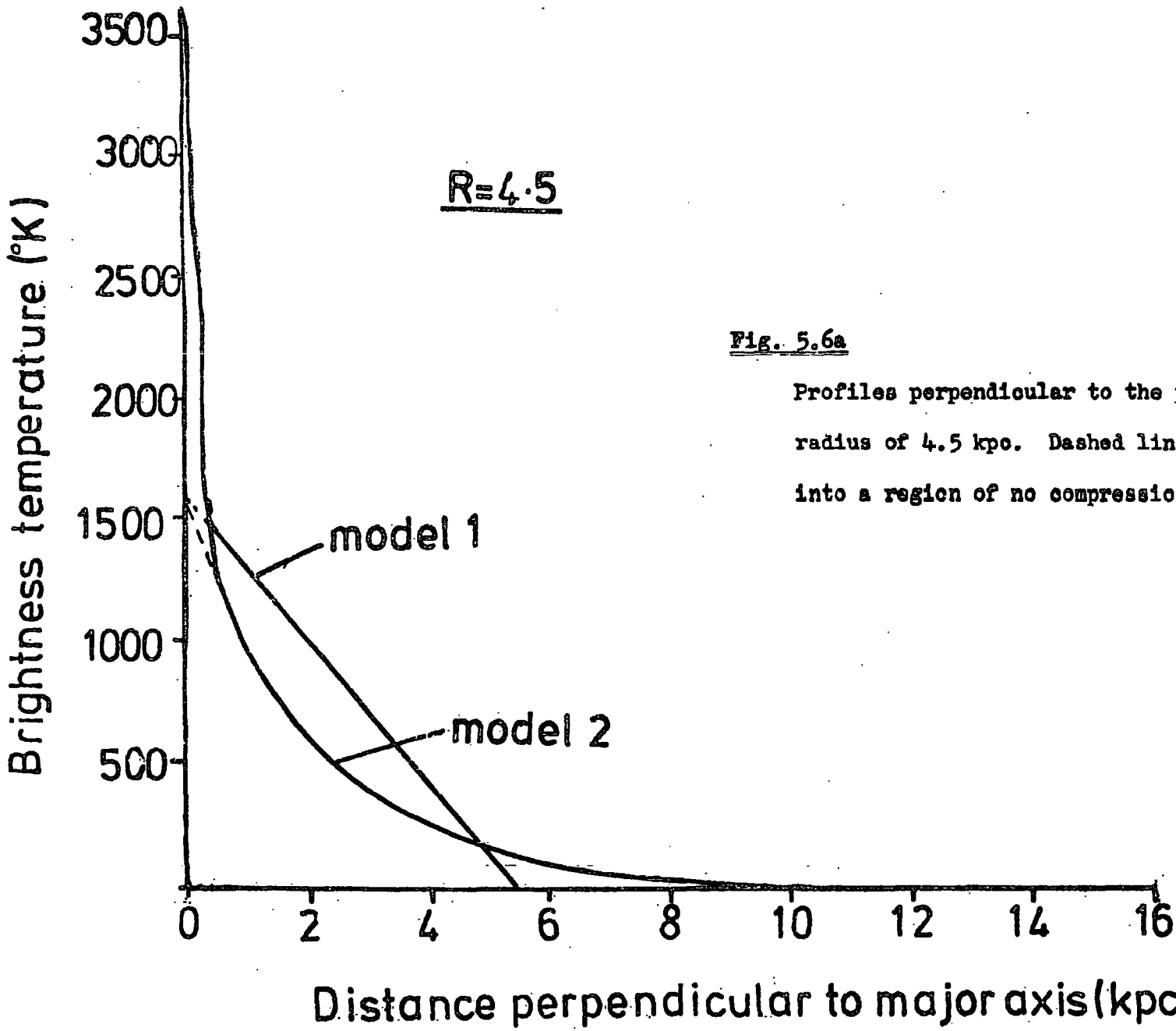

Fig. 5.6a

Profiles perpendicular to the plane of figs. 5.3 and 5.4, at a radius of 4.5 kpc. Dashed lines are the extrapolated profiles into a region of no compression.

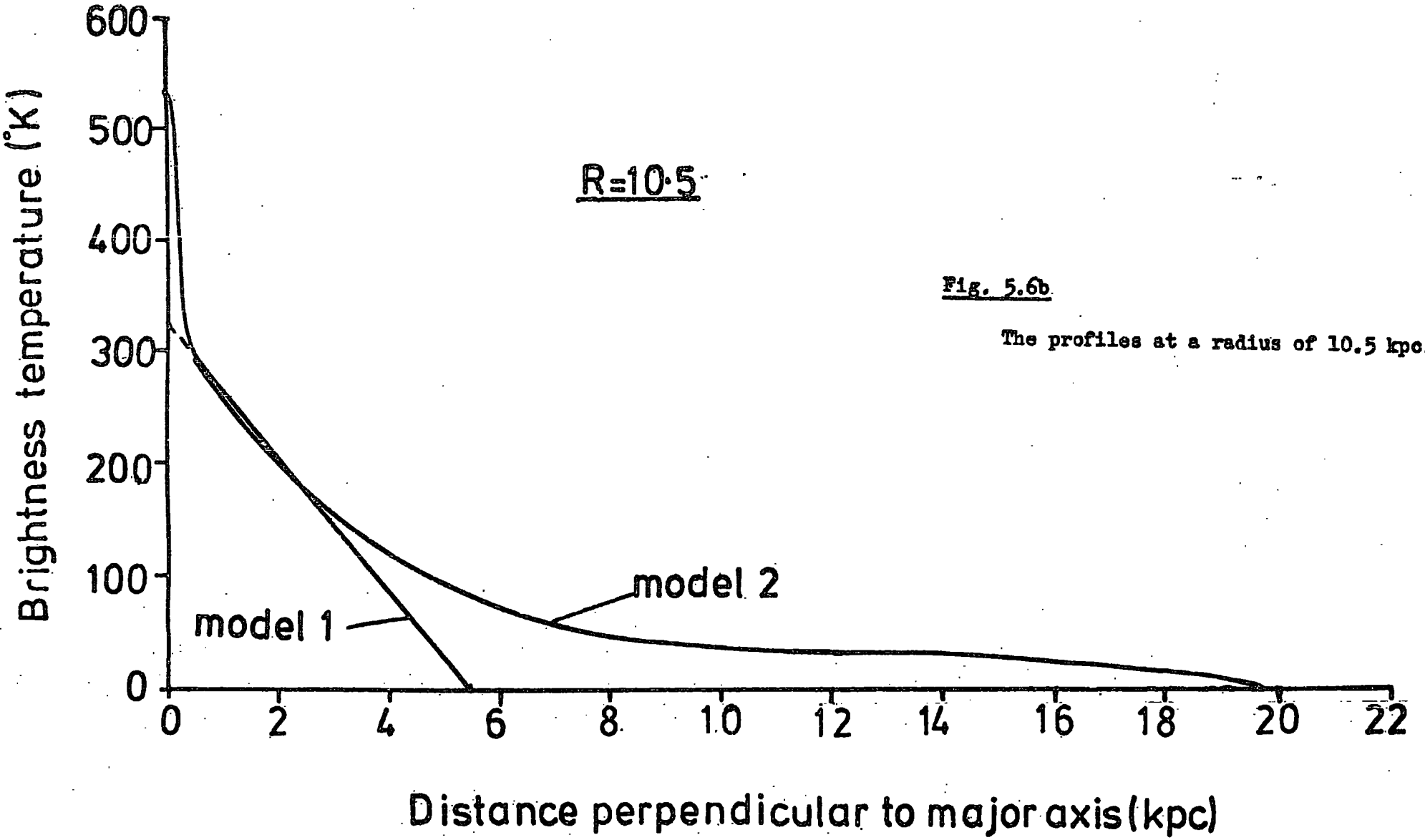

Fig. 5.6b

The profiles at a radius of 10.5 kpc.

Table 5.1

Comparison of emissivities (°K/kpc) produced by models 1 and 2 with those of Webster (1977), at 408 Mhz. The model predictions have been scaled by $\left(\frac{150}{408}\right)^{2.8}$, ($\beta$ = 2.6).

Galactocentric distance (kpc)	Z-distance (kpc)	Model 1 emissivity	Model 2 emissivity	Webster emissivity
0	10	0	0.08	0.3
0	9	0	0.11	"
0	8	0	0.14	"
0	7	0	0.20	"
0	6	0	0.29	"
0	5	0.49	0.54	"
0	4	1.48	0.75	"
0	3	2.47	0.99	"
0	2	3.46	1.61	"
0	1	4.45	2.97	"
inner 3 kpc region	0	13 (30 kpc path length)	13	~ 20

5.3 Comparison with NGC 891.

The Westerbork radio maps chosen for comparison with the model predictions are the 610 and 1412 Mhz ones. The half-power beam widths for these two maps are 57" x 85" (3.8 x 5.7 kpc, for adopted distance of 14 Mpc) and 25" x 37" (1.7 x 2.5 kpc), respectively. Since the resolution of the former map is much inferior to the latter one, the main comparison will be made with the 1412 Mhz map. As discussed later on, the thermal emission at this frequency is estimated to be a small fraction of the radio-continuum emission.

To allow for the much greater size of NGC 891 compared with the Galaxy, the linear scales of the maps were scaled up by 1.5. The predicted maps of the two models, which have been convolved to the resolution of the 1412 Mhz map and normalized to bring the predicted brightness temperatures into agreement with the observed ones, are shown in figs. 5.7 and 5.8. It is apparent that model 2 produces a much too extended halo of emission around the galaxy, and the model 1 emission also extends too far. To bring the Z-extent of the emission predicted by model 1 into agreement with the observed extent of $\sim$ 6 kpc, the map scale in the Z-direction was adjusted so that the boundary is at 6 kpc, instead of the 8.25 kpc one produced by scaling up by 1.5. The model 1 map produced this way is shown in fig. 5.9. Fig. 5.10 shows the model 2 map produced the same way. Profiles of the emission along the major and minor axes of the galaxy are shown in figs. 5.11 and 5.12, respectively, with the observed profiles superimposed. As can be seen from the major axis profiles the model 1 profile gives quite a good fit, the model 2 profile producing too little emission near the galactic centre. From the minor axis profiles it can be seen that the model 1 profile is much broader than the observed profile, whereas the model 2 profile does not fall off rapidly enough at large Z-distances. Overall, the distribution

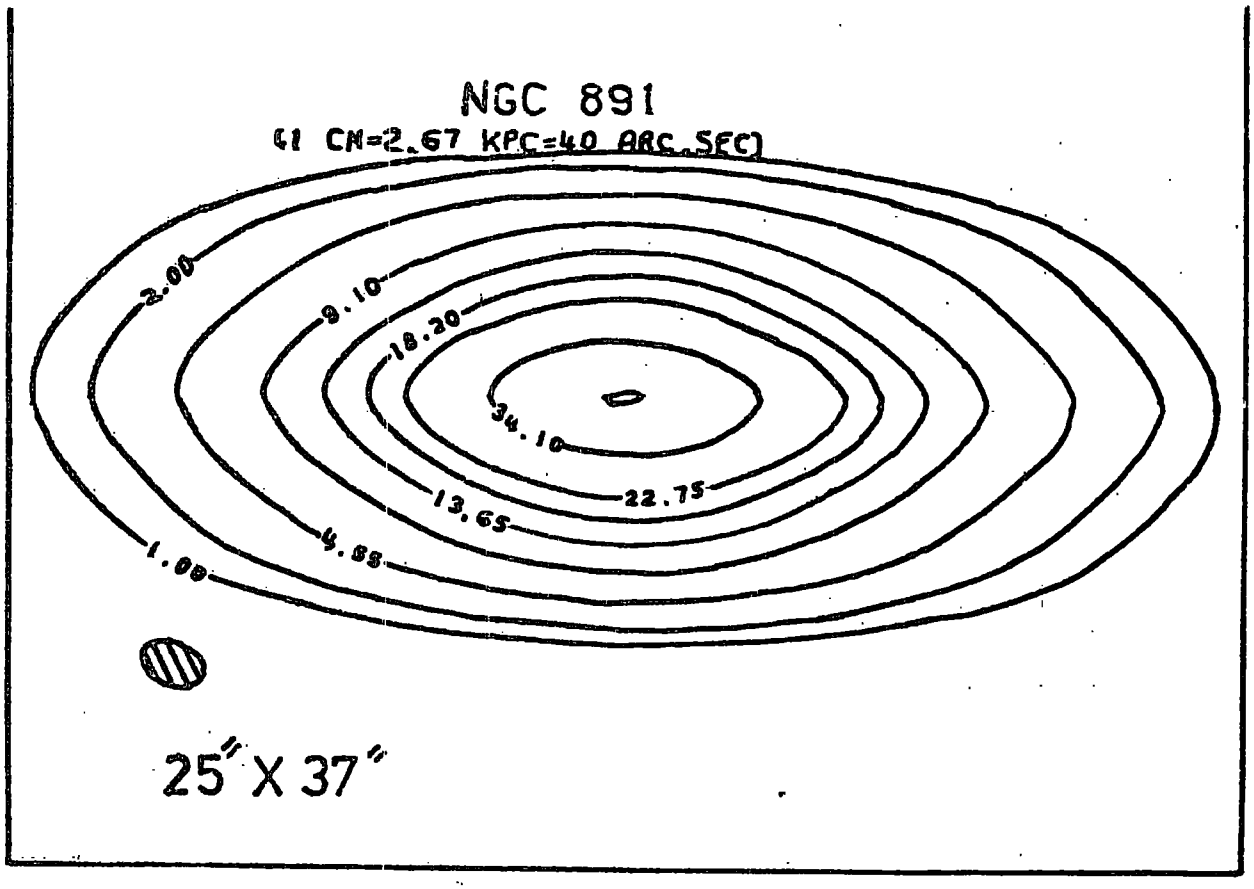

Fig. 5.7 Computed 1412 Mhz map by model 1, scaled up by 1.5 x 1.5

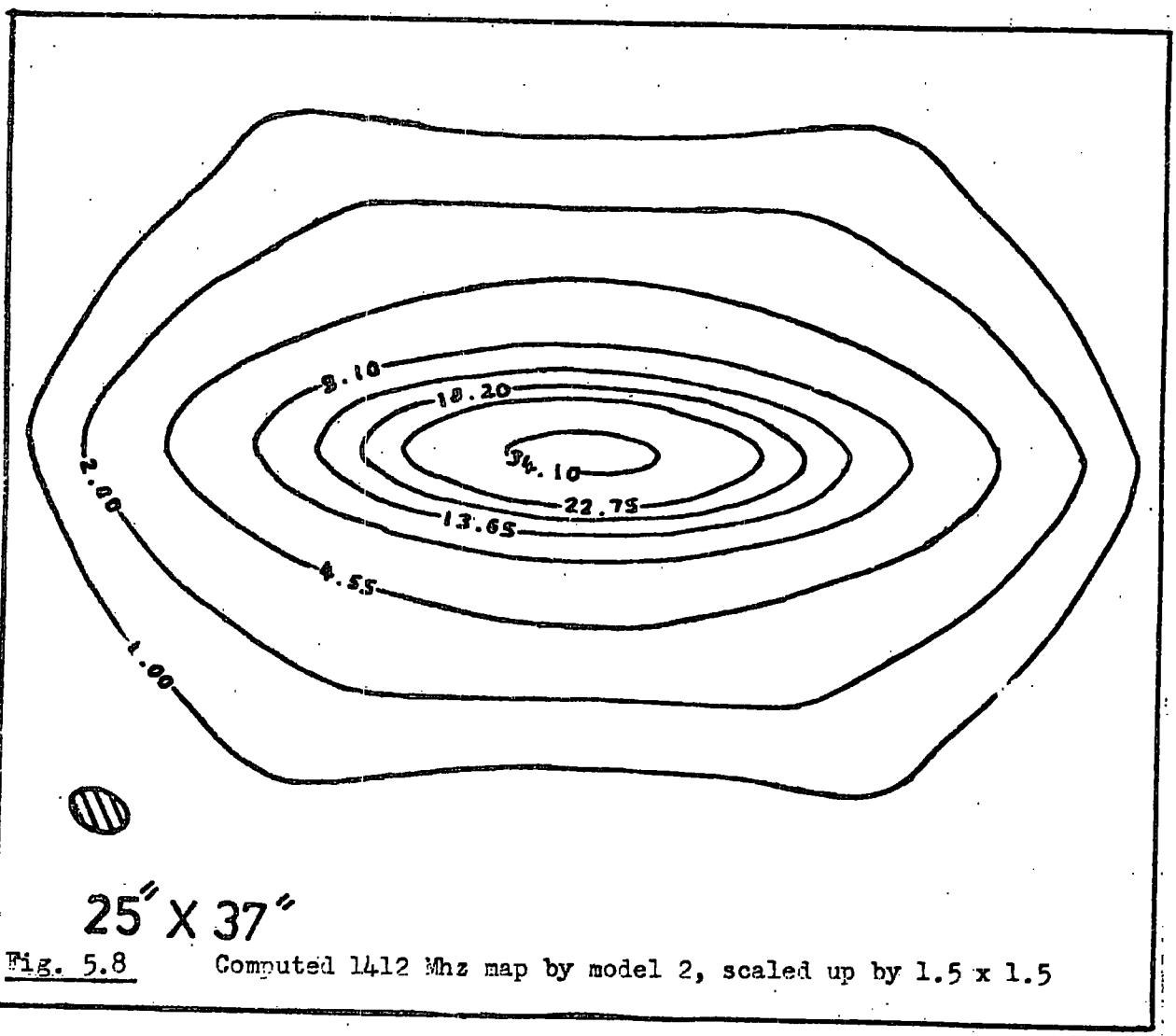

Fig. 5.8 Computed 1412 Mhz map by model 2, scaled up by 1.5 x 1.5

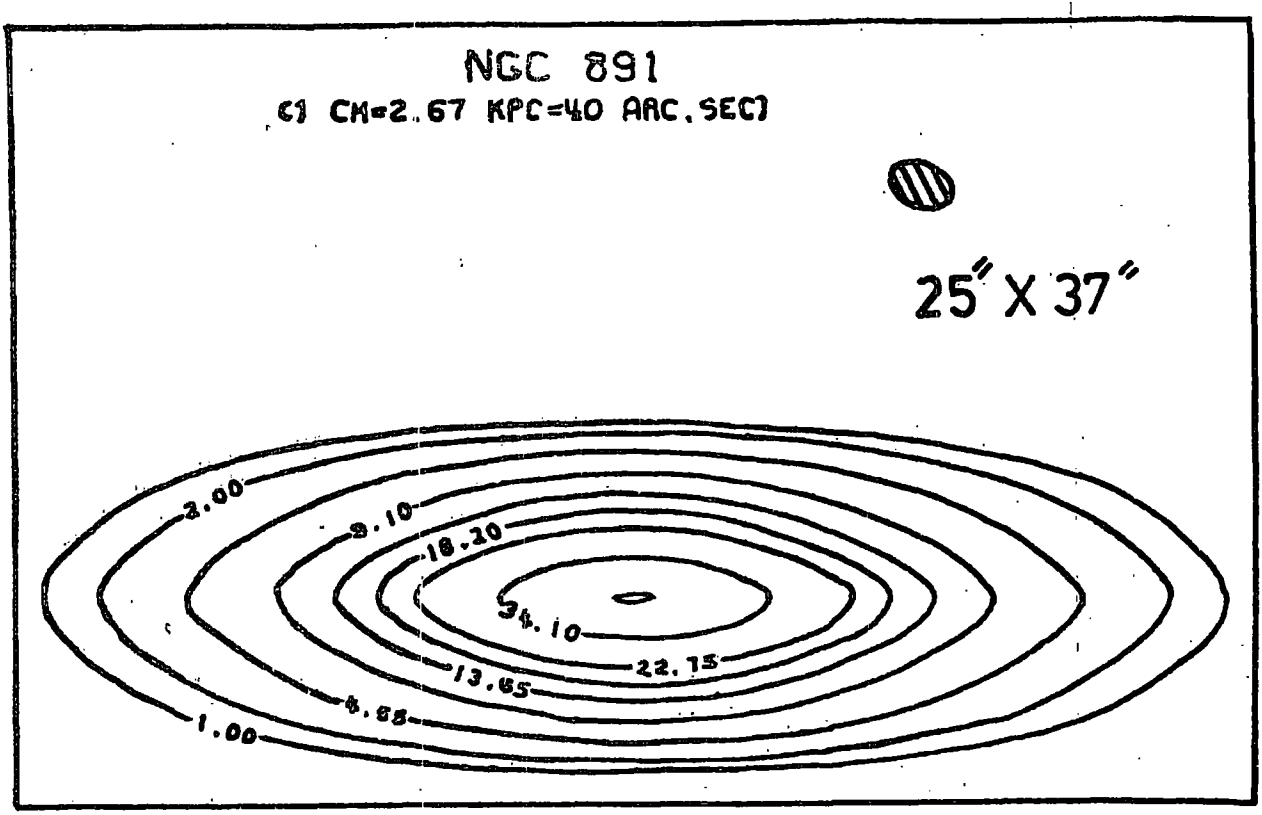

Fig. 5.9

Computed 1412 Mhz map by model 1, scaled up by 1.5 x 1.1.

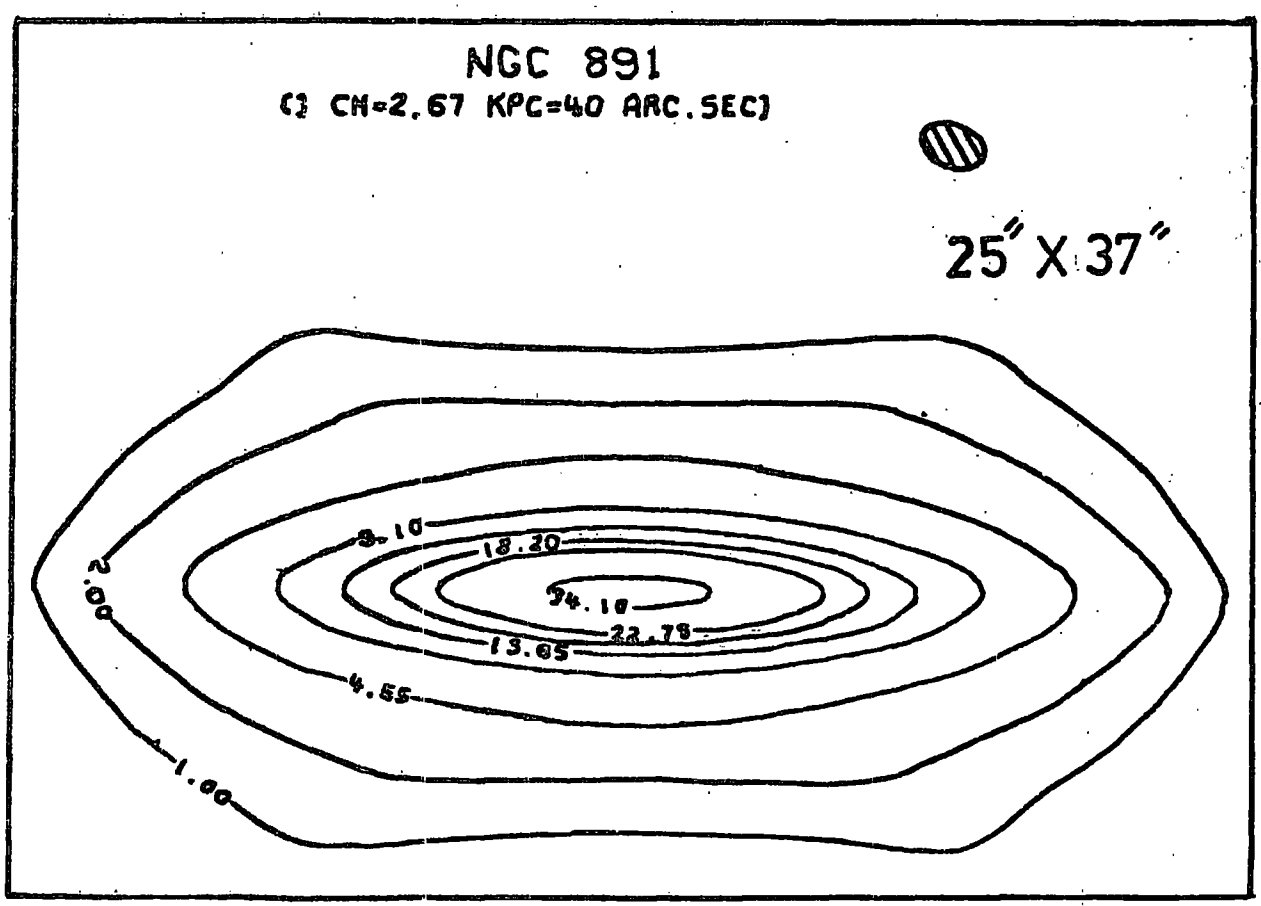

Fig. 5.10

Computed 1412 Mhz map by model 2, scaled up by 1.5 x 1.1.

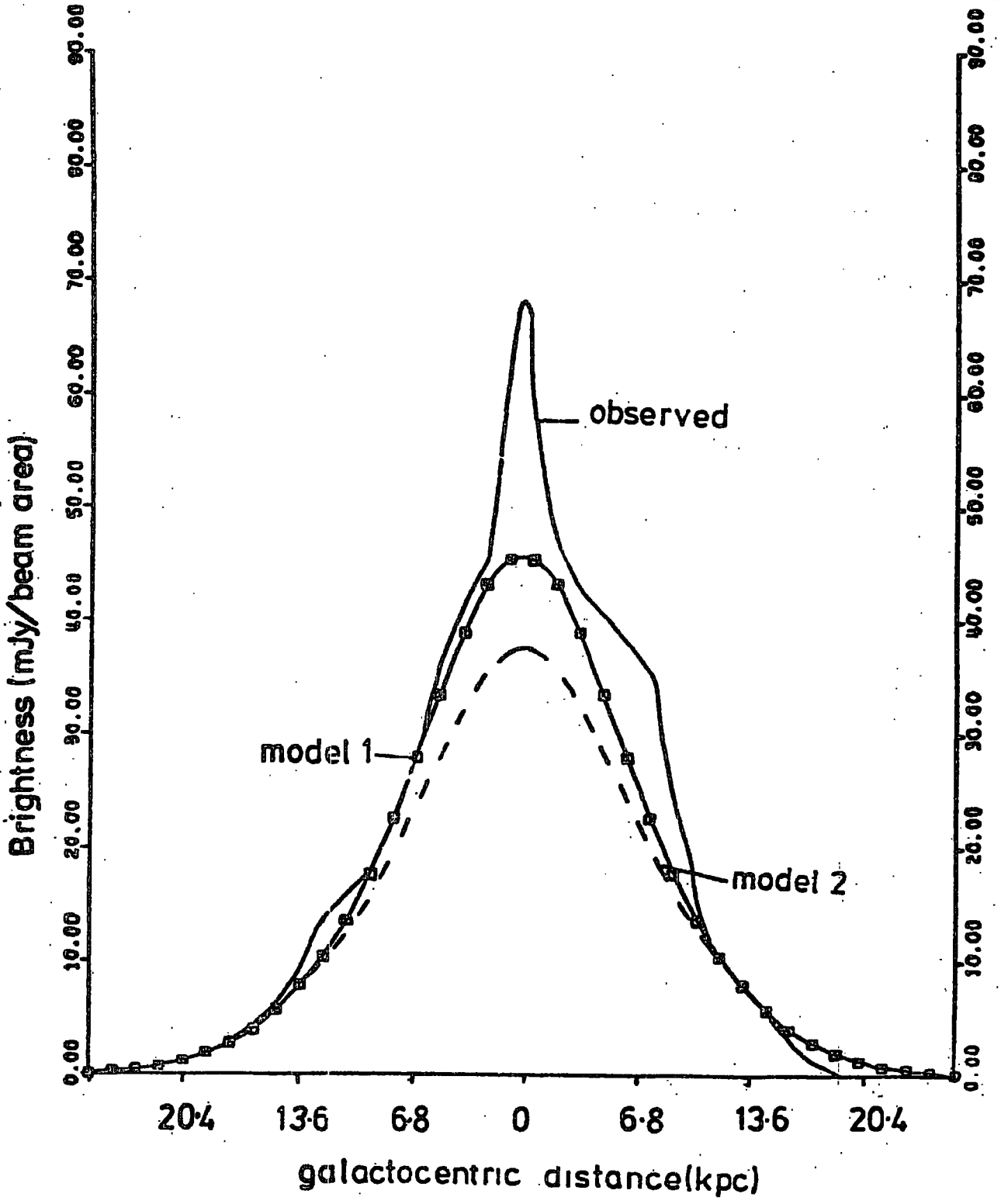

Fig. 5.11

The predicted profiles along the major axis of NGC 891, with the 1412 Mhz profile superimposed.

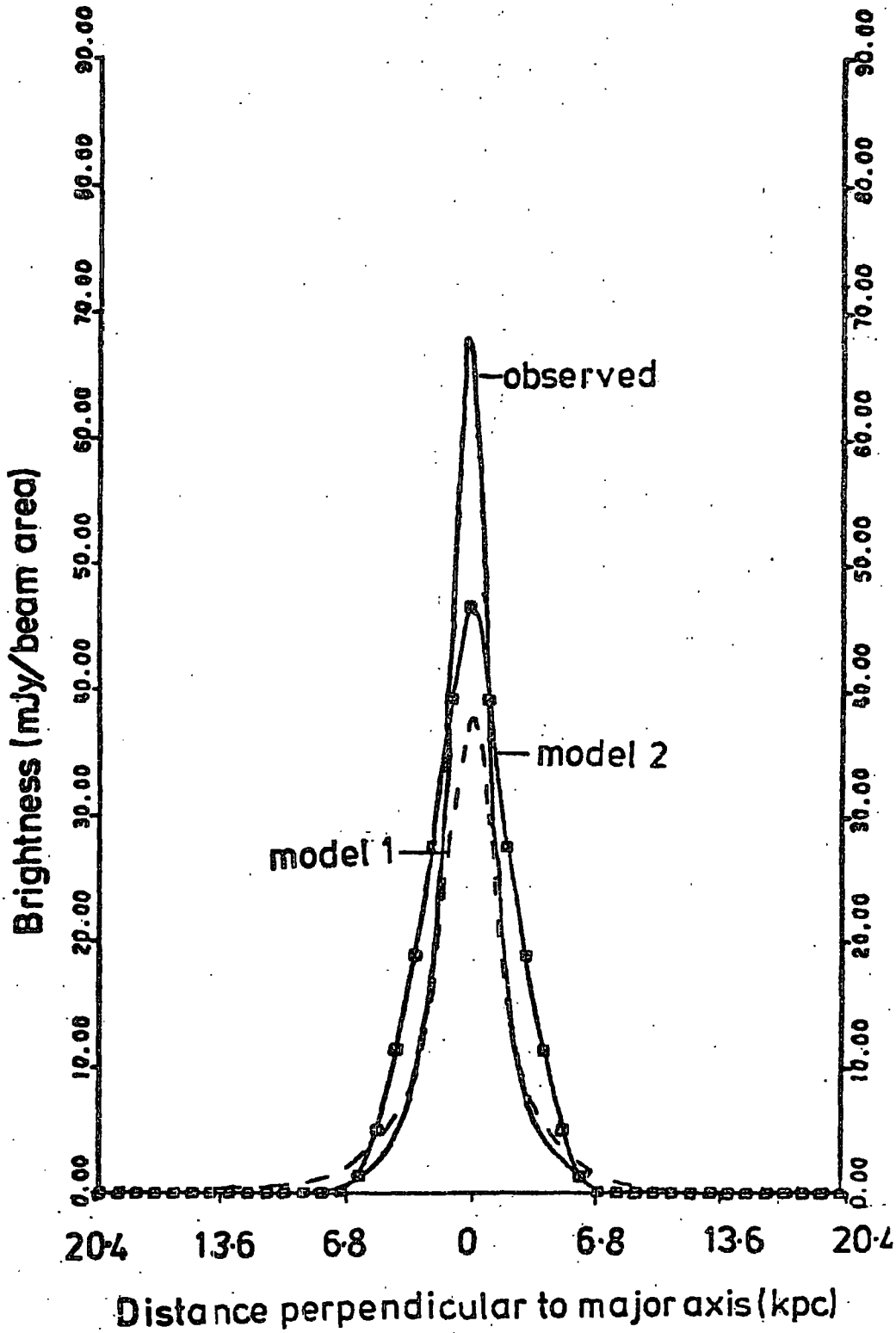

Fig. 5.12

The predicted profiles perpendicular to the major axis at R = 0, of NGC 891, with the observed 1412 Mhz profile superimposed. (No extra source of emission has been added at the centre).

of emission about NGC 891 more nearly resembles that of model 1, though the emissivity fall-off can not simply be linear with Z-distance.

As can be seen from fig. 5.11 there is an unresolved source of emission at the centre of the galaxy. To make the model 1 map more comparable with the observed one, an extra source of emission was added at the centre. This map is shown in fig. 5.13, and the profiles in figs. 5.14 and 5.15. This map is drawn to the same scale as fig. 3.10b. Table 5.2 shows the various parameters used to produce this map.

Table 5.2

Assumed distance (Mpc)	14
Scaling up factors	1.5 (R-direction) 1.1 (Z-direction)
Position angle of telescope beam	-25.0°
Half-power beam widths	25" x 37"
normalization constant	0.0189
Extra emission added at centre (K)	50

The normalization constant is the amount the 150 Mhz predictions of the Galaxy have to be multiplied by to obtain agreement with the observations. NGC 891 is therefore approximately 6·6 times brighter than the Galaxy at 1412Mhz (β = 2.6).(T_b(°k)/5(mJy/beam area) = 0·66)

Allen, Baldwin and Sancisi (1977) have averaged the 1412 Mhz emission in strips 195" (13 kpc) in length parallel to and 12" (0.8 kpc) in width perpendicular to the major axis, in order to improve the signal to noise ratio. Fig. 5.16 shows this profile with the model 1 profile superimposed, the predictions having been averaged as above. As can be seen from this

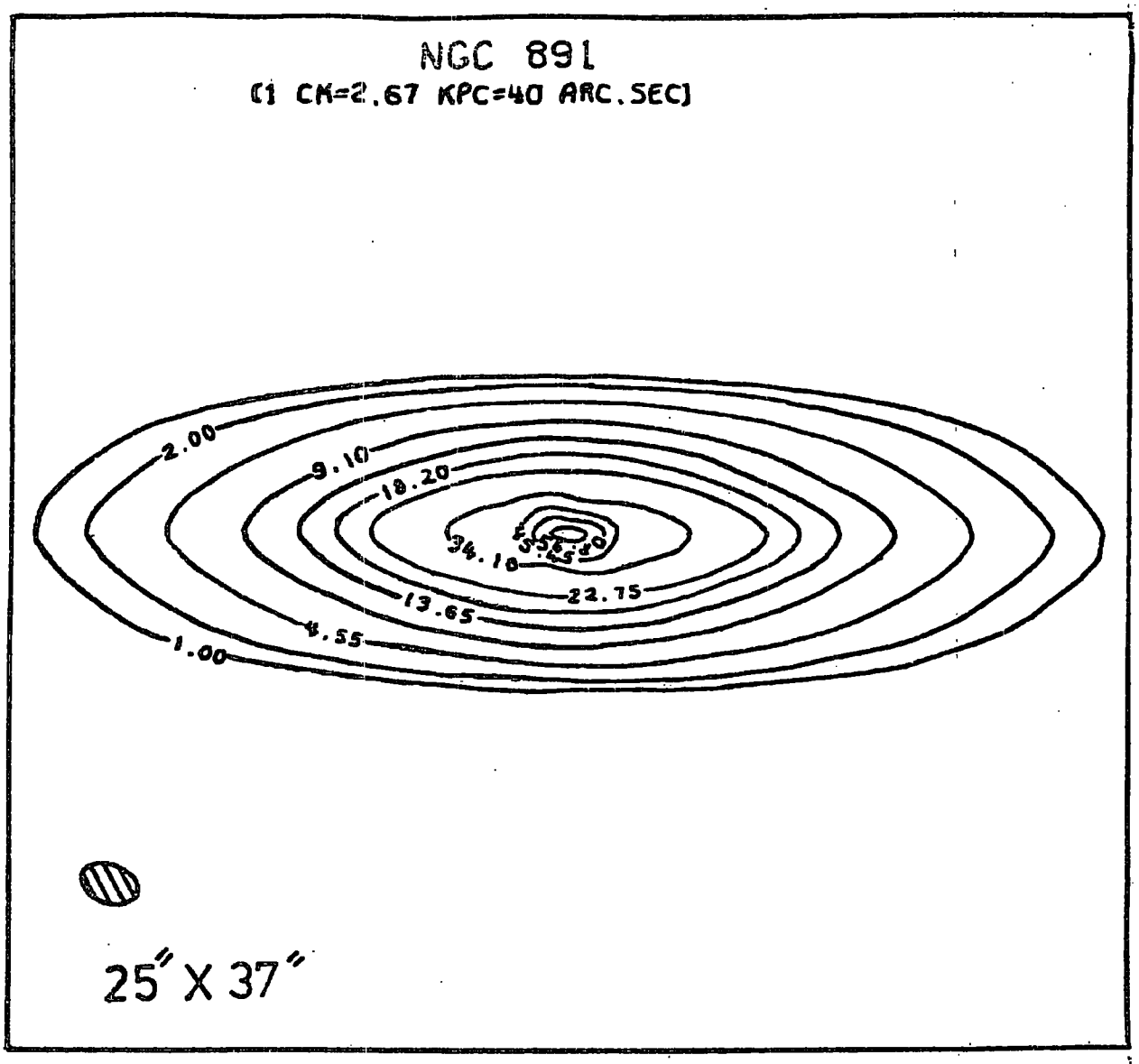

Fig. 5.13

The computed 1412 Mhz map of NGC 891, with a point source of emission added at the centre. The map is drawn to the same scale as fig. 3.10e. The contour intervals are also the same.

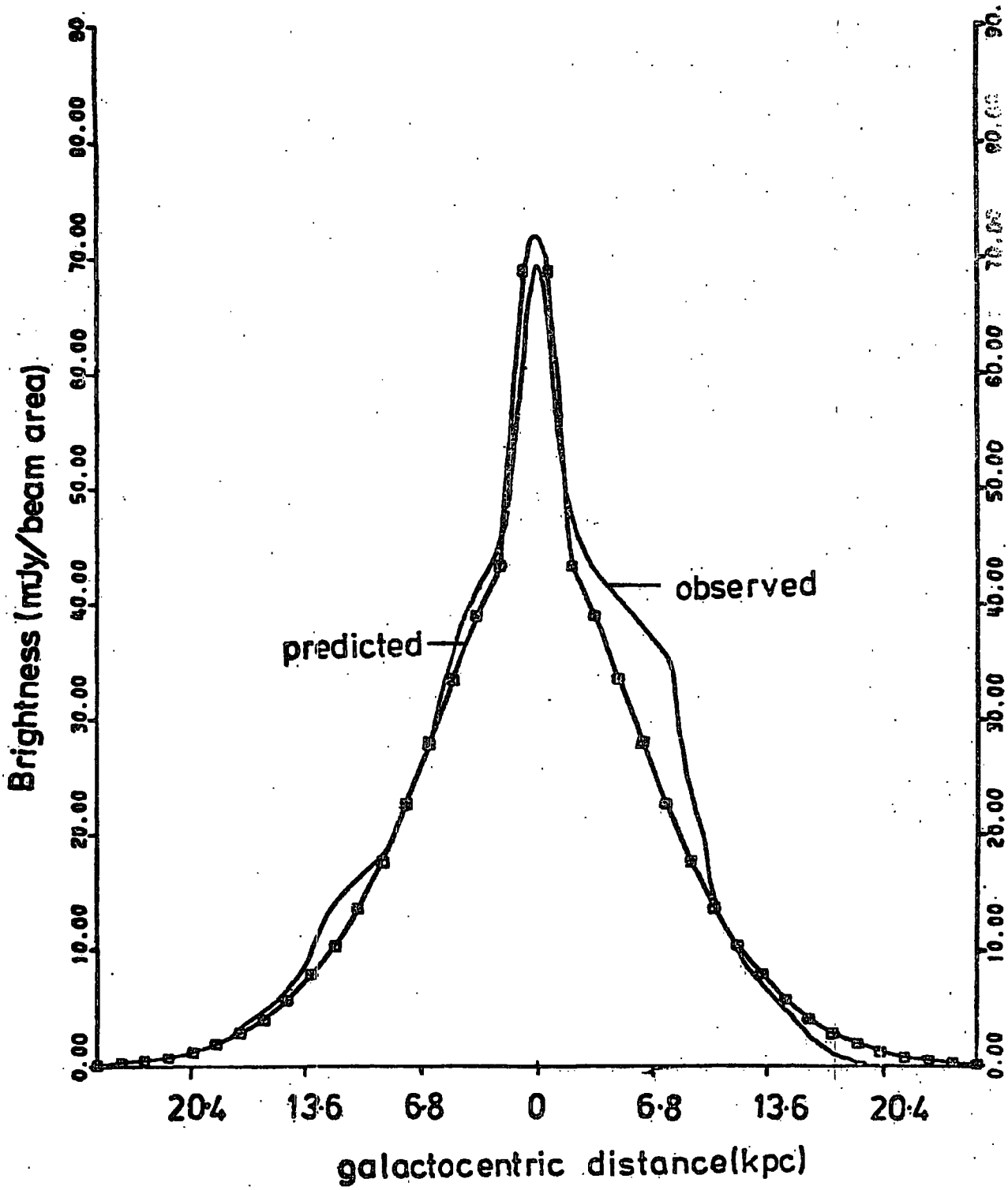

Fig. 5.14

The 1412 Mhz predicted and observed profiles along the major-axis of NGC 891, after a point source of emission has been added at the centre.

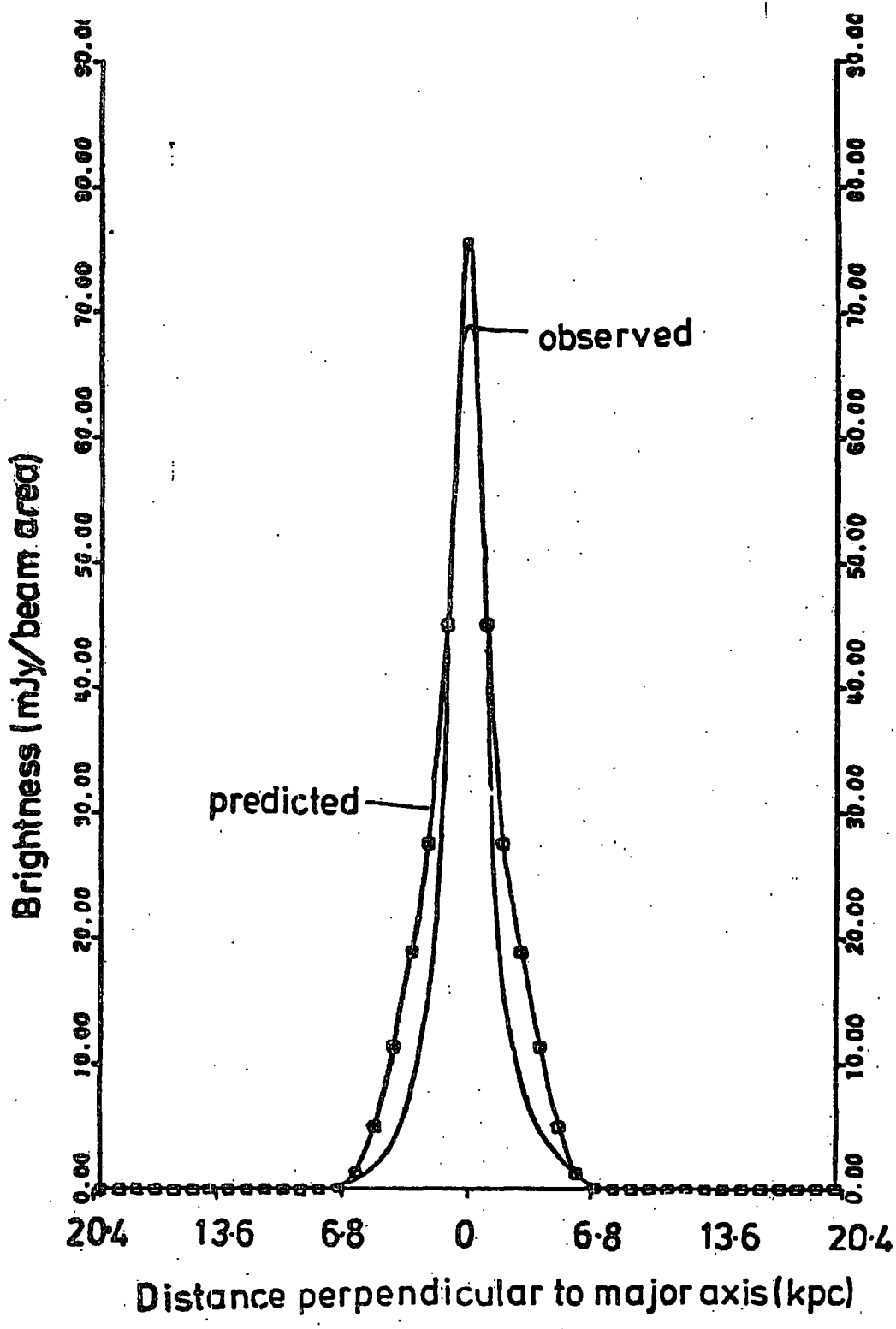

Fig. 5.15

The observed and predicted 1412 Mhz profiles, after a point source of emission has been added at the centre, to the predicted map.

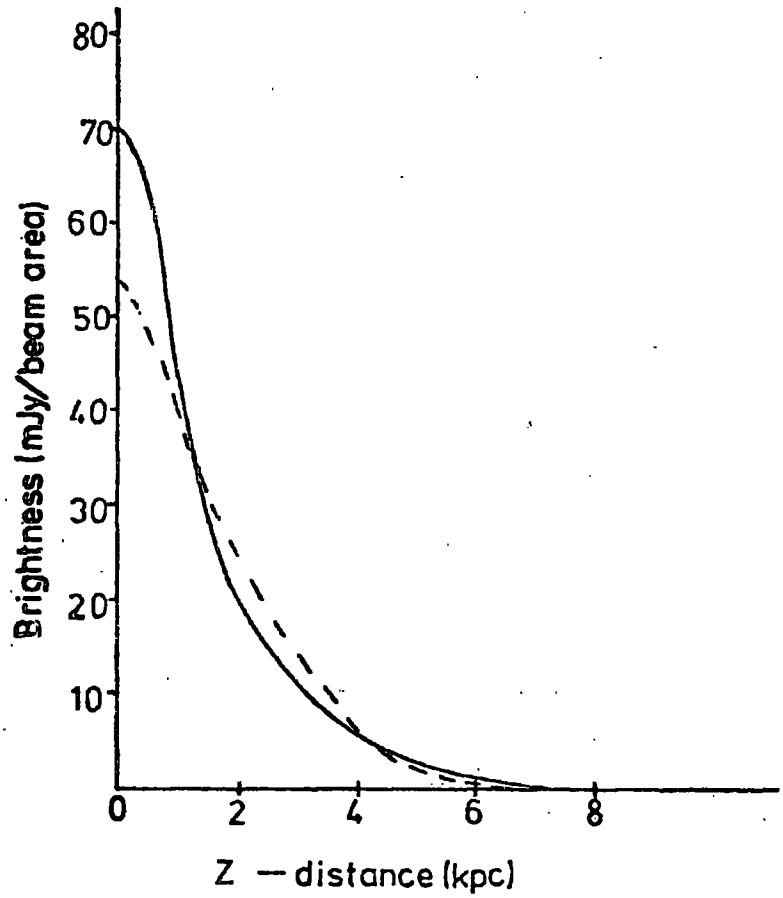

Fig. 5.16

The observed and predicted profiles along the minor axis of NGC 891 at 1412 Mhz, after the emission has been averaged in strips 13 kpc in length parallel to the major axis and 0.8 kpc in width. The dashed line is the predicted curve.

profile, the observed emission falls off rapidly out to about 2 kpc and then approximately exponentially out to 6 kpc, whereas the predicted profile is practically linear between 1 and 4 kpc.

A 610 Mhz map has been computed for model 1, by scaling the 1412 Mhz predictions by $\left(\frac{1412}{610}\right)^{2.8}$ and convolving with the 57" x 85" elliptical beam. This map is shown in fig. 5.17, and the observed and predicted profiles, along the major and minor axes, in figs. 5.18 and 5.19. The former profile gives a reasonable fit, but the Z profile is again too broad. Fig. 5.20 shows the 610 Mhz profiles perpendicular to the major axis, after having been averaged in strips 180" (12 kpc) in length and 30" (2 kpc) in width, as presented by Allen et al. (1977). The agreement is seen to be better after this averaging process has been done.

NGC 891 has also been mapped at 4995 Mhz (6 cm) by Allen, Baldwin and Sancisi (1977) and 408 Mhz by Baldwin and Pooley (1973). The half-power beam widths of the telescope beams are 11".1 x 17" (0.7 x 1.1 kpc) and 80" x 120" (5.7 x 8 kpc), respectively. At 5 Ghz the disc seems to consist of two components; one is similar to the HI disc and could be thermal, while the other is nonthermal and extends to about 4 kpc in the Z-direction (Allen et al. 1977). The 408 Mhz variation of emissivity at Z = 0 with radius, and that for the Galaxy, is shown in fig. 5.21 (Baldwin and Pooley 1973). Fig. 5.22 shows the brightness profile along the major axis of NGC 891, and that for the Galaxy (Baldwin and Pooley 1973). These values have been computed for an assumed distance to NGC 891 of 7 Mpc. As can be seen from these two figures, the emissivity and brightness temperature distributions can be reasonably well approximated by an exponential fall off.

To conclude this section, model 1 can account for the radio-continuum emission of NGC 891 reasonably well. Some possible explanations for the much higher radio luminosity of NGC 891, than the Galaxy, will be given later on.

NGC 891

(1 CM=6.77 KPC=100 ARC SEC)

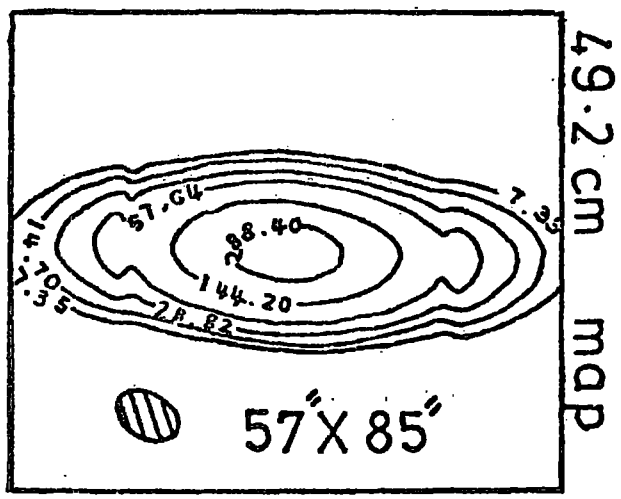

Fig. 5.17

The computed 610 Mhz map. This map is drawn to the same scale as fig. 3.10b . The contour intervals are also the same, but the units are such that 1 unit=0.46 K

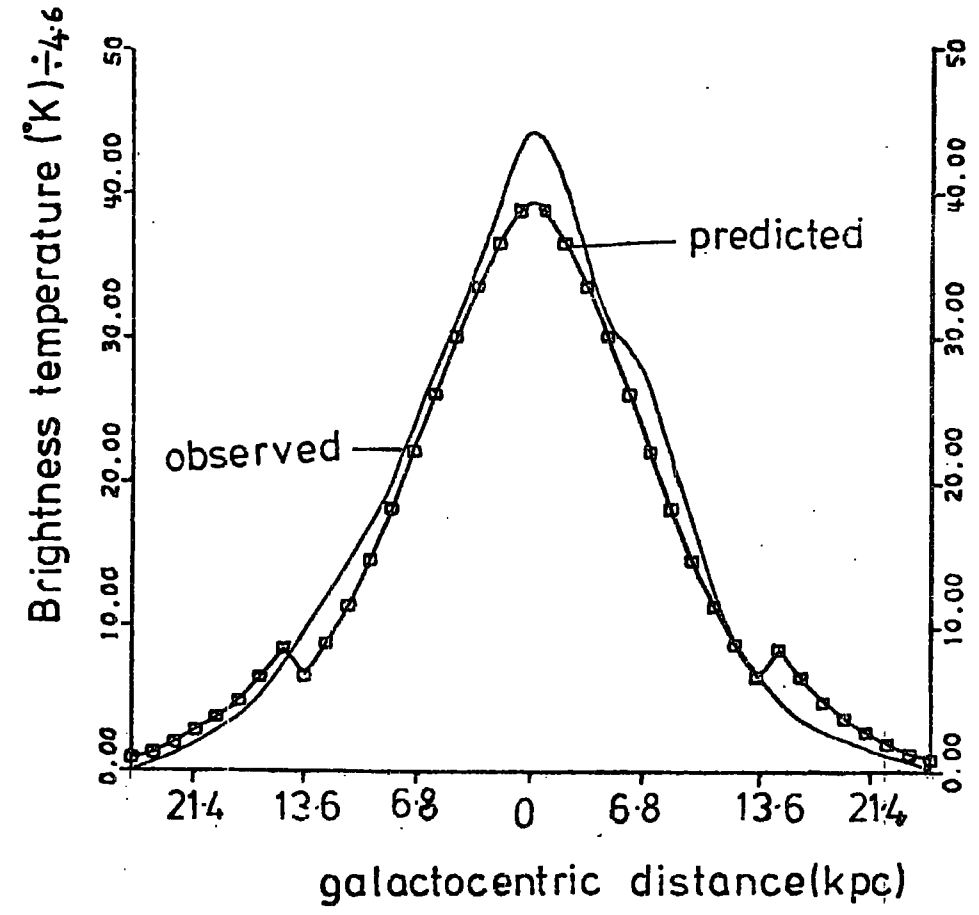

Fig. 5.18

The 610 Mhz profiles along the major axis of NGC 891.

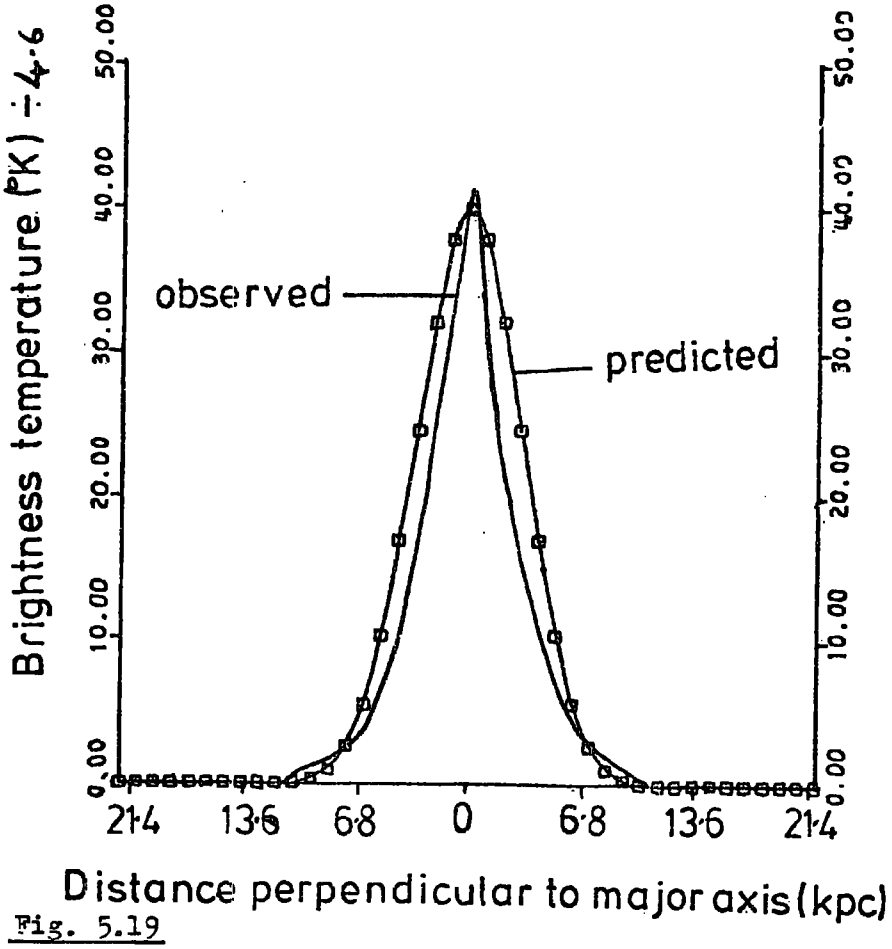

Fig. 5.19

The 610 Mhz profiles along the minor axis of NGC 891.

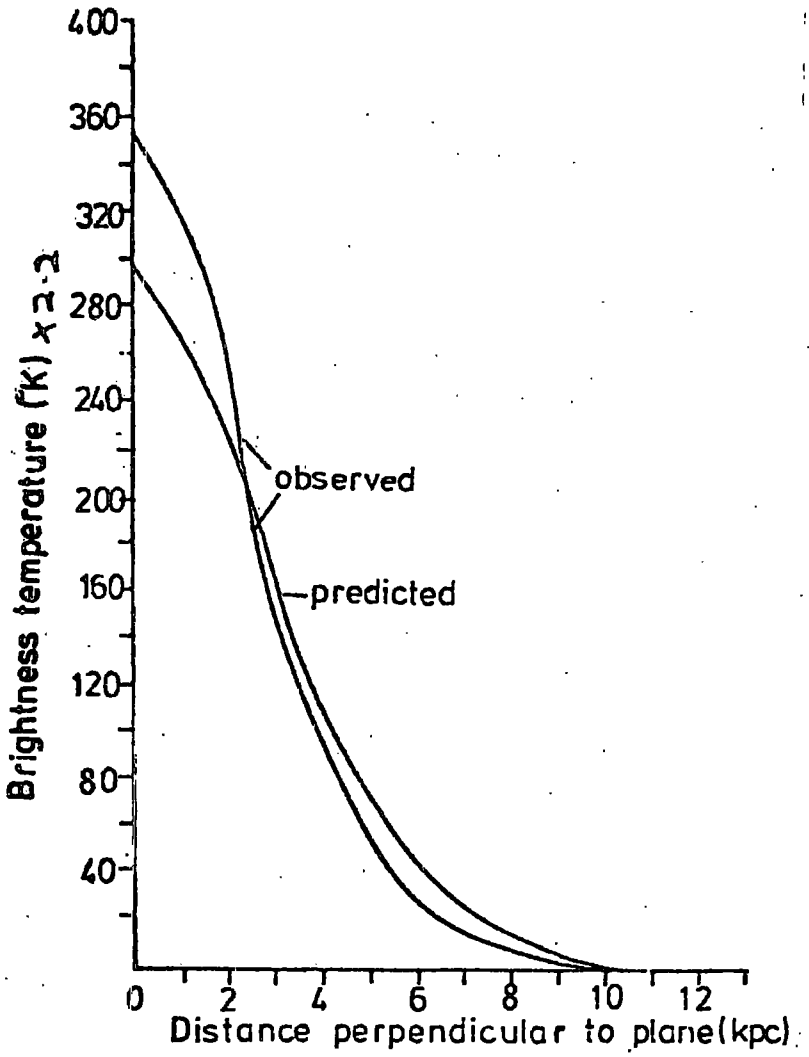

Fig. 5.20

610 Mhz observed and predicted profiles along the minor axis, after the emission has been averaged in strips 12 kpc in length parallel to and 2 kpc in width perpendicular to the major axis.

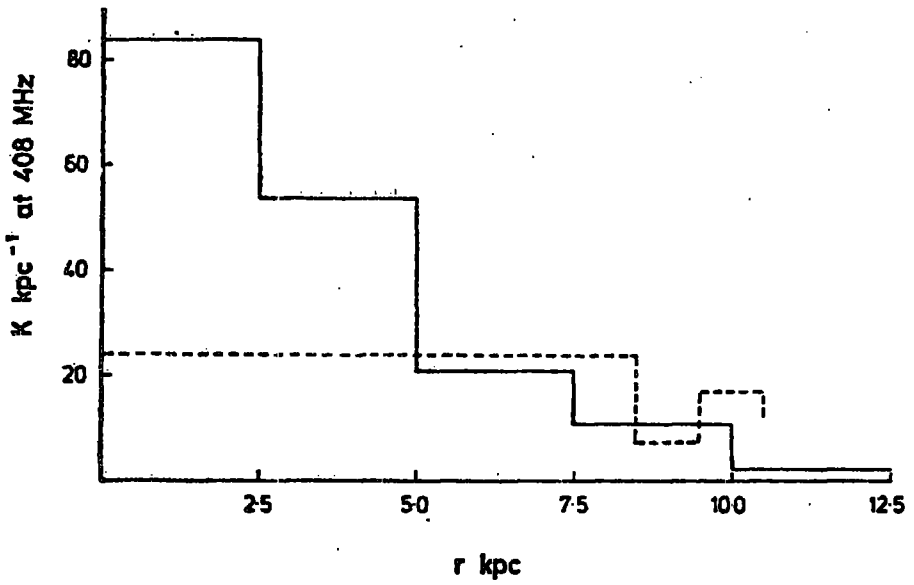

Fig. 5.21

The variation of emissivity along the semi-major axis of NGC 891 at 408 Mhz (Baldwin and Pooley 1973). The dashed line is that computed for the Galaxy if placed at 7 Mpc.

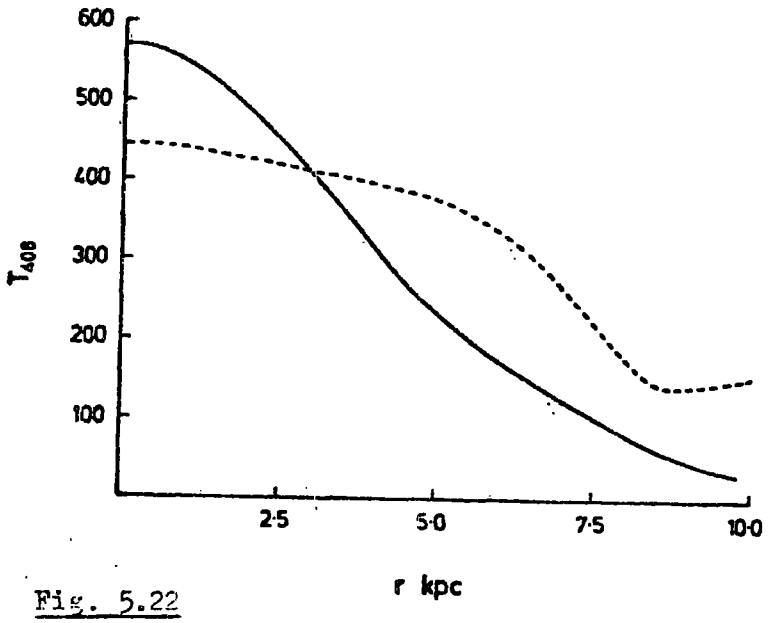

Fig. 5.22

The mean brightness temperature profile at 408 Mhz along the major axis of NGC 891 (Baldwin and Pooley 1973). The dashed line is the brightness that would be observed if the Galaxy was placed at 7 Mpc.

5.4 Comparison with NGC 4631.

The Westerbork radio map chosen for a comparison with the model predictions, is the 610 Mhz (Ekers and Sancisi 1977). The half-power beam width is 58" x 107" (1.5 x 2.7 kpc at the adopted distance of 5.2 Mpc). A 1412 Mhz map is also available (23" x 42"), but at this high resolution the nucleus is resolved into a triple structure and a 'spur' feature is prominent, so that the lower resolution map was considered more suitable for a comparison. This 610 Mhz map would also be expected to be more comparable to the 150 Mhz models of French (1977), and also thermal emission will be less important at this frequency.

To allow for the smaller linear size of NGC 4631, compared with the Galaxy, the linear scales of the predicted maps have been scaled down by 0.6. Radio maps of the galaxy produced by models 1 and 2 are shown in figs. 5.23 and 5.24 respectively. Figs. 5.25 and 5.26 show the emission profiles along the major and minor axes, with the observed profiles superimposed. The observed 610 Mhz map has been shown in fig. 3.10a. It can be seen that the model 2 computed map more closely resembles the observed one, than does the model 1. map.

Computed 610 Mhz maps of NGC 4631 for inclination angles of 85° and 80°, from model 1, are shown in figs. 5.27 and 5.28. On comparison with fig. 5.23, which was computed assuming NGC 4631 to be exactly edge-on, instead of $\sim 84°$, it is seen that the 85° one is almost identical with the 90° one. For this reason, and also to save computation time, all further maps were computed for an angle of inclination of 90°.

As in the case of NGC 891 there is an unresolved source of emission near the centre of the galaxy. Fig. 5.29 shows a 610 Mhz map produced with a point source of emission added. The major and minor axes profiles, with the observed ones superimposed, are shown in figs. 5.30 and 5.31, respectively. It can be seen that the observed peak in emission along

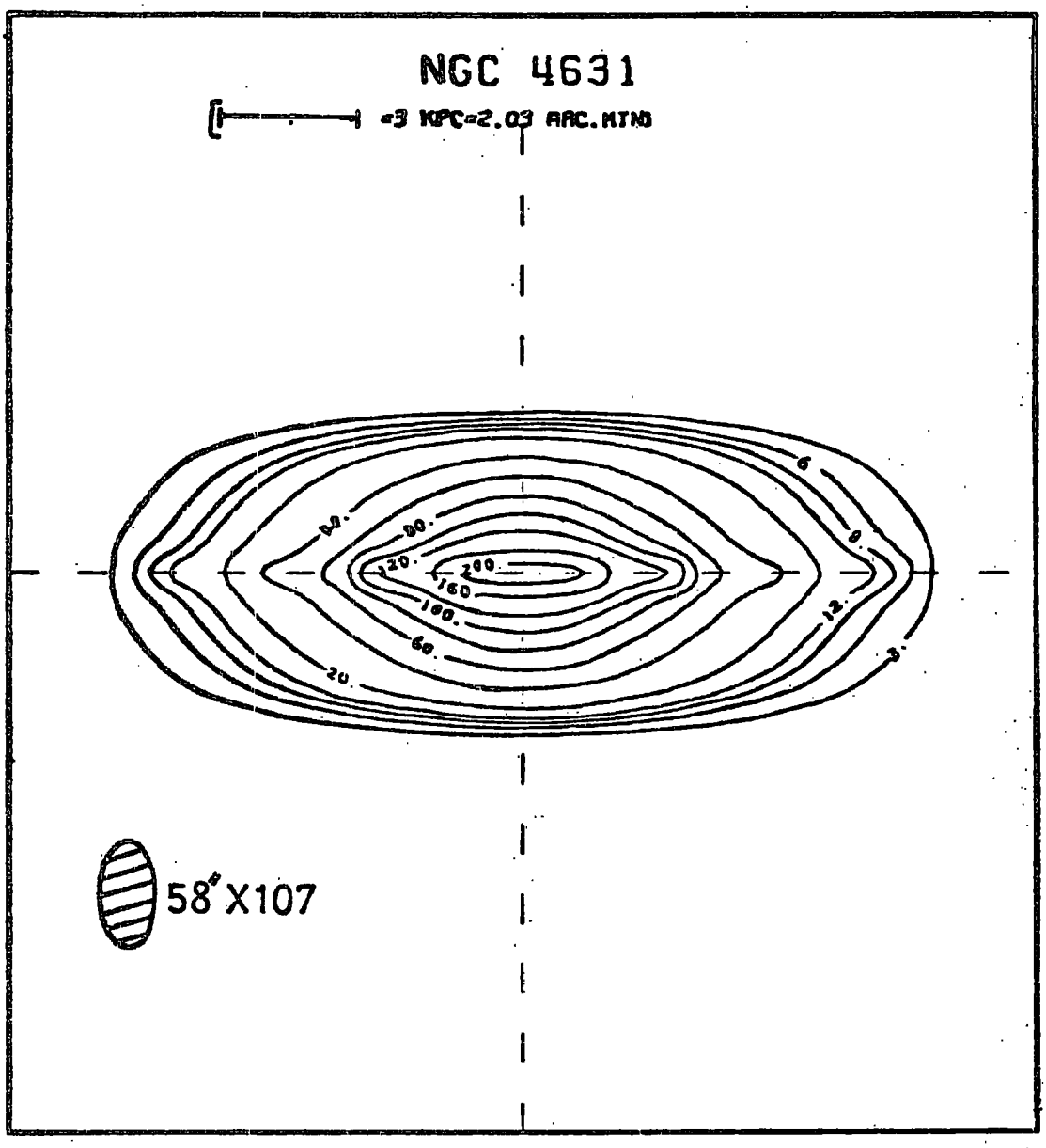

Fig. 5.23

Computed 610 Mhz map of NGC 4631 by model 1.

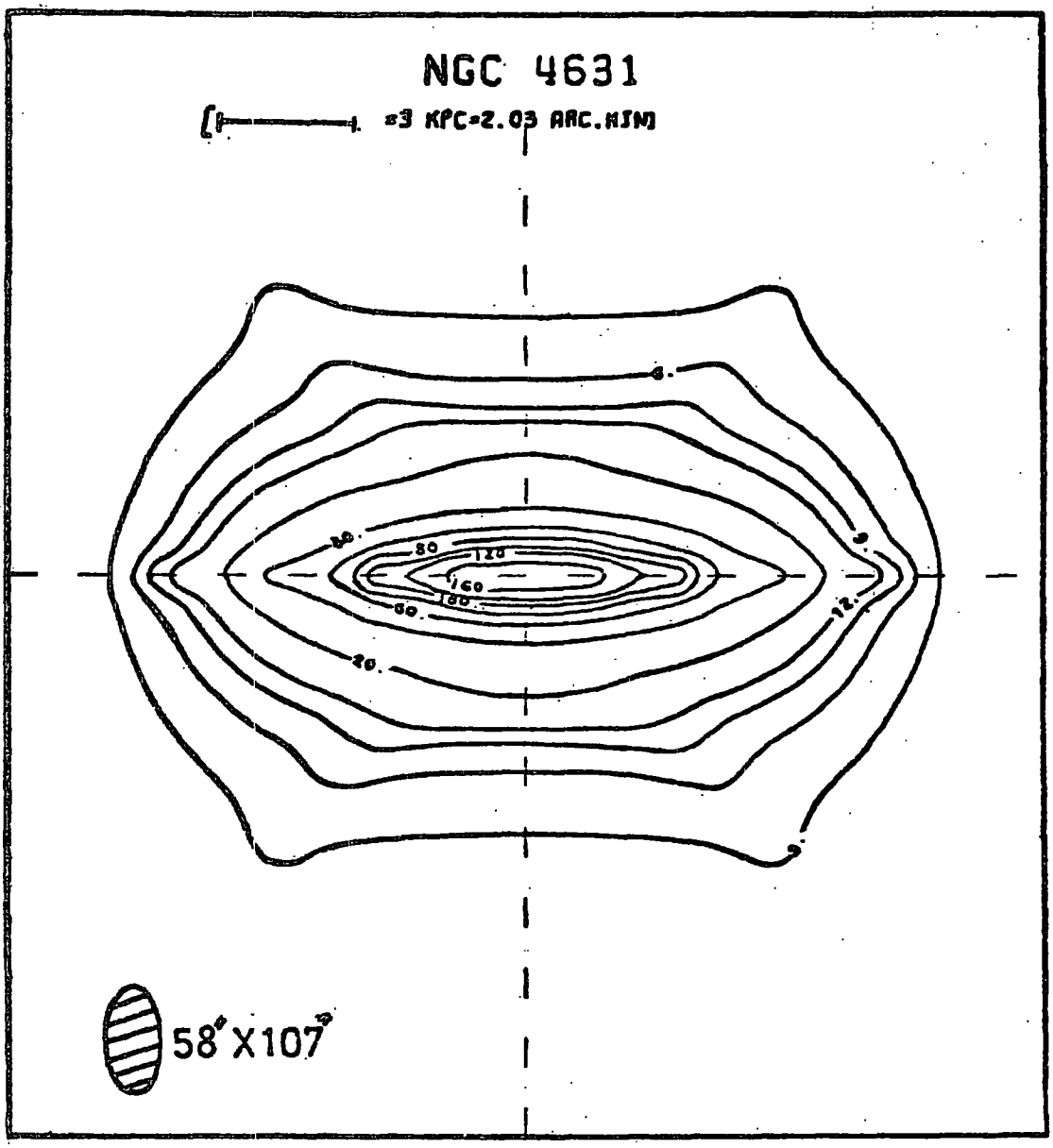

Fig. 5.24

Computed 610 Mhz map of NGC 4631 by model 2.

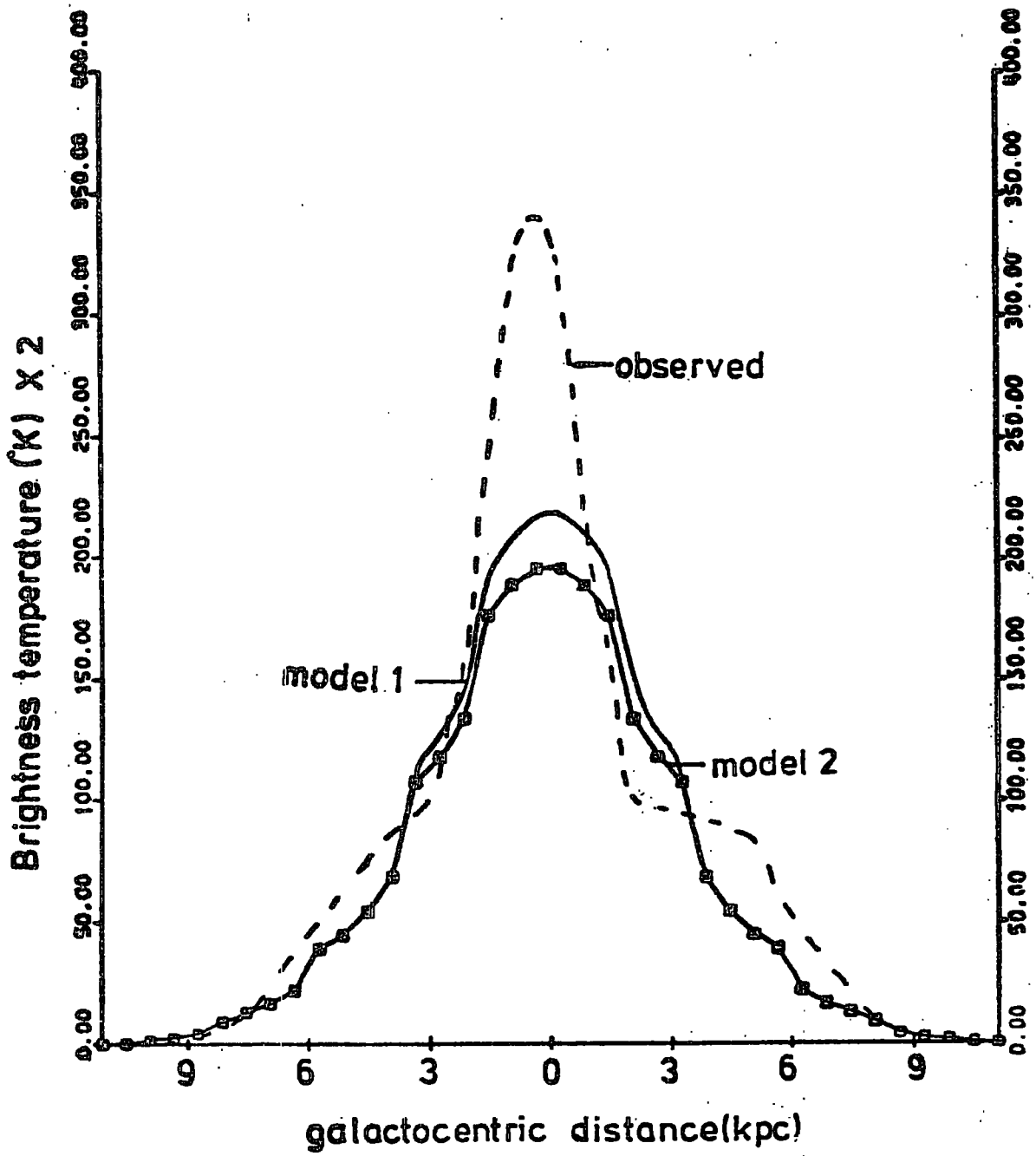

Fig. 5.25

The computed and observed 610 Mhz profiles along the major axis of NGC 4631.

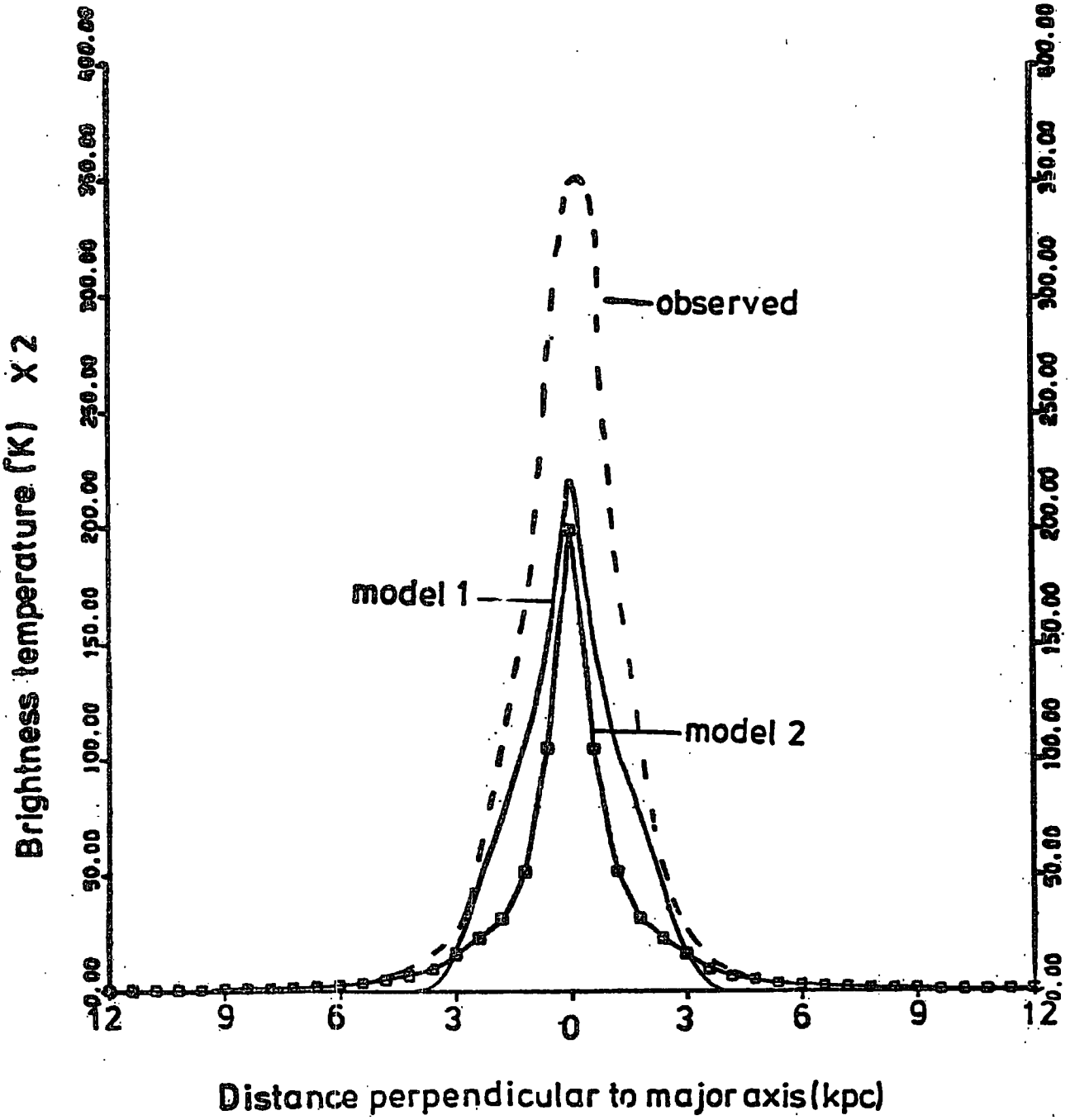

Fig. 5.26

The computed and observed 610 Mhz profiles along the minor axis of NGC 4631.

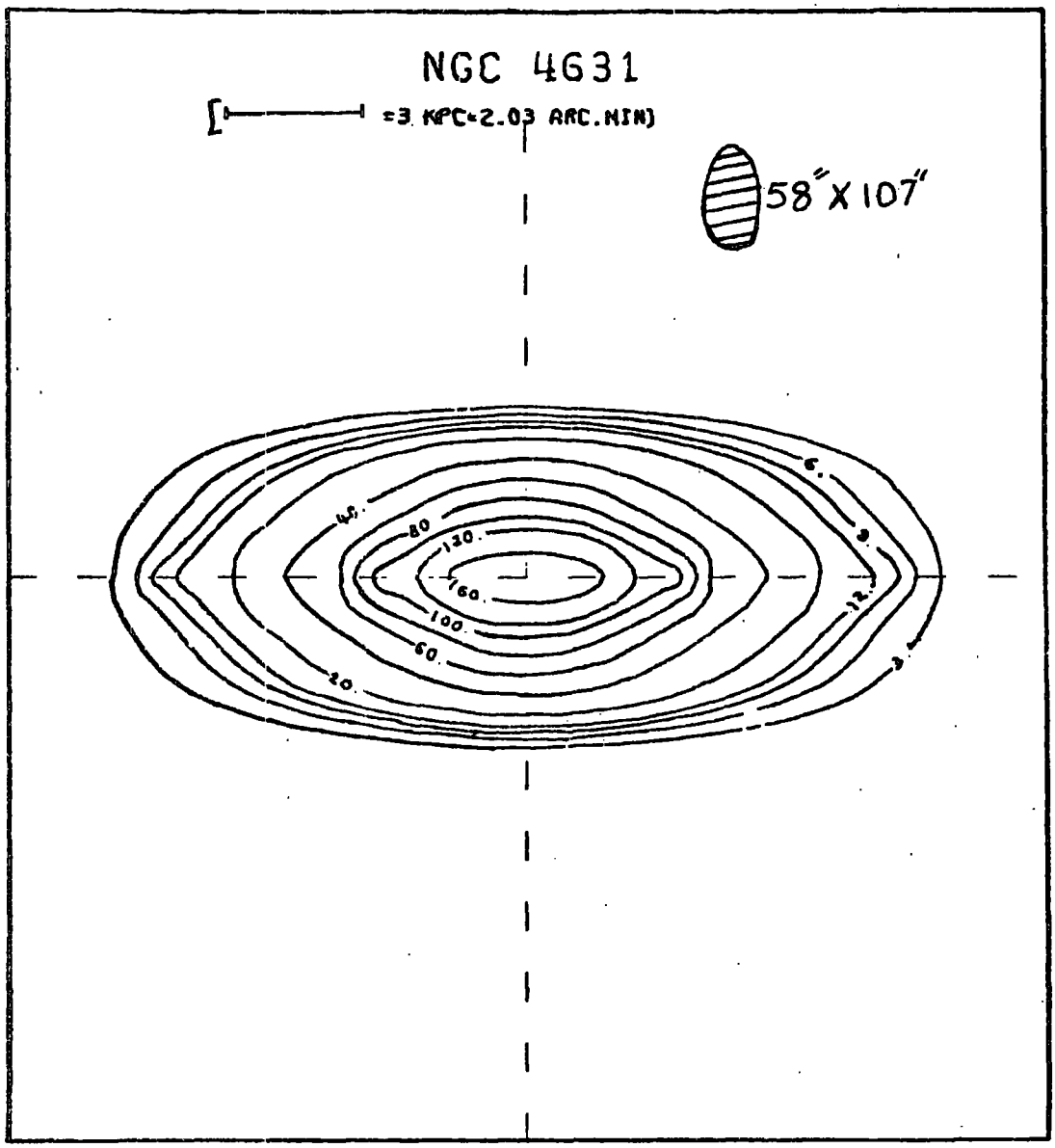

Fig. 5.27

The computed 610 Mhz map of NGC 4631, for model 1, for an angle of inclination of 85°.

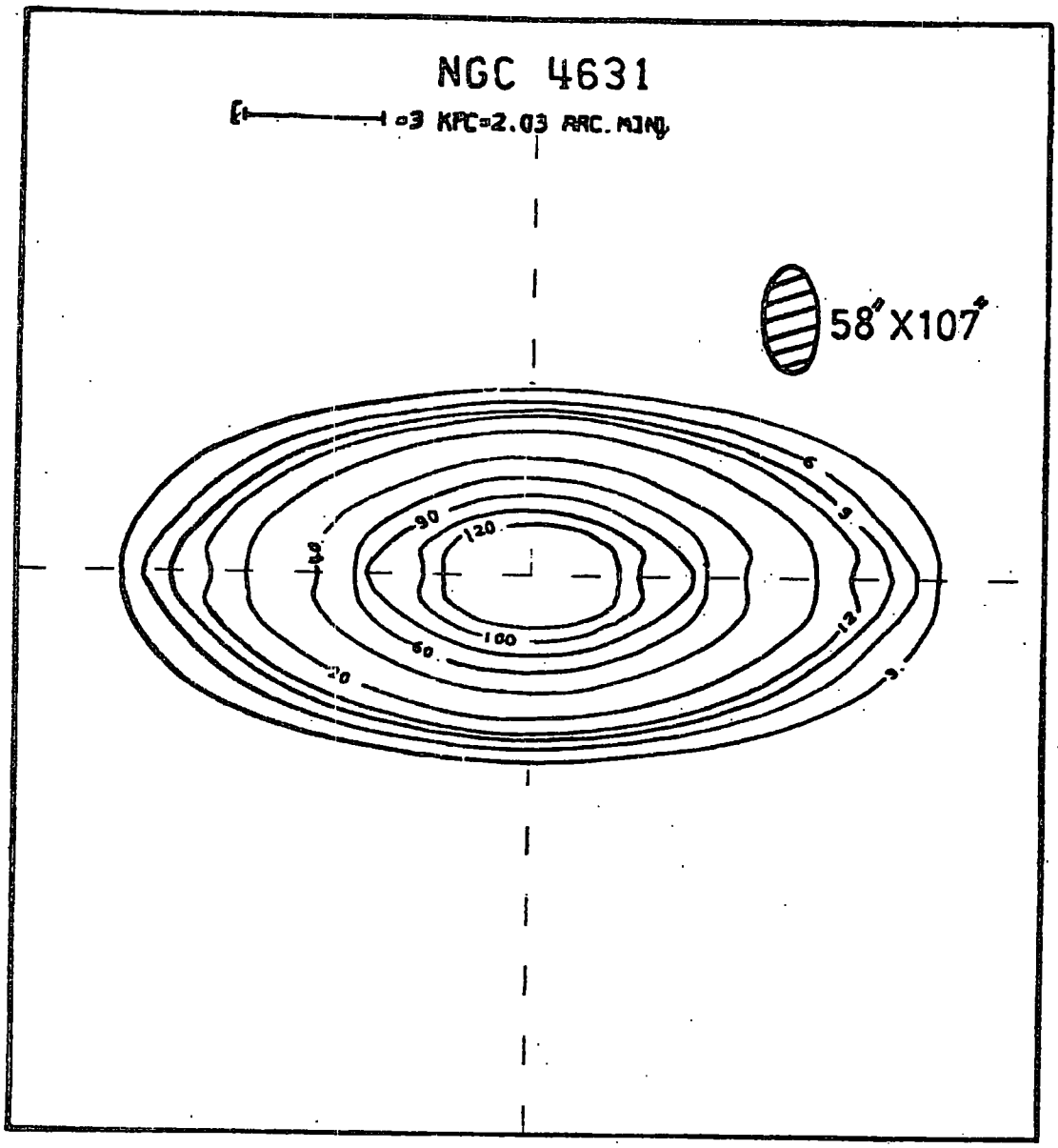

Fig. 5.28

The computed 610 Mhz map of NGC 4631, for model 1, for an angle of inclination of 80°.

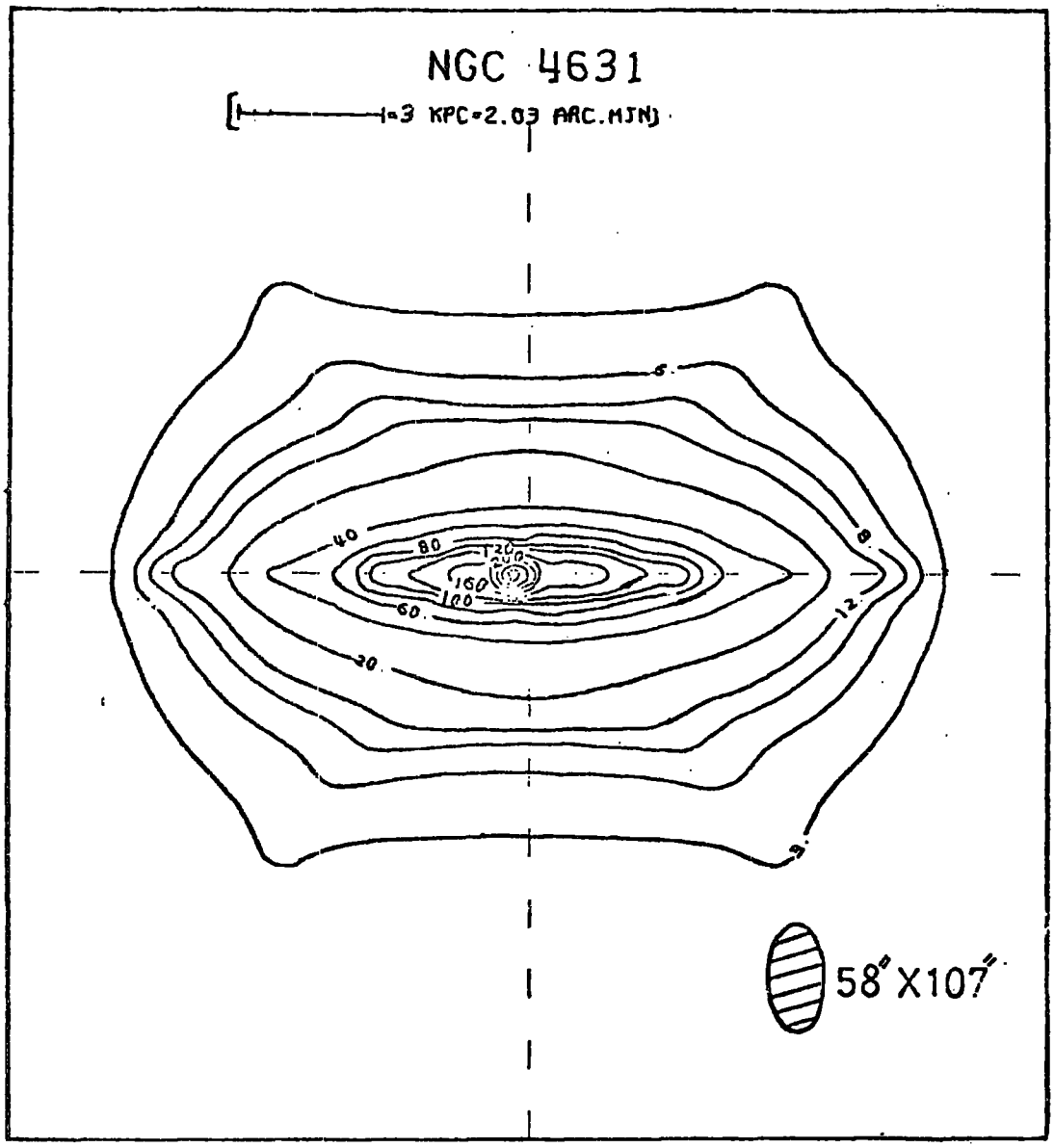

Fig. 5.29

The computed 610 Mhz map of NGC 4631 with a point source of emission added 0.8 kpc West of centre. The contour intervals are the same as those in fig. 3.11a, but the levels are such that 1 unit = 0.5°K.

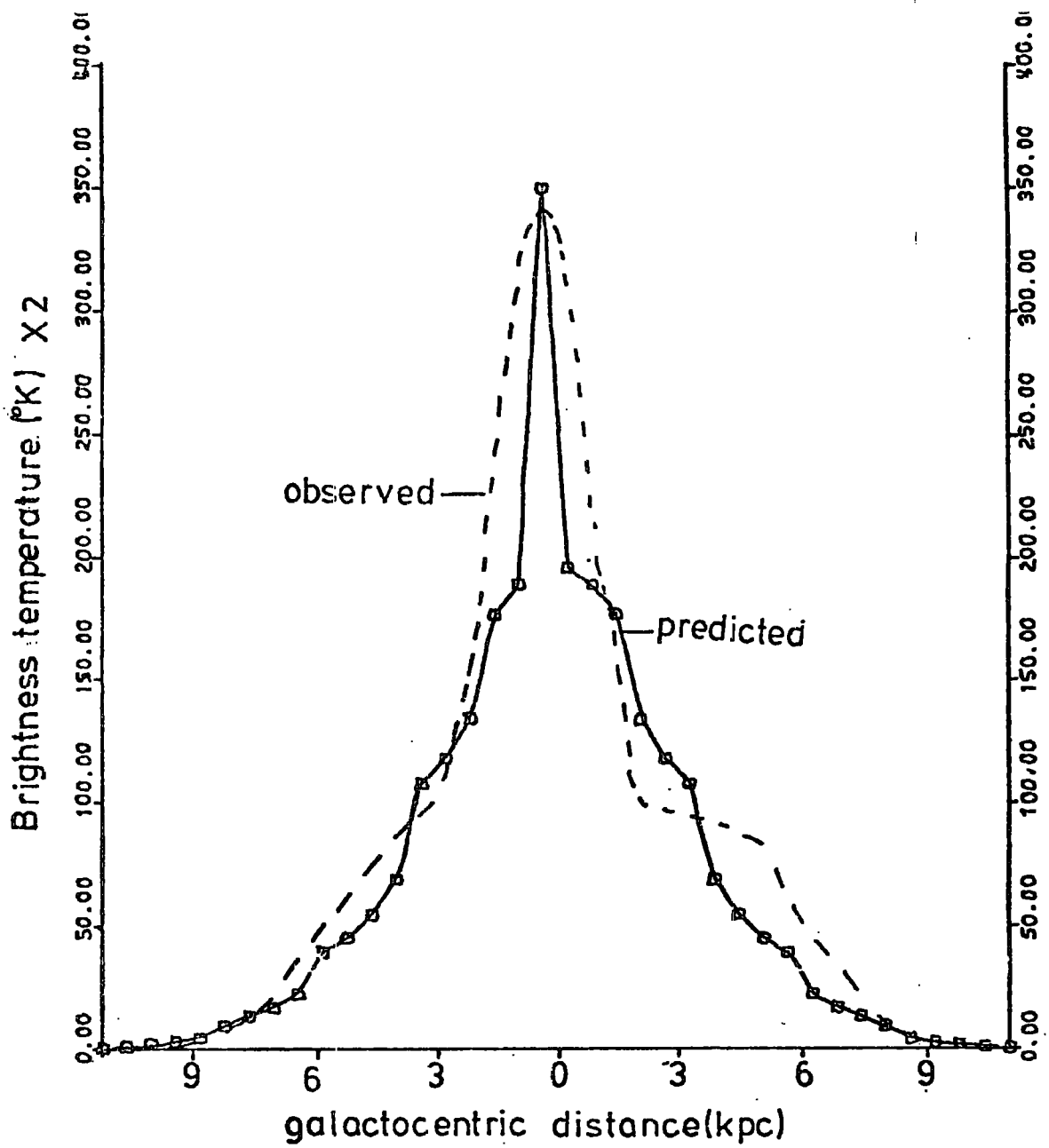

Fig. 5.30

The 610 Mhz observed and predicted profiles along the major axis of NGC 4631, after a point source of emission has been added.

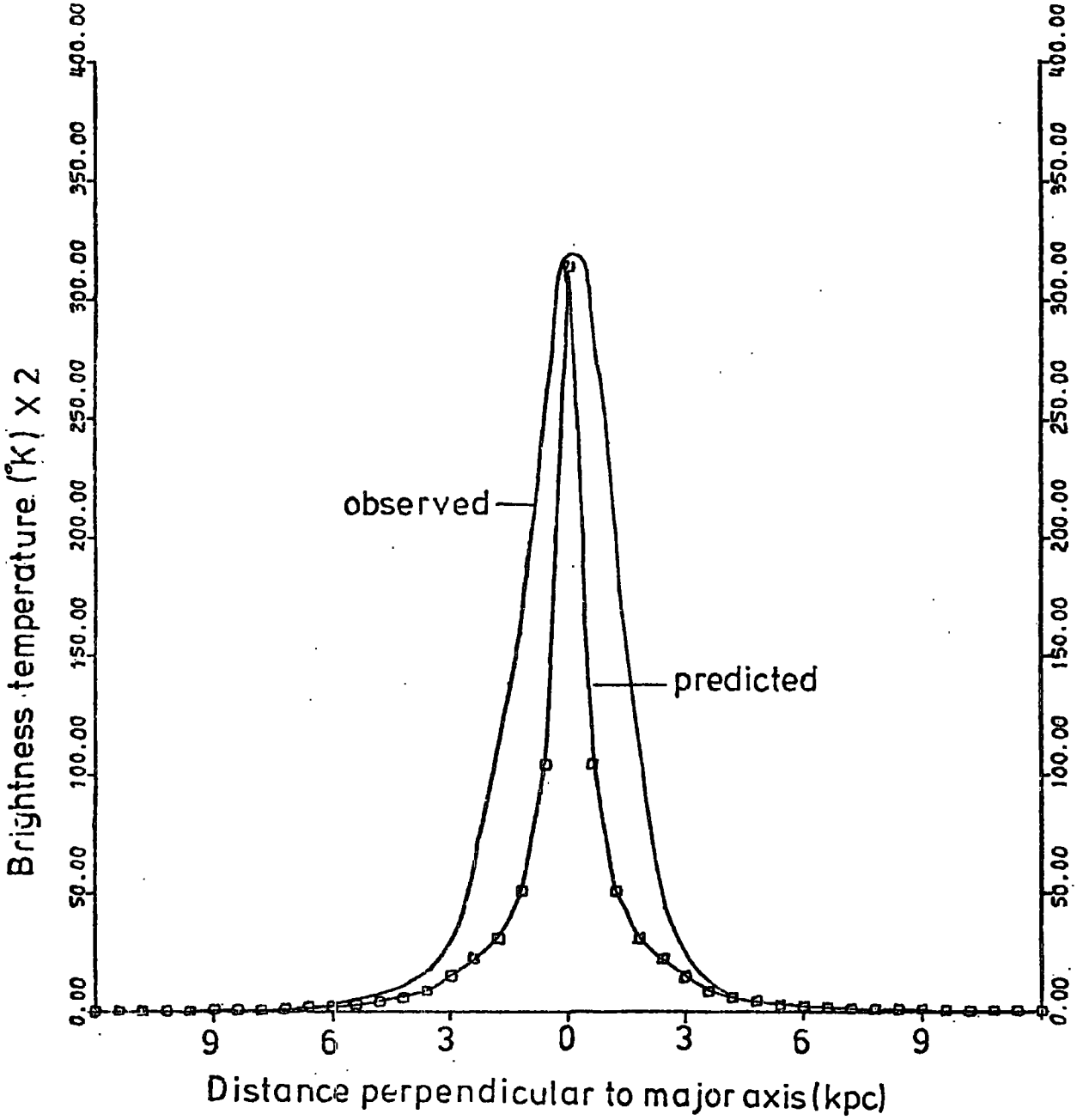

Fig. 5.31

The 610 Mhz observed and predicted profiles along the minor axis of NGC 4631, after a point source of emission has been added.

the major axis is broader than the predicted one. This is probably because the central source is in actual fact a triple source. On the whole the agreement is fairly reasonable. Table 5.3 lists the parameters used to produce this latter map.

Table 5.3

Map scale factor	0.6
Normalization constant	0.06
Emission (°K) added at centre	85
Radial displacement of source from centre (kpc)	0.8 (West)
Assumed distance (Mpc)	5.2
Position angle of telescope beam	95°
Half-power beam widths	58" x 107"

NGC 4631 is therefore three times brighter than the Galaxy at 610 Mhz (γ =2.6)

Radio maps are also available for NGC 4631, at 408 and 1407 Mhz (Pooley 1969), 4800 and 2695 Mhz (Wielebinski and von Kap-herr 1977) with the 100-m radio-telescope of the Max-Planck-Institut für Radioastronomie, and 1407 Mhz (Winter 1975) with the Cambridge extended Half-Mile telescope. The angular resolutions of these maps are 80" x 150" (2 x 3.75 kpc), 23" x 42" (0.58 x 1.01 kpc), 2.6' (3.9 kpc), 4.4' (6.6 kpc) and 2' x 3.75 (6 x 11.25 kpc) respectively.

As stated in chapter 1, the 408 and 1407 Mhz maps were made by the Cambridge One-Mile telescope, and no halo emission was detected. The resolutions of these maps are considered to be too poor for meaningful comparisons to be made.

5.5 Thermal Emission.

The thermal emission from HII regions is expected to be strongly concentrated to the galactic plane. The spectral index of thermal emission, 2.1, is considerably flatter than the brightness spectral index of 2.8, so that at high frequencies the thermal emission will eventually dominate the radio emission.

For the Galaxy Hirabayashi (1974), has estimated that at 150 Mhz, around seven per cent of the observed emission is thermal, whereas at 408 Mhz the value is nineteen per cent. Large et al. (1961), investigated the thermal percentage variation of thermal emission with longitude, and found that the thermal emission peaks at approximately the galactic centre. Observations of M33 by Israel and van der Kruit (1974), at high resolution, show many individual HII regions. They extrapolated the emission from these sources to the less luminous HII regions, and estimated that all the radio emission at 1400 Mhz could be thermal.

In the case of edge-on galaxies the effect of the thermal emission on the contour lines, is to increase the axial ratios. The thermal emission could also be partly responsible for the change of spectral index across the discs of NGC 891 and NGC 4631. Van der Kruit (1977), showed that the spectral index change across the face of M51, can be explained by the variations in the amount of thermal emission with position. Allen, Baldwin and Sancisi (1977), estimated that less than one-third of the disc emission, at 5 Ghz, is thermal, or less than about 10 per cent of the total flux density of NGC 891. Strong (1977), points out that the spectral indices α^{1412}_{4995}, α^{610}_{4995} and α^{610}_{1412}, in NGC 891, at the 610 Mhz beam resolution at Z = 0, are all equal within the experimental error ($\Delta\alpha \sim 0.02$), contrary to a decreasing of α that would occur if the thermal contribution was significant.

It is therefore concluded that the omission of thermal radiation,

below frequencies of about 2 Ghz, is not serious.

5.6 Compression Strengths.

In the models of NGC 4631 and NGC 891, it has been assumed that they have the same compression strength as that of the Galaxy. Since the enhanced emission from the region near to the galactic plane, is partly due to the compression of the magnetic field by the spiral shocks of Density Wave Theory, a higher compression strength could explain the much higher disc emissions, of the two galaxies. The increase in emission roughly follows the form $\frac{\varepsilon}{\varepsilon_0} = \left(\frac{\rho}{\rho_0}\right)^{2.7}$, where ρ_0 and ρ are the gas densities before and after the shock respectively. Therefore, the emission is strongly dependent on the compression strengths in the arms. Mouschovias et al. (1974), have shown that the enhancement in radio emission will be less than that predicted from above, since the magnetic field will buckle in the perpendicular direction, owing to the onset of the Parker instability. The electrons will also be redistributed by their own pressure, when a Parker instability is formed. It is possible that this mechanism could explain some of the high Z-emission in NGC 891 and NGC 4631. The dust visible in optical photographs of NGC 891 at distances of about one kiloparsec from the plane, could have been ejected by this mechanism, and would therefore contain magnetic fields.

Such radio enhancement, due to spiral shocks, is seen in M51 (Mathewson et al. 1972), M81 (van der Kruit 1973a), M101 (Israel et al. 1975), NGC 4258 (van der Kruit et al. 1972) and IC 342 (Baker et al. 1977). Instances where the radio enhancement seems to be absent, are Maffei II (Allen and Raimond 1972) and NGC 2403 (van der Kruit 1973a).

For both NGC 891 and NGC 4631, no estimate of the compression strength is possible from the radio-continuum observations. In the case of about a dozen other spiral galaxies, crude estimates of the amount of compression have been obtained (van der Kruit 1973b), by making use of the

above formula.

The shock strength depends on the velocity with which the gas approaches the shock. These velocities are larger, on the average, in galaxies in which the rotation curve reaches its maximum at a radius (R_{max}) much smaller than that of the outermost HII region (R_{opt}), when the pattern speed of the density wave equals the rotation speed of the outermost HII region. The compression strength also correlates with the luminosity classification of van den Bergh, which is based on the narrowness of the optical arms. From table 1 of van der Kruit (1973b), NGC 4631 is assigned a compression strength somewhere in the region 0 - 1 (< 0.5 weaker compression, 0.5 - 1.0 intermediate compression, > 1.0 strong compression). Van der Kruit points out that if the central complex of emission is a triple radio source, such as in NGC 4736, then NGC 4631 would be a low compression-strength galaxy. The triple structure observed in the central region of NGC 4631, at high resolution, could be due to the emission from the spiral arms when seen tangentially (Pooley 1969, van der Kruit 1973a), or the result of explosions in the nucleus.

In the case of our Galaxy, the observed value of R_{max} / R_{opt} is 0.5 - 0.6, and from fig. 6 of van der Kruit (1973b), it is seen to be a weak compression system (Type A), but could be of intermediate Type B.

In the case of NGC 891, the only clue to its compression-strength comes from the observed radial velocities of HI. As discussed in Chapter 3, these are similar to what is observed in the Galaxy, making it unlikely that its compression strength is much greater than that in the Galaxy.

It is therefore not possible to explain the much greater emission from NGC 4631 and NGC 891, simply by greater shock-strengths.

5.7 Magnetic Fields.

Oort (1972), showed that the large range in radio brightness from one galaxy to another, could be explained as being due to large variations in the magnetic field strengths. Allen, Baldwin and Sancisi (1977), calculated the equipartition magnetic field in the Galaxy, NGC 891 and NGC 4631, assuming $\alpha = -0.65$ and that there is 100 times as much energy in the total cosmic ray flux as in the electron component, the values being 0.5, 0.7 and 1.1 x 10^{-5} gauss, respectively. It is seen that only a small range of magnetic field intensities is needed to produce the diverse radio fluxes, this being due to the intensity of radio emission being dependent on approximately the square of the magnetic field intensity.

The continuum-radio emission about NGC 4631 resembles that predicted by White (1977), from his galactic dynamo model which is surrounded by ionized intergalactic hydrogen (density 10^{-5} - 10^{-6} particles cm^{-3}). In this model the magnetic field arises from the differential rotation of the galaxy, which causes shearing of the gas and current loops, which generate the field. The magnetic field intensity is also determined by the form of the rotation curve, greater differential rotation producing a more intense magnetic field.

Brecher and Burbidge (1970) found no compelling astrophysical evidence for the existence of intergalactic matter, but recent data from radio and X-ray astronomy suggest that it does exist (Field 1972, 1974). Earlier optical studies indicated the existence of absorbing matter within the Coma cluster of Galaxies (Zwicky 1962, Karachentsev and Lipovetskii 1968), but the reality of the extinction effect has been questioned. Probably the best evidence for intergalactic matter has come from the observed X-ray background between 1 - 100 Kev. The observations are consistent with hot intergalactic gas of $n \sim 10^{-5}$ cm^{-3} and $T \sim 10^{8}$ K (Sciama 1973, Field and Henry 1964).

Strong (1977), has done calculations of the diffusive and convective transport of electrons away from the disc of NGC 891, to account for the spatial distribution of intensity and spectral index in the halo. He found that the magnetic field must fall off slowly with height above the plane, with most of the radio intensity decrease resulting from electron propagation and energy losses.

It therefore seems likely that the different radio luminosities of the three galaxies, is simply due to different magnetic field intensities.

5.8 Conclusion.

The models of French (1977), of the Galactic radio-continuum emission, can reasonably well explain the distributions of emission in NGC 891 and NGC 4631. Model 1 which can account for that of NGC 891, and model 2 for that of NGC 4631, produce fits to the observed Galactic radio emission which are nearly as good as each other. Therefore modelling of edge-on galaxies is useful to see if models of the Galaxy are 'reasonable'. Because the radio-telescope resolutions, used so far to map these galaxies, are not good enough to resolve the spiral structure, other simpler models could also reproduce the observations.

It is important to note that it is difficult to clearly distinguish between a 'halo' and a thick disc of emission. Van der Kruit and Allen (1976), distinguish 'halos' from 'thick discs', if the axial ratio of the faintest reliable radio contours exceeds 0.5.

Chapter 5 - References.

Allen, R. J., Baldwin, J. E. and Sancisi, R. 1977, Astron. and Astrophys. (in the press).

Allen, R. J. and Raimond, E. 1972, Astron. and Astrophys. 19, 317.

Baars, J. W. M. and Hooghoudt, B. G. 1974, Astron. and Astrophys. 31, 323.

Baker, J. R., Haslam, C. G. T., Jones, B. B. and Wielebinski, R. 1977. Astron. and Astrophys. 59, 261.

Baldwin, J. E. and Pooley, G. G. 1973, Mon. Not. R. Astr. Soc. 161, 127.

Brecher, K. and Burbidge, G. R. 1970. Comments Astrophys. Space Phys. 2, 75.

Ekers, R. D. and Sancisi, R. 1977, Astron. and Astrophys. 54, 973.

French, D. K. 1977, Ph.d thesis University of Durham.

Field, G. B. 1972, Annual Rev. Astron. Astrophys. 10, 227.

Field, G. B. 1974, in M. S. Longair, Ed., Confrontation of Cosmological Theories with Observational Data, I. A. U. Symp. 63, pp 13 D. Reidel, Boston, Mass.

Field, G. B. and Henry, R. C. 1964, Astrophys. J. 140, 1002.

Hirabayashi, H. 1974, Publ. Astron. Soc. Japan. 26, 263.

Högbom, J. A. and Brouw, W. N. 1974, Astron. and Astrophys. 33, 289.

Israel, F. P., Goss, W. M. and Allen, R. J. 1975, Astron. and Astrophys. 40, 421.

Karachentsev, I. D. and Lipovetskii, V. A. 1968, Astron. Zh. 45, 1148 (English translation in Sov. Astron. A - J. 12, 909, 1969).

Kruit, P. C. van der 1973a, Astron. and Astrophys. 29, 231.

Kruit, P. C. van der 1973b, Astron. and Astrophys. 29, 263.

Kruit, P. C. van der 1977, Astron. and Astrophys. 59, 359.

Kruit, P. C. van der, Oort, J. H. and Mathewson, D. S. 1972, Astron. and Astrophys. 21, 169.

Kruit, P. C. van der, and Allen, R. J. 1976, in Annual Review of Astronomy and Astrophysics, Vol. 14 p. 439.

Large, M. I., Mathewson, D. S. and Haslam, C. G. T. 1961, Mon. Not. R. Astr. Soc. 123, 123.

Mathewson, D. S., Kruit, P. C. van der, and Brouw, W. N. 1972, Astron. and Astrophys. 17, 468.

Mouschovias, T. C., Shu, F. H. and Woodward, P. R. 1974, Astron. and Astrophys. 33, 73.

Oort, J. H. 1972, Karl-Schwarzschild Vorlesung, Astronomische Gesellschaft, Wien, September 1972.

Pooley, G. G. 1969, Mon. Not. R. Astr. Soc. 144, 143.

Sciama, D. W. 1973. Modern Cosmology. p. 142, Cambridge University Press.

Strong, A. W. 1977, submitted Astron. and Astrophys.

Webster, A. 1975, Mon. Not. R. Astr. Soc. 171, 243.

Wielebinski, R. and Kap-herr, A. von 1977, Astron. and Astrophys. 39, 17.

White, M. P. 1977, Ph.d thesis University of Durham.

Winter, A. J. B. 1975, Mon. Not. R. Astr. Soc. 172, 1.

Zwicky, F. 1962, in G. McVittie, ed. Problems in Extragalactic Research. pp 347, Macmillan, New York

Acknowledgements.

I am grateful to the Science Research Council for the provision of a Research Studentship, during the period of this work.

Professor A. W. Wolfendale, F. R. S., is thanked for enabling me to do the work presented in this thesis, and especially Dr. J. L. Osborne, my supervisor, for endless help and guidance.

Dr. D. K. French, in particular, and Drs. A. W. Strong and M. P. White and Mr. S. Kearsey, are thanked for useful discussions and help on various aspects of the work.

The staff of the Durham University Computer Unit are thanked for help in solving certain problems.

Mrs. K. Jones is thanked for remaining calm and collected during the typing of this thesis, and for making such a good job of it. A person, who would like to remain anonymous, is thanked for carefully producing most of the figures. Mr. M. Lee is thanked for skilfully producing figs. 3.1 and 3.2. My sisters Jacqueline and Suzanne Brindle are thanked for help in producing a few of the figures.

Finally I would like to thank the relevant members of the Mathematics and Physics Departments of the University of Newcastle upon Tyne, in particular Mr. E. Wilkes, Dr. G. McCartan and Dr. C. Gilbert.

3 SEP
REDYOR
LIBRARY